

Frequency Synchronization in HSPA+/LTE Communications: A General Model and Towards Uniform Implementation

Von der Fakultät für Elektrotechnik und Informatik
der Gottfried Wilhelm Leibniz Universität Hannover

zur Erlangung des akademischen Grades

Doktor-Ingenieur

genehmigte

Dissertation

von

M.Eng. Qipeng Cai

geb. am 20. April 1976 in China

2013

Referent: Prof. Dr.-Ing. Thomas Kaiser
Koreferent: Prof. Dr.-Ing. Jürgen Peissig
Vorsitzender: Prof. Dr.-Ing. Bodo Rosenhahn
Tag der Promotion: 9. April 2013

Acknowledgment

I am deeply grateful to my advisor Prof. Dr.-Ing. Thomas Kaiser for his encouragement, guidance throughout my Ph.D. study. He provided me great freedom to choose my interested research topic while directed and critiqued me just in time. Without his inspiration, support and care the accomplishment of this dissertation would have been impossible.

I would like to thank Herrn Dr.-Ing. Andreas Wilzeck for his thoughtful discussion, comments and cooperation. His remarkable insight into the field helped me substantially. My special thanks to my roommate Herrn Dipl.-Ing. Li Li for his vital support for my daily life during writing the dissertation.

For their help, hospitality and discussions, I am very thankful to all my colleagues at the Institute for Communications Technology: Frau Barbara Adler, Frau Eva-Maria Schroeder, Herrn Dipl.-Ing. Rolf Becker, Herrn M.Sc. Zhao Zhao, Herrn M.Sc. Hanwen Cao, Herrn Dr.-Ing. Bamrung Tau Sieskul, Frau M.Sc. Anggia Anggraini, Dr.-Ing. Sami Akin, Frau Dipl.-Wirtsch.-Ing. Kim Bartke-Minack, Herrn Dipl.-Ing. Martin Fuhrwerk, Herrn Dipl.-Ing. Waldemar Gerok, Herrn Dipl.-Wirtsch.-Ing. Henrik Schumacher, Dipl.-Ing. Christoph Thein, Dipl.-Ing. Andrej Tissen and all the students who have assisted me during this work.

I would like to thank the co-founders also my colleagues at RFmondial GmbH: Herrn Dr.-Ing. Albert Waal, Herrn Dr.-Ing. Jens Schroeder, Herrn Dipl.-Ing. Stefan Galler and Herrn Dr.-Ing. Yuri Vatis. Without their vital support on the finance, I could not persevere with this work.

Last, but certainly not least, I would like to acknowledge my family. Thanks to my parents and all my relatives for their love and encouragement.

Kurzfassung

Im Verlauf des letzten Jahrzehnts wurde durch unzählige Internetanwendungen der Bedarf an mobilen Netzverbindungen hoher Kapazität geweckt. Das Ziel breitbandiger Internetzugänge zu jeder Zeit an jedem Ort wurde dabei mit Nachdruck verfolgt. In der letzten Evolutionsstufe der dritten Generation sowie der kommenden vierten Generation mobiler Kommunikationssysteme kommen daher hochentwickelte Verfahren der Übertragungsschicht wie 64 QAM, OFDM oder MIMO zum Einsatz, um den Datendurchsatz zu erhöhen. Der Einsatz komplexer Verfahren macht diese neuen Systeme jedoch anfälliger für Unzulänglichkeiten der eingesetzten Hardware, wobei der Frequenzversatz von großer Bedeutung ist.

Diese Dissertation widmet sich daher dem Thema der Frequenzsynchronisation in 3GPP HSPA+, sowie LTE Systemen. Zuerst wird ein Empfangssignalmodell mit Frequenzversatz für das HSPA+ System entworfen, um den Einfluss des Frequenzversatzes genauer zu untersuchen. Im Anschluss wird eine analytische Methode zur Auswertung der Fehlerhäufigkeit von HSPA+ Systemen vorgestellt, unter Berücksichtigung sowohl von ICI als auch Fehlern der Kanalschätzung.

In einem zweiten Schritt wird ein Empfangssignalmodell für LTE Systeme mit Frequenzversatzfehler vorgestellt. Durch den Vergleich beider Systeme beim Vorhandensein eines Frequenzversatzes zeigen wir die Ähnlichkeit beider Empfangssignalmodelle. Basierend hierauf wird ein allgemeines Empfangssignalmodell entworfen, und die zuvor beschriebene Fehlerhäufigkeit Methode für beide Systeme generalisiert.

Zum Vergleich der Leistungsfähigkeit der Frequenzversatzschätzung für beide Systeme werden die unteren Grenzen eines erwartungstreuen Schätzers diskutiert. Es zeigt sich, dass für den Fall, dass der Frequenzversatz nicht vernachlässigbar ist, die bedingte Wahrscheinlichkeitsdichtefunktion der Beobachtungen die Regularitätsbedingung verletzt, welche notwendig ist für die Gültigkeit der oft genutzten Cramér-Rao Bound. Es wird daher die Annäherung der Barankin Bound hergeleitet, und zum Vergleich der Leistungsfähigkeit der Frequenzversatzschätzung mit variabler Anzahl an Beobachtungen verwendet.

Das letzte Kapitel dieser Arbeit beschäftigt sich mit der Implementierung der Frequenzsynchronisation in HSPA+ und LTE Systemen. Hierzu werden verschiedene Algorithmen zur Frequenzsynchronisation implementiert und verglichen. Basierend auf dem zuvor entworfenen allgemeinen Empfangssignalmodell und der Rahmenstruktur beider Systeme wird eine generalisierte Struktur zur Frequenzsynchronisation von HSPA+ und LTE Systemen entwickelt, welche die Implementierung der Frequenzsynchronisation in dual-mode Geräten vereinfachen kann.

Schlagwörter – HSPA+, LTE, Frequency Synchronization

Abstract

Over the past decade, numerous innovative Internet-based applications promote the blooming of the demands of wireless Internet access systems with high capability. There have been persistent efforts to realize *anywhere-anytime* broadband wireless Internet access. In the latest evolution of recent third generation mobile communication systems and the upcoming fourth generation mobile communication systems, many advanced techniques are introduced in the physical layer design, such as 64-QAM, OFDM, MIMO, etc., in order to realize higher system throughput. However, the introduction of those new techniques *may* lead systems more sensitive to hardware imperfections, in which *frequency offset* is an important member.

This dissertation is devoted to discuss the issues on frequency synchronization in *Evolved High-Speed Packet Access (HSPA+)* system and 3GPP *Long Term Evolution (LTE)* system. First, the received signal model for the HSPA+ system with frequency offset is derived to reveal the impairment of frequency offset. Sequently, an analytical method is proposed for evaluating the error rate performance of HSPA+ system by taking into account both the *Inter-Channel Interference (ICI)* and channel estimation error.

Secondly, we model the received signals of an LTE system with frequency offset. By comparison we show the similarity of the received signal models for both systems. Therefore, a general signal model is proposed and the previously proposed error rate evaluation method is further generalized for both systems.

For establishing the performance benchmark for frequency offset estimation for both systems, we discuss lower bounds for unbiased estimators based on the proposed general signal model. It is found that the conditional *Probability Density Function* of the observations normally violates the regularity conditions when the interference caused by the frequency offset is not negligible, which are necessary for the existence of the widely used *Cramér-Rao Bound*. To overcome this difficulty, we resort to the *Barankin Bound*. The approximation of the Barankin Bound is derived and the performance benchmark of frequency estimation is evaluated with different number of observations.

Finally, this dissertation discusses how to implement frequency synchronizer in HSPA+ system and LTE system. The strategy is addressed and different frequency estimation algorithms are evaluated and compared. Based on the general model for the received signals and the frame structures of both systems, a uniform structure is devised to realize frequency synchronizers for HSAP+ system and LTE system, which *may* simplify the implementation of frequency synchronizer in a *Dual-Mode User Equipment*.

Keywords – HSPA+, LTE, Frequency Synchronization

Contents

Acknowledgment	ii
Kurzfassung	iii
Abstract	iv
List of Figures	viii
List of Tables	x
List of Acronyms	xi
List of Symbols	xiv
1 Introduction	1
1.1 Motivation	1
1.2 Contributions of this Thesis	3
1.3 Dissertation Outline	4
2 Basic Material	5
2.1 Complex Baseband-Equivalent Model of bandpass transmission systems	5
2.2 Transmission channel for broadband mobile communications	6
2.3 Mitigation to Combat ISI in HSPA+ System and LTE System	7
2.4 Classification of Frequency Synchronization Algorithms	8
3 Impact of Frequency Offset on HSPA+ System	10
3.1 Introduction of HSPA+ System and its Air Interface	10
3.2 Signal Model of HSPA+ System with Frequency Offset	11
3.3 Impacts of Frequency Offset on Demodulator	13
3.3.1 Degradation of Signal-to-Noise Ratio	17
3.3.2 Performance Loss Analysis	19
3.3.2.1 Case I: Ideal Channel Estimation	19
3.3.2.2 Case II: Imperfect Channel Estimation	22
3.3.3 Numerical Results and Simulations	30

3.4	Discussion	33
3.5	Summary	35
4	Impact of Frequency Offset on LTE System	36
4.1	OFDM Signal Model with Frequency Offset	36
4.2	Impact of Frequency Offset on the Output of the Correlator	40
4.3	Discussion of the Impairments caused by the Frequency Offset in LTE system and HSPA+ system	43
4.4	Impact of Frequency Offset on the Uplink of LTE System	45
4.4.1	Matrix Expression of the OFDM System and SC-FDMA System	45
4.4.2	Effect of User-Specific Frequency Offsets on the SC-FDMA system	46
4.5	Summary	51
5	Lower Bounds for Parameter Estimation from Observations of Pilot Signals	52
5.1	Signal Model of the Observations	52
5.2	Lower Bounds for Parameter Estimation	55
5.2.1	PDF and Likelihood Function of the Observations	55
5.2.2	Regularity of the PDF	57
5.2.3	Cramér-Rao Bounds when the interference is absent	58
5.2.4	Lower Bounds for the normal case	60
5.2.4.1	Barankin Bound and its approximations	60
5.2.4.2	Barankin Bound approximation for our signal model	63
5.3	Properties of the Barankin bound for frequency estimation	64
5.4	Parameter selection for frequency estimation	66
5.5	Summary	68
6	Implementation of Frequency Synchronization in HSPA+ System and LTE System	69
6.1	Frequency Synchronization Strategy	70
6.2	Performance Comparison of Frequency Estimation Algorithms	71
6.3	Approximation of the Periodogram Estimate	73
6.4	Temporal-Synchronization-Aided Fast Frequency Acquisition	76
6.5	Slot-Sync-Aided Frequency Acquisition in HSPA+ system	77
6.5.1	Primary Synchronization Channel	78
6.5.2	Optimal Correlation Length in Non-coherent Case	79
6.5.3	Slot Synchronization with Coarse Frequency Offset Estimation	81
6.5.4	Performance Evaluation	82
6.6	Symbol-Sync-Aided Frequency Acquisition in LTE system	85
6.6.1	CP based Method for Symbol Timing Synchronization and FFO Estimation	85
6.6.2	Reference Signal Collection and IFO Estimation	87
6.6.3	RFO Estimation	88

6.6.4	Simulation results	88
6.7	Summary	90
7	Conclusion	91
	Appendices	93
A	Derivation of Equation 3.32	94
B	Derivation of Equation 3.51	95
C	Derivation of ρ and r in Equation 3.55	98
D	Derivation of Equation 3.66	100
E	Parity of $P_M(E z_h, \hat{z}_h, \psi)$ in Equation 3.66	102
F	Derivation of Equation 4.47	103
G	Non-linear Approximation of Barankin Bound	104
	Bibliography	XV

List of Figures

2.1	Tapped delay line model of broadband wireless channel	7
2.2	Power Spectral Density (PSD): OFDM vs. FDM	8
2.3	Typical Signal Flow of Frequency Synchronization Algorithms in a digital receiver	9
3.1	Projected HSPA peak data rate evolution with increased bandwidth and number of antennae. (From <i>Nokia Siemens Networks</i> [2010])	10
3.2	Spreading for all downlink physical channels except SCH. (From <i>3GPP</i> [2008c])	11
3.3	Typical four-finger rake receiver for CDMA system.	12
3.4	SNR Degradation of 64-QAM Signal in HSPA+ System with Frequency Offset	19
3.5	Symbol Error Rate of 64-QAM signal in HSPA+ System with Frequency Offset over an AWGN Channel and a Rayleigh Channel	22
3.6	Signal points for M -ary PAM signals.	24
3.7	Average Receive SINR vs. Average Receive SNR of HSPA+ system with 64-QAM signal under different frequency offsets over a flat Rayleigh fading channel	26
3.8	SER curves comparison: Equation 3.42 in Case I vs. Simulation	31
3.9	SER curves comparison: Numerical Results of Case II.B vs. Simulation	31
3.10	SER curves comparison: Numerical Results of Case II.C vs. Simulation	32
3.11	SER curves comparison: Case I, Case II_B and Case II_C	34
3.12	SER curves comparison: channel estimator with different average lengths	34
4.1	OFDM Symbols in Time Domain	37
4.2	SER curves comparison: channel estimator with different average lengths	44
4.3	Subcarrier Mapping of IFDMA and LFDMA	45
4.4	Example: IFDMA and LFDMA with two UEs	49
4.5	Interference Power to UE1. Parameters: $U = 2$, $\Delta F^{(1,2)} = 10^{-6}$, $N_d = 2048$, $N^{(u)} = 600$, Zeroed DC subcarrier.	50
5.1	Non-regular PDF whose nonzero region depends on the unknown parameters	58
5.2	BB_{Ω} w.r.t. Ω at $\alpha = 1$, $k = 1$, $q = 1$, $M = 32$	65
5.3	BB_{Ω} w.r.t. SNR for different signal models	66
5.4	BB_{Ω} w.r.t. SNR for different M and Ω	67
6.1	Variance of the estimates: $\alpha = 1$, $p = 1$ for BB_{Ω}	73

6.2	Performance comparison for the approximations of PE	75
6.3	LTE FDD Frame: Type I. (From <i>Agilent Technologies</i> [2007])	76
6.4	Block diagram of temporal-synchronization-aided frequency acquisition	77
6.5	Frame and Slot Structure of HSPA+ Downlink Signals	78
6.6	Hierarchical PSC correlator.(64-chip partial correlation)	79
6.7	The function $\lambda(L, f_0)$ for frequency offset $f_0 = 5, 10, \text{ and } 20 \text{ kHz}$	80
6.8	Root Mean Square Error of the coarse frequency estimation	83
6.9	RMSEs and Means of the estimates for $f_0 = 20 \text{ kHz}$	83
6.10	Probability of the frequency estimation error when $f_0 = 20 \text{ kHz}$	84
6.11	Variance of frequency offset estimation in LTE system:	89

List of Tables

3.1	a_m, b_m of 64-QAM	27
3.2	a_m, b_i and c_m of 64-QAM	29
6.1	Simulation parameters for HSPA+ system	82
6.2	Simulation parameters for LTE system	89

List of Acronyms

ACI	Adjacent Channel Interference.
ADC	Analog-to-Digital Conversion.
AWGN	Additive White Gaussian Noise.
BB	Barankin Bound.
BER	Bit Error Rate.
BOF	Boundary of Frame.
BOHF	Boundary of Half Frame.
BOS	Boundary of Slot or Boundary of Symbol.
BS	Base Station.
CP	Cyclic Prefix.
CPICH	Common Pilot Channel.
CRB	Cramér-Rao Bound.
CS	Circuit-Switched.
DA	Data-Aided.
DD	Detection-Directed.
DFE	Decision Feedback Equalizer.
DFT	Discrete Fourier Transform.
DPCH	Dedicated Physical Channel.
DSP	Digital Signal Processing.
DSSS	Direct-Sequence Spread-Spectrum.
DTFT	Discrete-Time Fourier Transform.
DVB	Digital Video Broadcasting.
EGC	Equal Gain Combining.
FDM	Frequency Division Multiplexing.
FFO	Fractional Frequency Offset.
FFT	Fast Fourier Transform.

GSM	Global System for Mobile Communications.
HR	Hybrid Region.
HS-PDSCH	High Speed Physical Downlink Shared Channel.
HSPA+	Evolved High-Speed Packet Access.
ICI	Inter-Carrier Interference.
ICI	Inter-Channel Interference.
IDR	Interference Dominant Region.
IFDMA	Interleaved Frequency Domain Multiple Access.
IFO	Integer Frequency Offset.
IPTV	Internet Protocol Television.
ISI	Inter-Symbol Interference.
ITU	International Telecommunication Union.
LFDMA	Localized Frequency Domain Multiple Access.
LMVU	Locally Minimum Variance Unbiased.
LOS	Line Of Sight.
LR	Likelihood Ratio.
LS	Least-squares.
LTE	Long Term Evolution.
LTV	Linear Time Variant.
MAI	Multiple Access Interference.
MIMO	Multiple Input Multiple Output.
MLE	Maximum Likelihood Estimator.
MLSE	Maximum-likelihood Sequence Estimation.
MMS	Multimedia Messaging Service.
MMSE	Minimum Mean Square Error.
MRC	Maximal Ratio Combining.
MSE	Mean Square Error.
NDA	Non-Data-Aided.
NDR	Noise Dominant Region.
OCNS	Orthogonal Channel Noise Simulator.
OFDM	Orthogonal Frequency Division Multiplexing.
OFDMA	Orthogonal Frequency Division Multiple Access.
OVSF	Orthogonal Variable Spreading Factor.

P-SCH	Primary Synchronization Channel.
P2P	Point-to-Point.
PAPR	Peak-to-Average Power Ratio.
PDF	Probability Density Function.
PLL	Phase Lock Loop.
PS	Packet-Switched.
PSC	Primary Synchronization Code.
PSCFD	Parabolic Smoothed Central Finite Difference Estimator.
QPSK	Quadrature Phase-Shift Keying.
RF	Radio Frequency.
RFO	Residual Frequency Offset.
RHS	Right Hand Side.
RMSE	Root Mean Square Error.
S-SCH	Secondary Synchronization Channel.
SAE	System Architecture Evolution.
SC-CDMA	Single Carrier Code Division Multiple Access.
SC-FDMA	Single Carrier Frequency Division Multiple Access.
SCH	Synchronization Channel.
SER	Symbol Error Rate.
SF	Spreading Factor.
SINR	Signal-to-Interference-plus-Noise Ratio.
SNR	Signal-to-Noise Ratio.
TDM	Time Division Multiplex.
UE	User Equipment.
UMTS	Universal Mobile Telecommunications System.
VoIP	Voice over IP.
WCDMA	Wideband Code Division Multiple Access.
ZF	Zero Forcing.

List of Symbols

ω_c	Carrier angular frequency
$s_L(t)$	Equivalent baseband representation of the signal $s(t)$
$s_T[n]$	Samples of the transmitted signal
$s_R[n]$	Samples of the received signal
S_c	Scrambling code for the cell c
C_{m_k}	Spreading code of channel k
Δf	Absolute frequency offset
ΔF	Frequency offset normalized to the sampling frequency
$\Delta \mathcal{F}$	Frequency offset normalized to the symbol rate of one channel(subcarrier)
W_P	Spreading factor of channel P
N_g	Length of the Cyclic Prefix
N_d	Length of the payload part of one OFDM symbol
N_s	Length of one OFDM symbol
$\delta_{p,q}$	Kronecker delta
β	Amplitude attenuation factor caused by frequency offset
$H(\Omega)$	Frequency response of the transmission channel $h(t)$
$Q(x)$	Tail probability of the standard normal distribution
σ_d^2	Variance of the data symbols
σ_v^2	Variance of the additive Gaussian noise v
σ_χ^2	Variance of the interference plus noise term χ
γ_b	Received SNR per bit
\mathbf{K}_χ	Covariance matrix of the interference plus noise vector χ
\mathbf{I}	Identity matrix
\mathbf{p}	Phase rotation vector
\mathbf{J}	Fisher information matrix
$E[x]$	Expectation of random variable x
$\Re[z]$	Real part of complex value z
$\Im[z]$	Imaginary part of complex value z
$f(\mathbf{z}; \boldsymbol{\eta})$	Joint probability density function of the observation vector \mathbf{z}
$L(\boldsymbol{\eta} \mathbf{z})$	Log-likelihood function of $f(\mathbf{z}; \boldsymbol{\eta})$
BB_Ω	Barankin bound of frequency offset Ω

Chapter 1

Introduction

1.1 Motivation

In the second half of the 19th century, wireline telegraphy and telephony changed the nature of communications. Within a few years, the movement of information had gone from the speed of people to the speed of light. Then, in the 20th century, the second revolution took place, as radio freed those same communications from the constraint of a wire.

Although the first generation mobile communication systems were deployed as early as in 1950s, they did not profoundly get involved in people's daily life. Their analog systems were incapable of providing enough system capacity to serve the whole population with an affordable cost. The situation was changed with the development of the *Microelectronics* technology and the *Digital Signal Processing (DSP)* technology. Digital wireless communication systems with a *cellular* network were proposed to boost the system capacity for people's basic communication requirement, i.e. voice service. In 1990s, two different second generation (2G) digital cellular systems, i.e. *Global System for Mobile Communications (GSM)* and *Interim Standard 95 (cdmaOne)* were deployed in Europe and the U.S. respectively. Especially, the GSM system was accepted almost all over the world. Until July 2001 GSM system is used by 70% of subscribers worldwide.

Almost at the same time, another revolutionary technique intervened in our lives gradually since 1990s. It is the *Internet*. Internet extraordinarily extends means of exchanging and accessing information. Numerous innovative services and different business models are created based on the Internet. The influence of the Internet has caused a change in the way we communicate, learn and shop. By now, Internet has become important part of our daily lives. Meanwhile, the Internet boom also challenges the communication technology with its sempiternal growing data-rate requirements.

With a growing number of consumers utilizing the Internet, industries have foreseen a consumer demand for high-speed wireless access. Although initial email and Internet-based services have been offered in them, voice-service-oriented 2G mobile communication systems are incapable to fulfill the requirements from the upcoming high-speed, *Packet-Switched (PS)* Internet services because of its narrowband nature and *Circuit-Switched (CS)* technology. To provide worldwide access and global roaming for a wide range of services, *International Telecommunication Union (ITU)* developed the third generation (3G) mobile communication system – *Universal Mobile Telecommunications System*

(UMTS) in the late 1990s to support higher system throughput and to provide efficient solutions to handle both CS and PS services. Today there are more than 490 commercial 3G/UMTS networks operating commercially in around 174 countries.

Over the last two decades, mobile networks have enabled dramatic advances and changes in telecommunications and mobile operators have grown to dominate the industry, offering their subscribers a service set as rich as their wireline competitors, plus mobility. As we are getting experienced using mobile handsets in our daily lives, we are living in a convergence period with mobile communication, Internet, computing and broadcasting. The introduction of wireless Internet is driving digital convergence in all conceivable areas, including *Digital Video Broadcasting (DVB)*, *Point-to-Point (P2P)* multimedia communications, *Multimedia Messaging Service (MMS)*, *Internet Protocol Television (IPTV)*, digital camera, games, and cell phones. In addition to enabling fixed to mobile migrations of Internet applications such as *Voice over IP (VoIP)*, video streaming, music downloading, mobile TV and many others, mobile communication systems face the challenge to provide enough capacity to support an explosion in demand for connectivity from a new generation of consumer devices tailored to those new mobile applications.

To satisfy the demand for higher data rates and larger capacity coming with this convergence, the throughput over the existing transmission media has to be increased. In the latest evolution of the 3G system – HSPA+ system and the upcoming fourth generation (4G) system – 3GPP LTE system, several techniques are proposed to boost up the system throughput: broader transmission band and higher order modulation for high speed transmission, multi-carrier system to combat selective fading, spatial multiplexing transmission to increase the capacity of wireless links, iteratively decodable codes (e.g., turbo codes and LDPC codes) to improve the quality of the link, and so forth.

No matter what kind of advanced techniques the system employs, to function properly, the receiver must synchronize with the incoming signal. The accuracy of the synchronization will determine whether the real system is able to achieve the designed capacity. Many books and volume of papers address synchronization problem in versatile wireless communication systems because of the following reasons:

- Error performance: Synchronization is critical to error performance;
- Design effort: A large amount of design time is spent in solving synchronization problems;
- Implementation: A very large portion of the receiver hardware and software is dedicated to synchronization.

To discuss the synchronization problem in communication systems, questions come out naturally as follows:

- **How does synchronization affect the system performance?**
- **What are key problems in synchronization?**
- **How can we design the synchronizer to fulfill the system requirement?**

In particular, this dissertation is devoted to the study of frequency synchronization in the two latest broadband mobile communication systems – HSPA+ system and LTE system. While the impacts of frequency offset on an *Single Carrier Code Division Multiple Access (SC-CDMA)* system have been studied in [Viterbi, 1995] and [Liu et al., 2011], the adoption of advanced techniques makes HSPA+ system more sensitive to the frequency error than its ancestor. The special system properties of HSPA+ system are not taken into account in the previous discussion and the analytical analysis of the impacts on the performance of HSPA+ system caused by frequency offset is still missing.

In principle, HSPA+ system belongs to *Single-Carrier* systems and LTE system belongs to *Multi-Carrier* systems. Although frequency synchronization has been intensively discussed for SC-CDMA systems in [Wang and Ottosson, 1999], [Wang and Ottosson, 2000] and [Korde and Gandhi, 2012], and for OFDM systems in [Pollet et al., 1995], [Pollet and Moeneclaey, 1996], [Luise and Reggiani, 1996] and [Toumpakaris et al., 2009], the studies were conducted distinguishingly on the two kinds of systems. I am stimulated to investigate the impacts of the frequency offset on both HSPA+ and LTE systems uniformly by the demand of multi-standard receiver design.

The main objective of this study is to create an infrastructure to analyze the impact of the frequency synchronization error on the system performance and the theoretical bound for frequency offset estimation in both systems. Furthermore, the theoretical results are used to direct the implementation of the frequency synchronizer.

1.2 Contributions of this Thesis

The original contributions of this thesis are highlighted as follows:

- **Error rate analysis for HSPA+ system** – An exact *Symbol Error Rate (SER)* analysis for HSPA+ system is presented by taking into account the *Inter-Channel Interference (ICI)* and the channel estimation error caused by the frequency offset.
- **General signal model for HSPA+ system and LTE system** – A general signal model with the impact of frequency offset is given for both HSPA+ system and LTE system. Based on this general signal model, the SER analysis method for HSPA+ system is extended to LTE system.
- **MAI of LTE system caused by frequency offset** – The *Single Carrier Frequency Division Multiple Access (SC-FDMA)* technique is adopted for LTE uplink air interface. Based on the proposed framework in [Wilzeck et al., 2007], the *Multiple Access Interference (MAI)* caused by user-specific frequency offset is analyzed and compared for different subcarrier allocation schemes in the SC-FDMA system.
- **Lower Bound for frequency offset estimation** – Because of the non-regularity property, the **CRB**, which establishes a fundamental lower limit to the variance of any unbiased estimator usually serves as a benchmark for performance evaluation purposes, does not exist for the general signal model. Therefore, the **BB** is derived to give a theoretical lower bound for unbiased

frequency offset estimation, whose existence does not depend on the regularity condition of the signal model.

- **Uniform implementation structure for frequency offset estimation** – Based on the general signal model an uniform implementation structure for frequency offset estimation is proposed to HSPA+ system and LTE system, which could help to simplify the design of frequency synchronizer in a multi-standard receiver.

1.3 Dissertation Outline

The rest of this dissertation is organized as follows:

In Chapter 2, we introduce the basics of broadband wireless communications. Besides the modeling of broadband wireless transmission channel, the main investigation objectives, i.e. the air interfaces for HSPA+ system and LTE system are described here respectively.

In Chapter 3, we analyze the impact of frequency offset on HSPA+ system. The ICI caused by frequency offset in HSPA+ system is derived. Not only the ICI, but also the channel estimation error caused by frequency offset are involved in an exact analytical SER analysis for HSPA+ system.

In Chapter 4, the *Inter-Carrier Interference (ICI)* is derived based on OFDM signal model with frequency offset. By comparing the expressions of the received signals in HSPA+ system and in LTE system, a general signal model for the received signals is proposed and then the analytical SER analysis is generalized for both systems. The impact of the frequency offset on SC-FDMA system is also discussed in this chapter, which is adopted in LTE uplink air interface. The MAI caused by user-specific frequency offset is derived for two different resource allocation schemes, i.e. *Localized Frequency Domain Multiple Access (LFDMA)* and *Interleaved Frequency Domain Multiple Access (IFDMA)*.

In Chapter 5, we make effort to obtain a fundamental lower limit to the variance of unbiased frequency offset estimators for HSPA+ system and LTE system. If the observations for estimation are only corrupted by *Additive White Gaussian Noise (AWGN)*, the CRB can be derived to establish the fundamental limit to the variance of any unbiased estimator. However, the observations are contaminated not only by the noise, but also by the interference, when the synchronization of the system is not ideal. According to the general signal model, the statistic property of the observations in HSPA+ system and LTE system does not satisfy the regularity requirement for the existence of the CRB. Therefore, the Barankin Bound is derived based on the general signal model for the observations.

In Chapter 6, different algorithms for frequency offset estimation are evaluated. The parameters for algorithms are selected according to the theoretical lower bound for the estimation and the system performance requirement discussed in Chapter 4 and the best algorithm is chosen. Furthermore, based on the common signal model, an uniform structure is proposed to simplify the implementation of frequency synchronizer in a multi-standard receiver for HSPA+ system and LTE system.

In Chapter 7, we present the conclusions.

Chapter 2

Basic Material

2.1 Complex Baseband-Equivalent Model of bandpass transmission systems

Any bandpass signal can be expressed in terms of a carrier frequency:

$$s(t) = A(t) \cos(\omega_c t + \phi(t)) \quad (2.1)$$

where ω_c denotes the carrier frequency, $A(t)$ is the amplitude of the signal, and $\phi(t)$ is the relative phase of the signal relative to the phase of the carrier, both being function of time.

This signal $s(t)$ can also be written as the real part of a complex variable, for which we are free to define the imaginary part any way we like. However, there is a standard complex exponential way of representing frequencies which allows a particularly simple and convenient notation, and this suggests using:

$$s(t) = \Re [A(t) \cos(\omega_c t + \phi(t)) + jA(t) \sin(\omega_c t + \phi(t))] \quad (2.2)$$

let $s_L(t) = A(t)e^{j\phi(t)}$, and we get

$$s(t) = \Re [s_L(t)e^{j\omega_c t}] \quad (2.3)$$

$s_L(t)$ is known as the equivalent baseband representation of the signal, and in some books also referred as *Complex Envelope Representation* of the bandpass signal.

Meanwhile, any *real* linear system may be described by its impulse response $h(t)$ or by its frequency response $H(\omega)$, which holds

$$H^*(-\omega) = H(\omega) \quad (2.4)$$

Let us define $H_L(\omega - \omega_c)$ as

$$H_L(\omega - \omega_c) = \begin{cases} H(\omega) & (\omega > 0) \\ 0 & (\omega < 0) \end{cases} \quad (2.5)$$

Then we have [*Proakis, 2000*]

$$h(t) = 2\Re [h_L(t)e^{j\omega_c t}] \quad (2.6)$$

where $h_L(t)$ is the inverse Fourier transform of $H_L(\omega)$ and it is the baseband equivalent expression of $h(t)$.

If a bandpass signal $s(t)$ passes through a bandpass transmission channel $h(t)$, the output signal $r(t)$ can be represented as

$$r(t) = \Re \left[r_L(t) e^{j\omega_c t} \right] \quad (2.7)$$

where $r_L(t)$ is the baseband equivalent expression of $r(t)$ and it is given by the convolution of $s_L(t)$ with $h_L(t)$ as

$$r_L(t) = s_L(t) * h_L(t) = \int_{-\infty}^{\infty} s_L(\tau) h_L(t - \tau) d\tau \quad (2.8)$$

The combination of Equation 2.7 with 2.8 allows us to ignore any linear frequency translations encountered in the modulation of a signal for purposes of matching its spectral content to the frequency allocation of a particular channel. Thus, for mathematical convenience, we shall deal only with the transmission of equivalent baseband signals through equivalent baseband channels [Proakis, 2000].

Therefore, further discussions in this thesis are based on the baseband equivalent expression of the system, if not specially mentioned.

2.2 Transmission channel for broadband mobile communications

The performance of a broadband mobile communication system is greatly influenced by the characteristics of the transmission channel. Not like the free space where there are few obstacles, many obstacles normally locate in mobile communication channels such as buildings, roads, trees, cars, even people. Electromagnetic waves are reflected, refracted or diffracted by those obstacles. As a result, the receiver sees the superposition of multiple copies of the transmitted signal, each traversing a different path. Each signal copy will experience differences in attenuation, delay and phase shift while traveling from the source to the receiver. This can result in either constructive or destructive interference, amplifying or attenuating the signal power seen at the receiver. Strong destructive interference is frequently referred to as a deep fade and may result in temporary failure of communication due to a severe drop in the channel signal-to-noise ratio.

The difference of the maximum path delay and the minimum path delay is termed as *maximum excess delay* τ_{\max} . If the maximum excess delay is much smaller than the reciprocal of the receiver bandwidth W , the receiver would not distinguish the signals from different paths. Then, from the receiver point of view, the channel is a narrowband channel. Conversely, if $\tau_{\max} > \frac{1}{W}$, the channel is seen as a broadband channel [Molisch, 2000]. If we change our view to frequency domain, the correlation bandwidth of a time dispersion channel and the maximum excess delay are inversely proportional. Then, a narrowband mobile channel exhibits statistically *frequency-nonselective* fading. However, a broadband mobile channel manifests *frequency-selective* fading.

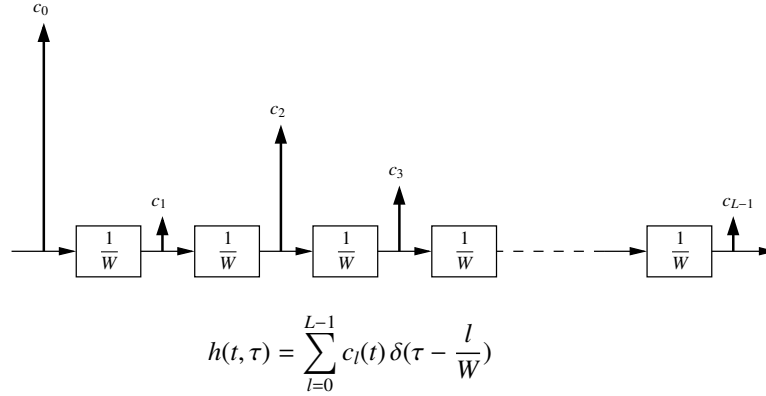


Figure 2.1: Tapped delay line model of broadband wireless channel

When $\tau_{\max} \gg \frac{1}{W}$, one way to present the impulse response of a multipath channel is by a discrete number of impulses as follow [Proakis, 2000]

$$h(t, \tau) = \sum_{l=0}^{L-1} c_l(t) \delta(\tau - \frac{l}{W}) \quad (2.9)$$

The maximum excess delay is assumed over L pulse duration in Equation 2.9. Note that the impulse response is expressed as a *Linear Time Variant (LTV)* function because the coefficients $c_l(t)$ vary with time. This model represents the channel by a tapped delay line with L taps as shown in Figure 2.1.

The time-variant tap weights $\{c_l(t)\}$ are complex-valued stationary random processes. In the special case of *Rayleigh* fading, the magnitude $|c_l(t)| \equiv \alpha_l(t)$ are Rayleigh-distributed and the phase $\phi_l(t)$ are uniformly distributed. Moreover, under the uncorrelated scattering assumption $\{c_l(t)\}$ are mutually uncorrelated [Proakis, 2000].

2.3 Mitigation to Combat ISI in HSPA+ System and LTE System

With a broadband wireless channel, the signal echos at the receiver extend over more than one period of system symbol duration and causes *Inter-Symbol Interference (ISI)* problem. The ISI seriously degrades the system performance and it must be canceled or avoided for broadband mobile communications in order to ensure the system throughput.

The common techniques to combat ISI for broadband wireless communications have been introduced in [Sklar, 2001], which include the *Decision Feedback Equalizer (DFE)*, a *Maximum-likelihood Sequence Estimation (MLSE)* Equalizer, *Direct-Sequence Spread-Spectrum (DSSS)* techniques, *Orthogonal Frequency Division Multiplexing (OFDM)*, and so on.

HSPA+ is a wireless broadband standard defined in 3GPP release 7 and above. It is a smoothly evolved system to the initial third generation system. *Wideband Code Division Multiple Access (WCDMA)* technique is employed for the air interface of the system, which essentially utilizes DS/SS

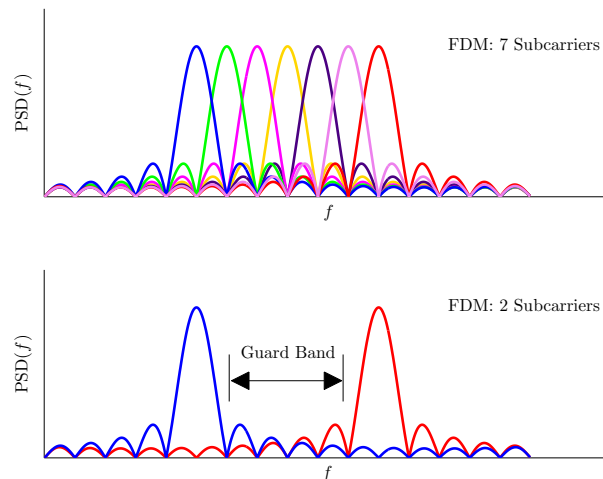


Figure 2.2: Power Spectral Density (PSD): OFDM vs. FDM

technique. By virtue of the scrambling codes with small off-peak autocorrelation values, WCDMA systems enable the receiver to eliminate the ISI by using the code-correlator and to convert a frequency selective fading channel to multiple flat fading channels by virtue of *Rake* receiver [Turin, 1980].

OFDM technique is adopted in the air interface of LTE system. Not like the DS/SS techniques in WCDMA system, which use the time-domain methods to combat ISI, OFDM technique utilizes the frequency-domain methods to divide a frequency-selective broadband transmission channel to multiple parallel flat narrowband transmission channels. Therefore, a high-rate transmission can be achieved by combining multiple low-rate transmissions over the parallel flat narrowband channels. Because of less ISI in narrowband transmission, complex time-domain equalizers could be saved in the receiver.

Compared to the normal *Frequency Division Multiplexing (FDM)* techniques, the specificity of OFDM technique is that the signal band is made up of orthogonal carrier waves to allow overlapping the narrowband channels in an intended way, as shown in Figure 2.2. Under the ideal synchronization conditions, the signal overlapping will not generate interference so as to achieve much better spectrum efficiency than the normal FDM system, in which the guard band must be placed between the adjacent carriers in order to avoid the *Adjacent Channel Interference (ACI)*.

2.4 Classification of Frequency Synchronization Algorithms

The typical signal flow of the frequency synchronization algorithms in a digital receiver is shown in Figure 2.3. The feed-back signal paths are marked with dashed lines. If the frequency estimation algorithm needs the synchronization signal which is transmitted specially for helping estimation process, it is called *Data-Aided (DA)* algorithm, otherwise if the algorithm achieves the estimate directly

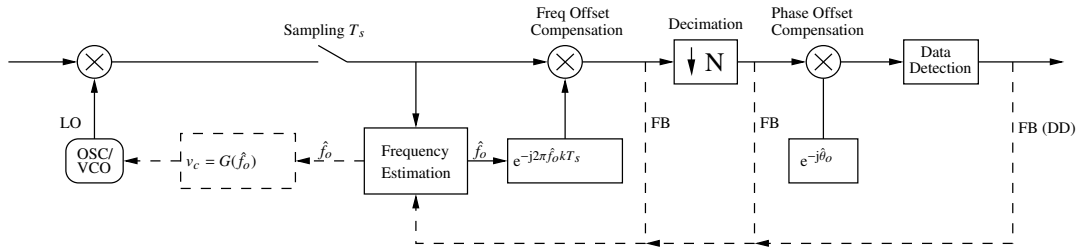


Figure 2.3: Typical Signal Flow of Frequency Synchronization Algorithms in a digital receiver

from the received data signals, it belongs to *Non-Data-Aided (NDA)* algorithm. If the frequency synchronization algorithm has only the *feed-forward* signal paths marked with solid lines, it is therefore an *open-loop* algorithm. Otherwise, it is a *closed-loop* algorithm, if it is equipped with any *feed-back* signal path marked with dashed line. Furthermore, if the feed-back signals include the results of the data detection unit, the algorithm is *Detection-Directed (DD)*.

In civil communication system, data-aided algorithms are widely used to guarantee the system performance because of their great performance advantage to non-data-aided algorithms. Therefore, only data-aided algorithms are taken into account in our discussion. For frequency offset estimation, high resolution has normally contrary requirements to large non-ambiguous range, i.e. the variance of the estimation error is bigger, if the non-ambiguous range of the frequency offset estimation is larger. Hence, frequency offset estimation consists commonly of two steps: coarse estimation and fine estimation. Coarse estimation obtains the frequency offset with bigger granularity. The compensation unit uses the coarse estimation result to limit the residual frequency offset in a much smaller frequency range to enable the fine estimation to further derive the residual frequency offset with much smaller granularity. The combination of the results from both coarse estimation and fine estimation thus provides us an frequency offset estimate with enough accuracy for the system.

Chapter 3

Impact of Frequency Offset on HSPA+ System

3.1 Introduction of HSPA+ System and its Air Interface

HSPA+ system is a smoothly evolved system to the initial third generation system – UMTS system. Although it follows the same air interface technology of UMTS system, it provides much higher data rate through the use of advanced wireless techniques, such as higher order modulation, *Multiple Input Multiple Output (MIMO)* technique and carrier combination. Figure 3.1 depicts the peak data rate evolution of HSPA+ system.

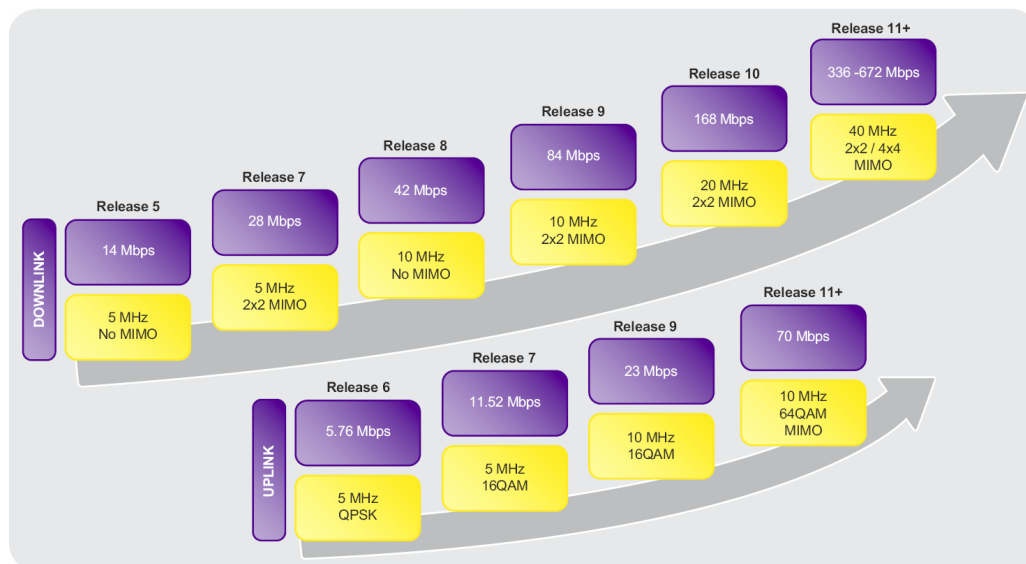


Figure 3.1: Projected HSPA peak data rate evolution with increased bandwidth and number of antennae. (From *Nokia Siemens Networks* [2010])

As same as UMTS system, WCDMA techniques are used to construct the air interface of HSPA+ system. The block diagram of spreading and modulation for all downlink physical channels is shown in Figure 3.2, except *Synchronization Channels (SCHs)*. The whole process includes symbol mapping, spreading, scrambling and channel combining. From signal format point of view, there exist two

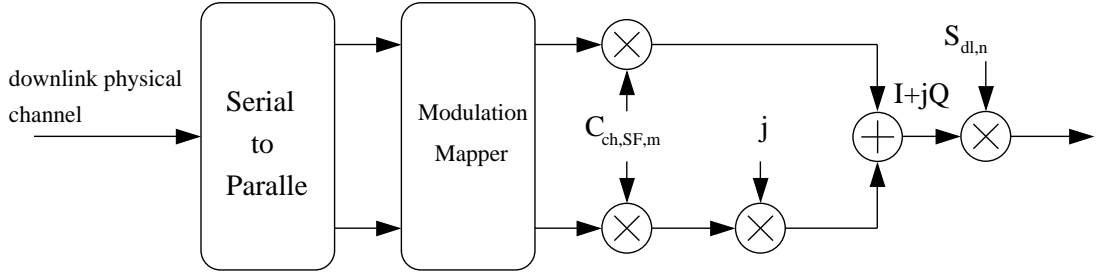


Figure 3.2: Spreading for all downlink physical channels except SCH. (From *3GPP* [2008c])

major differences between the HSPA+ system and its predecessor: 1. HSPA+ introduces 64-QAM modulation to the modulation mapper; 2. all the service channels, i.e. *High Speed Physical Downlink Shared Channels* (HS-PDSCHs), use the spreading codes with the same *Spreading Factor* (SF), i.e. $SF = 16$.

The spreading codes here, also known as channelization codes, are *Orthogonal Variable Spreading Factor* (OVSF) codes. The spreading factor varies from 16 to 512. According to the DSSS communication theory, given a fixed chip rate, the channel with smaller spreading factor provides larger throughput at the cost of a smaller processing gain.

3.2 Signal Model of HSPA+ System with Frequency Offset

For analyzing the impact of frequency offset on the system performance, the signal model of the transmit and receive system is established as a basis for discussions. The discussion is limited in a single cell and the inter-cell interference is not taken into account in order to simplify the analysis.

As shown in Figure 3.2, the information bits carried by a downlink physical channel are first grouped by serial to parallel processing and then the bit groups are mapped to complex signal symbols via the modulation mapper. The real part and the imaginary part of the complex signal symbols are multiplied with the identical channelization code to accomplish the spectrum spreading process. Finally, the generated complex signal is multiplied with the downlink scrambling code, which is used to distinguish the downlink signals from different cells. The signals of all downlink physical channels are added together with their own weight factors and further sent out through the antenna port. The signal sampled at the chip rate is expressed as

$$s_T[n] = \sum_{k=0}^{K-1} d_k \left[\left\lfloor \frac{n}{W_k} \right\rfloor \right] \cdot C_{m_k}[n] \cdot S_c[n] \cdot G_k \quad (3.1)$$

where $\lfloor \cdot \rfloor$ operator takes the integer part of the operand, k is the index of the downlink physical channel and K denotes the total number of downlink physical channels in the cell, d_k is the complex signal symbol out from the modulation mapper block for the k -th downlink physical channel, W_k indicates the spreading factor of the channel k , C_{m_k} stands for the spreading code of channel k , G_k is the weight factor of channel k and S_c refers to the scrambling code for the cell c . Considering the signal pulse

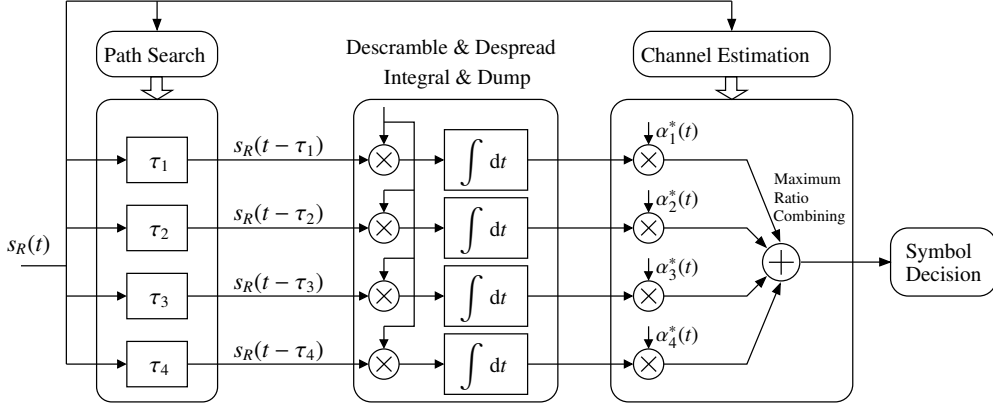


Figure 3.3: Typical four-finger rake receiver for CDMA system.

shape $g(t)$, the baseband transmit signal can be expressed as [Proakis, 2000]

$$s_T(t) = \sum_{n=-\infty}^{+\infty} s_T[n] \cdot g(t - nT_c) \quad (3.2)$$

where T_c is the *chip interval* of the system.

The *Radio Frequency (RF)* modulator takes the baseband signal and generates the band-limited broadcast signal. The broadcast signal passes through a wireless channel and is received by the receiver of the *UE*. The receiver first downconverts the RF signal to baseband for the further processing.

The received signal may be represented in the baseband equivalent representation as

$$s_R(t) = s_T(t) * h(t) \cdot e^{j2\pi\Delta f t} + \eta(t) \quad (3.3)$$

where $*$ denotes linear convolution, $s_T(t)$, $h(t)$ and $\eta(t)$ represent the transmit signal, the passband wireless channel and the passband Gaussian noise process in the equivalent baseband form respectively, Δf is frequency offset between transmitter and receiver.

As discussed in Chapter 2, a tapped delay line model can be used to describe the baseband equivalent of the broadband wireless channel in multipath wireless environment. Without loss of generality, assuming L channel taps, the channel can be expressed as

$$h(t) = \sum_{l=0}^{L-1} \alpha_l(t) e^{j\phi_l(t)} \delta(t - \tau_l) \quad (3.4)$$

where $\alpha_l(t)$, $\phi_l(t)$ and τ_l are amplitude, phase and tap delay of the l -th channel tap respectively, $\delta(t)$ is the Dirac delta function. By substituting Equation 3.4 into 3.3 we obtain the received signal as

$$s_R(t) = e^{j2\pi\Delta f t} \sum_{l=0}^{L-1} \alpha_l(t) e^{j\phi_l(t)} s_T(t - \tau_l) + \eta(t) \quad (3.5)$$

3.3 Impacts of Frequency Offset on Demodulator

To combat frequency selective fading channel, the rake architecture in Figure 3.3 is adopted in the receiver. Under the assumption of ideal timing synchronization, each finger of the rake works as an optimum demodulator for a frequency flat fading channel $\alpha_l(t)e^{j\phi_l(t)}$. Therefore, the impact of frequency offset on the performance of an optimum receiver for a frequency flat fading channel is the basis to analyze the performance degradation of the system with frequency offset. Next we discuss this impact in detail.

By frequency flat fading channel, i.e. $L = 1$, assuming that the timing synchronization is perfect and the channel is time-invariant in observation, then Equation 3.5 can be simplified to

$$s_R(t) = e^{j2\pi\Delta f t} \alpha e^{j\phi} s_T(t) + \eta(t) \quad (3.6)$$

After *Analog-to-Digital Conversion* (ADC) we obtain the samples as

$$s_R[n] = e^{j2\pi\Delta F n} \alpha e^{j\phi} s_T[n] + \eta[n] \quad (3.7)$$

where $\Delta F = \frac{\Delta f}{f_{\text{sampling}}}$ and f_{sampling} is the sampling frequency for the detection. In our analysis the sampling rate is set to the chip rate of the system, i.e. $f_{\text{sampling}} = f_{\text{chip}}$. To detect the information carried by the P -th physical channel, the decision symbol is obtained by first descrambling and then despreading the received samples with the spreading code for channel P , which may be expressed as

$$\tilde{d}_P[i] = \frac{1}{W_P} \sum_n s_R[n] \cdot S_c^*[n] \cdot C_{m_P}[n] \quad (3.8)$$

Substituting Equation 3.1 and 3.7 to Equation 3.8 we obtain

$$\begin{aligned} \tilde{d}_P[i] &= \frac{1}{W_P} \sum_{n=iW_P}^{(i+1)W_P-1} s_R[n] \cdot S_c^*[n] \cdot C_{m_P}[n] \\ &= \alpha e^{j\phi} G_P e^{j2\pi W_P \Delta F i} \frac{1}{W_P} \sum_{n=0}^{W_P-1} e^{j2\pi \Delta F n} d_P[i] C_{m_P}[n] S_c[n] S_c^*[n] C_{m_P}[n] \\ &\quad + \alpha e^{j\phi} G_k e^{j2\pi W_P \Delta F i} \frac{1}{W_P} \sum_{n=0}^{W_P-1} (e^{j2\pi \Delta F n} \sum_{k \neq P} d_k[i] C_{m_k}[n] S_c[n]) S_c^*[n] C_{m_P}[n] \\ &\quad + \frac{1}{W_P} e^{j2\pi W_P \Delta F i} \sum_{n=0}^{W_P-1} e^{j2\pi \Delta F n} \eta[n] S_c^*[n] C_{m_P}[n] \end{aligned} \quad (3.9)$$

The power of the scrambling code $E_{sc} = S_c[n] S_c^*[n]$ is constant. Without loss of generality, we assign

$E_{sc} = 1$. Thus, the above equation becomes

$$\begin{aligned} \tilde{d}_p[i] &= \alpha e^{j\phi} G_k e^{j2\pi W_p \Delta F i} d_p[i] \frac{1}{W_p} \sum_{n=0}^{W_p-1} e^{j2\pi \Delta F n} C_{m_p}[n] C_{m_p}[n] \\ &+ \alpha e^{j\phi} G_k e^{j2\pi W_p \Delta F i} \frac{1}{W_p} \sum_{\substack{k=0 \\ k \neq p}}^K \sum_{n=0}^{W_p-1} d_k[i] e^{j2\pi \Delta F n} C_{m_k}[n] C_{m_p}[n] \\ &+ \frac{1}{W_p} e^{j2\pi W_p \Delta F i} \sum_{n=0}^{W_p-1} e^{j2\pi \Delta F n} \eta[n] S_C^*[n] C_{m_p}[n] \end{aligned} \quad (3.10)$$

From the *Right Hand Side (RHS)* of Equation 3.10, it is obvious that the decision symbol consists of three parts. The first part comes from the desired data symbol $d_p[i]$, the second part is contributed by the data symbols from other physical channels, which is referred to ICI, and the third part are from the Gaussian noise in band.

The channelization code C_{m_k} is also called orthogonal variable spreading code. The codes generated from different roots are orthogonal. If the codes C_{m_p} and C_{m_q} belong to the same code level, i.e. they have the same spreading factor $SF = W$, the orthogonal property can be expressed as [Feng et al., 2007]

$$\sum_{n=0}^{W-1} C_{m_p}[n] C_{m_q}[n] = W \delta_{p,q} \quad (3.11)$$

where $\delta_{p,q}$ is the *Kronecker delta* and it is defined as

$$\delta_{p,q} = \begin{cases} 1, & p = q \\ 0, & p \neq q \end{cases}$$

Because of the orthogonal property of the spreading code, in the case of none frequency offset, Equation 3.10 degenerates to

$$\begin{aligned} \tilde{d}_p[i] &= \alpha e^{j\phi} G_k d_p[i] + \frac{1}{W_p} \sum_{n=0}^{W_p-1} e^{j2\pi \Delta F n} \eta[n] S_C^*[n] C_{m_p}[n] \\ &= \alpha_E e^{j\phi} d_p[i] + \eta_E[i] \end{aligned} \quad (3.12)$$

where α_E is the combined amplitude factor of the fading factor and gain factor. $\eta_E[i]$ is the effective additive noise and it is the linear combination of the noise samples $\eta[n]$. In the analysis $\eta[n]$ are assumed as i.i.d. zero-mean circular symmetric complex Gaussian random variables with the same variance σ_η^2 . According to the properties of the circular symmetric Gaussian random variable [Gallager, 2008a], $\eta_E[i]$ is also a circular symmetric Gaussian random variable with zero-mean and variance $\frac{\sigma_\eta^2}{W_p}$.

In the case of perfect synchronization, it can be seen that the orthogonal property of the spreading code ensures that the decision symbol is affected only by channel effects and channel noise. However,

the perfect synchronization will never exist in the real world. When the frequency offset exists, it causes the spreading codes of the different physical channels to lose their orthogonality, as shown in Equation 3.13. Hence, in despreading a given physical channel's waveform, nonzero contributions to that channel's signal, i.e. the second part of the RHS in Equation 3.10, arise from the transmissions of the other channels.

$$\begin{aligned} \frac{1}{W} \sum_{n=0}^{W-1} e^{j2\pi\Delta F n} C_{m_k}[n] C_{m_p}[n] &= \begin{cases} \frac{1}{W} \sum_{n=0}^{W-1} e^{j2\pi\Delta F n}, & k = P \\ \frac{1}{W} \sum_{n=0}^{W-1} e^{j2\pi\Delta F n} C_{m_k}[n] C_{m_p}[n], & k \neq P \end{cases} \\ &= \begin{cases} \frac{\sin(\pi\Delta F W)}{W \sin(\pi\Delta F)} e^{j2\pi\Delta F(W-1)}, & k = P \\ \frac{1}{W} \sum_{n=0}^{W-1} e^{j2\pi\Delta F n} C_{m_k}[n] C_{m_p}[n], & k \neq P \end{cases} \end{aligned} \quad (3.13)$$

Combining Equation 3.13 and Equation 3.10, the decision symbol of the desired channel P can be expressed as

$$\tilde{d}_P[i] = \alpha_E e^{j\phi} \frac{\sin(\pi\Delta F W_P)}{W_P \sin(\pi\Delta F)} e^{j2\pi\Delta F(W_P-1)} e^{j2\pi W_P \Delta F i} d_P[i] + ICI_P[i] + \eta_E[i], \quad (3.14)$$

and the term $ICI_P[i]$ in the equation is defined by

$$ICI_P[i] = \alpha_E e^{j\phi} e^{j2\pi W_P \Delta F i} \frac{1}{W_P} \sum_{\substack{k=0 \\ k \neq P}}^{K-1} \sum_{n=0}^{W_k-1} d_k[i] e^{j2\pi\Delta F n} C_{m_k}[n] C_{m_p}[n] \quad (3.15)$$

where $\alpha_E = \alpha G_k$.

Comparing Equation 3.14 to Equation 3.12, we can summarize the impacts of the frequency offset ΔF on HSPA+ system with perfect timing synchronization as:

1. The amplitude of the desired symbol is attenuated by a factor of $\frac{\sin(\pi\Delta F W_P)}{W_P \sin(\pi\Delta F)}$.
2. The phase of the desired symbol is affected by $2\pi\Delta F(W_P - 1) + 2\pi\Delta F W_P i$.
3. The frequency offset corrupts the orthogonality among the OVFS codes and causes the distortion due to interference with other HS-PDSCHs. This term is also known as Inter-Channel Interference.

Obviously, the frequency offset degrades the *Signal-to-Noise Ratio (SNR)* of the decision symbol at a receiver and corrupts the receiver performance. Now let us discuss the relationship of the performance loss and the frequency offset analytically.

Lemma 3.1. *Suppose $\{C_{m_k}[n]\}$ is the set of the OVFS codes with $SF = W$ and $k, n \in [0 \dots W - 1]$.*

Then the following equality holds

$$\forall p, q \in [0 \dots W - 1], \quad \sum_{k=0}^{W-1} C_{m_k}[p] C_{m_k}[q] = W\delta_{p,q}, \quad (3.16)$$

Proof. The set $\{C_{m_k}[n]\}$ can be expressed as a matrix B^N with dimension $W \times W$, where $N = \log_2 W$ and $B_{k,n}^N = C_{m_k}[n]$. According to the definition of the codes in [3GPP, 2008c], we can obtain

$$B^N = \begin{pmatrix} B^{N-1} & B^{N-1} \\ B^{N-1} & -B^{N-1} \end{pmatrix} \quad (3.17)$$

Obviously, B^N is a symmetric matrix and we have

$$C_{m_k}[n] = C_{m_n}[k] \quad (3.18)$$

Therefore,

$$\forall p, q \in [0 \dots W - 1], \quad \sum_{k=0}^{W-1} C_{m_k}[p] C_{m_k}[q] = \sum_{k=0}^{W-1} C_{m_p}[k] C_{m_q}[k] \quad (3.19)$$

According to the orthogonal property of OVFS codes and substituting Equation 3.11 to Equation 3.19, we get

$$\forall p, q \in [0 \dots W - 1], \quad \sum_{k=0}^{W-1} C_{m_k}[p] C_{m_k}[q] = W\delta_{p,q} \quad (3.20)$$

□

Corollary 3.2. Suppose d_k are i.i.d. random variables with zero mean and variance $E\{|d_k|^2\} = \sigma_d^2$. Define

$$I_{p,k} = \frac{1}{W} \sum_{n=0}^{W-1} d_k e^{j2\pi\Delta F n} C_{m_k}[n] C_{m_p}[n] \quad (3.21)$$

Then, the following equality holds

$$E \left\{ \left| \sum_{k=0}^{W-1} I_{p,k} \right|^2 \right\} = E \left\{ \sum_{k=0}^{W-1} |I_{p,k}|^2 \right\} = \sigma_d^2 \quad (3.22)$$

for each HS-PDSCH p .

Proof. Because d_k are i.i.d., it is quite straightforward that

$$E \left\{ \left| \sum_{k=0}^{W-1} I_{p,k} \right|^2 \right\} = E \left\{ \sum_{k=0}^{W-1} |I_{p,k}|^2 \right\} \quad (3.23)$$

The RHS of Equation 3.23 can be transformed into

$$\begin{aligned}
E \left\{ \sum_{k=0}^{W-1} |I_{p,k}|^2 \right\} &= \sum_{k=0}^{W-1} E \{ |I_{p,k}|^2 \} = \sum_{k=0}^{W-1} E \{ I_{p,k} I_{p,k}^* \} \\
&= \sigma_d^2 \left[\frac{1}{W^2} \sum_{u=0}^{W-1} \sum_{v=0}^{W-1} E \{ e^{j2\pi\Delta F(u-v)} \} \sum_{k=0}^{W-1} C_{mk}[u] C_{mp}[u] C_{mk}[v] C_{mp}[v] \right] \\
&= \sigma_d^2 \left[\frac{1}{W^2} \sum_{u=0}^{W-1} \sum_{v=0}^{W-1} E \{ e^{j2\pi\Delta F(u-v)} \} C_{mp}[u] C_{mp}[v] \sum_{k=0}^{W-1} C_{mk}[u] C_{mk}[v] \right]
\end{aligned} \tag{3.24}$$

According to Lemma 3.1 and using in Equation 3.24 the identity

$$\sum_{k=0}^{W-1} C_{mk}[u] C_{mk}[v] = W\delta[u-v]$$

yields

$$E \left\{ \sum_{k=0}^{W-1} |I_{p,k}|^2 \right\} = \sigma_d^2 \tag{3.25}$$

□

Because all HS-PDSCHs use the same spreading factor W , to make full use of HS-PDSCHs, we take $K = W$ in Equation 3.15 and approximate the interference power for a dedicated channel P caused by the frequency offset as

$$\begin{aligned}
\sigma_{ICI}^2 &= E \{ |ICI_P|^2 \} = E \left\{ \left| \alpha_E e^{j\phi} \sum_{\substack{k \neq P \\ k=0}}^{W-1} I_{P,k} \right|^2 \right\} \\
&= \alpha_E^2 E \left\{ \left| \sum_{k=0}^{W-1} I_{P,k} \right|^2 \right\} - \alpha_E^2 E \{ |I_{P,P}|^2 \} \\
&= \alpha_E^2 \sigma_d^2 \left[1 - \frac{\sin^2(\pi\Delta FW)}{W^2 \sin^2(\pi\Delta F)} \right] \\
&= \mathcal{E}_h \sigma_d^2 (1 - \beta^2)
\end{aligned} \tag{3.26}$$

where $\mathcal{E}_h = \alpha_E^2$ is defined as the power factor of the effective channel. $\beta = \frac{\sin(\pi\Delta FW)}{W \sin(\pi\Delta F)}$ denotes the amplitude attenuation factor caused by the frequency offset.

3.3.1 Degradation of Signal-to-Noise Ratio

It is well known that SNR plays an important role in analyzing the performance of communication systems. As above discussed, the frequency offset causes a noise-like interference, which will degrade the SNR of the received signal at the input of the decision function in the system.

If the signal-to-noise ratio of the fully synchronized system is SNR_{syn} and that of the system with frequency offset is SNR_{wf} , the degradation of SNR in dB is defined as [Pollet et al., 1995]

$$D = -10 \log \left(\frac{\text{SNR}_{\text{wf}}}{\text{SNR}_{\text{syn}}} \right) \quad (3.27)$$

From Equation 3.12 we can easily get

$$\text{SNR}_{\text{syn}} = \frac{\mathcal{E}_h \sigma_d^2}{\sigma_{\eta_E}^2} \quad (3.28)$$

From Equation 3.14 and Equation 3.26, the signal-to-noise ratio, or more precisely the *Signal-to-Interference-plus-Noise Ratio* (SINR), can be derived as

$$\begin{aligned} \text{SNR}_{\text{wf}} &= \frac{\beta^2 \mathcal{E}_h \sigma_d^2}{\sigma_{ICI}^2 + \sigma_{\eta_E}^2} \\ &= \frac{\beta^2 \mathcal{E}_h \sigma_d^2}{\mathcal{E}_h \sigma_d^2 (1 - \beta^2) + \sigma_{\eta_E}^2} \end{aligned} \quad (3.29)$$

Substituting Equation 3.28 and 3.29 to Equation 3.27, the degradation is obtained as

$$\begin{aligned} D &= 10 \log \left(1 + \frac{\mathcal{E}_h \sigma_d^2}{\sigma_{\eta_E}^2} (1 - \beta^2) \right) - 10 \log(\beta^2) \\ &= 10 \log \left(\frac{1}{\beta^2} - \left(1 - \frac{1}{\beta^2} \right) \text{SNR}_{\text{syn}} \right) \end{aligned} \quad (3.30)$$

If we assume that the order of QAM signal is M and define the complex noise power $\sigma_{\eta_E}^2 = N_0$, the average bit energy $E_b = \frac{\sigma_d^2}{\log_2 M}$ and Equation 3.30 can be rewritten as

$$D(\gamma_b, \beta, M) = 10 \log \left(\frac{1}{\beta^2} - \log_2 M \left(1 - \frac{1}{\beta^2} \right) \gamma_b \right) \quad (3.31)$$

where $\gamma_b = \frac{\mathcal{E}_h E_b}{N_0}$ denotes the received SNR per bit under the fading channel.

Taking the parameters of HSPA+ system into account, such as $f_{\text{chip}} = 3.84\text{MHz}$, $W = 16$ and $M = 64$, the curves shown in Figure 3.2 illustrate the SNR degradation of 64-QAM signal in HSPA+ system with different frequency offsets. It is obvious that the SNR degradation caused by the frequency offset is negligible in the receive SNR range below 35 dB, when the frequency offset is lower than 200 Hz. If we set the target that the SNR degradation caused by the frequency offset be less than 0.1 dB when $\bar{\gamma}_b = 25$ dB, we obtain the corresponding frequency offset $\Delta f \approx 328$ Hz. As a rule of thumb, the carrier frequency of HSPA+ system is around 2 GHz. Then, 328 Hz equals to 0.164 ppm of the carrier frequency, or the *Doppler Shift* caused by the speed difference of 177 km/h between the transmitter and the receiver.

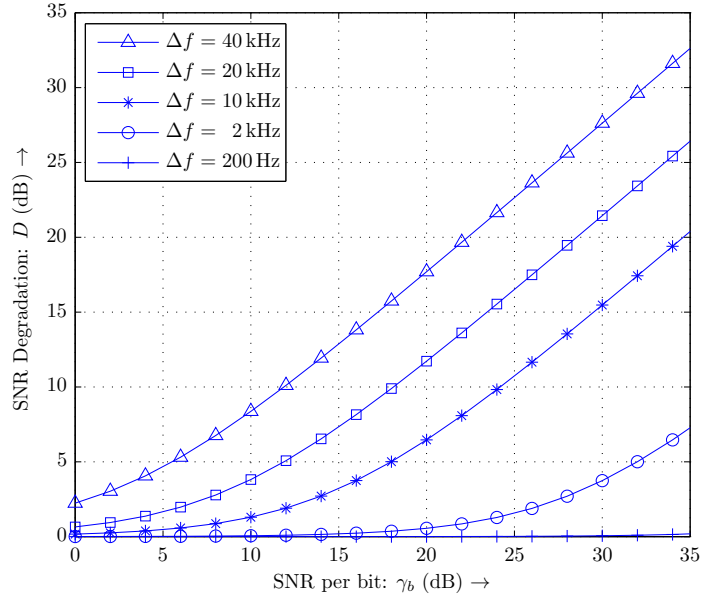


Figure 3.4: SNR Degradation of 64-QAM Signal in HSPA+ System with Frequency Offset

3.3.2 Performance Loss Analysis

In modern high speed digital communication systems *Symbol Error Rate (SER)* and *Bit Error Rate (BER)* are commonly adopted to illustrate the performance of the physical layer of the system. Next we analyze the performance loss caused by frequency offset in the system with an ideal channel estimation and an imperfect channel estimation respectively.

3.3.2.1 Case I: Ideal Channel Estimation

Under the assumption of perfect synchronization, according to the result in Appendix A, the SER of M -ary QAM signal under AWGN channel can be expressed as

$$P_M = 4 \left(1 - \frac{1}{\sqrt{M}} \right) Q \left(\sqrt{\frac{3 \log_2 M E_b}{M-1 N_0}} \right) \times \left[1 - \left(1 - \frac{1}{\sqrt{M}} \right) Q \left(\sqrt{\frac{3 \log_2 M E_b}{M-1 N_0}} \right) \right] \quad (3.32)$$

where $Q(x)$ is the Q -function defined as

$$Q(x) = \frac{1}{\sqrt{2\pi}} \int_x^{+\infty} e^{-\frac{t^2}{2}} dt, \quad x \geq 0$$

Given a channel with a fixed attenuation α , Equation 3.32 can be represented as

$$P_M(\gamma_b) = 4 \left(1 - \frac{1}{\sqrt{M}} \right) Q \left(\sqrt{\frac{3 \log_2 M}{M-1} \gamma_b} \right) \times \left[1 - \left(1 - \frac{1}{\sqrt{M}} \right) Q \left(\sqrt{\frac{3 \log_2 M}{M-1} \gamma_b} \right) \right] \quad (3.33)$$

where $\gamma_b = \alpha^2 \frac{E_b}{N_0}$ denotes the receive SNR per bit.

When α is random, γ_b is also random and represents the instantaneous receive SNR. We average $P_M(\gamma_b)$ over the PDF of γ_b to obtain the SER as

$$P_M^{(\text{fad})} = \int_0^{+\infty} P_M(\gamma_b) p(\gamma_b) d\gamma_b \quad (3.34)$$

where $p(\gamma_b)$ is the PDF of γ_b when α is random. In the case of frequency non-selective Rayleigh fading channel, given $\alpha \sim \text{Rayleigh}(\frac{\sigma_h}{\sqrt{2}})$, γ_b has a *gamma distribution* with parameter $k = 1$ and $\theta = \frac{\sigma_h^2 E_b}{N_0}$, or equivalently an *exponential distribution* with parameter $\lambda = \frac{N_0}{\sigma_h^2 E_b}$. It yields the mean value $\bar{\gamma}_b = k\theta = \frac{\sigma_h^2 E_b}{N_0}$ and the *conditional* PDF of γ_b with respect to $\bar{\gamma}_b$ can be represented as [Alouini and Goldsmith, 1999]

$$p(\gamma_b; \bar{\gamma}_b) = \begin{cases} \frac{1}{\bar{\gamma}_b} e^{-\frac{\gamma_b}{\bar{\gamma}_b}}, & \gamma_b \geq 0 \\ 0, & \text{otherwise} \end{cases} \quad (3.35)$$

Substituting Equation 3.33 and 3.35 into Equation 3.34, the SER of M -ary QAM signal over the flat Rayleigh fading channel can be expressed as [Kim et al., 1996]

$$P_M^{(\text{fad})}(\bar{\gamma}_b) = \frac{\sqrt{M}-1}{M} \left[(\sqrt{M}-1) + 4I_1 - (\sqrt{M}-1) I_2 \right] \quad (3.36)$$

where

$$\begin{aligned} I_1 &= \frac{1}{2} - \frac{1}{2}\xi \\ I_2 &= \frac{4}{\pi} \xi \tan^{-1} \xi \end{aligned}$$

and

$$\xi = \sqrt{\frac{\bar{\gamma}_b G}{1 + \bar{\gamma}_b G}}, \quad G = \frac{3 \log_2 M}{2(M-1)}$$

The above result is obtained in the case of perfect synchronization and perfect channel state knowledge. However, as discussed above, the frequency offset, no matter caused by the carrier oscillator offset between transmitter and receiver, or by the *Phase Noise* of the oscillator in transmitter and receiver, even by the *Doppler Shift*, will degrade the SNR of the decision symbols and corrupt the receiver performance.

In the system with frequency offset, λ_b is used to denote the effective SNR of the decision symbol. According to Equation 3.31, we obtain

$$\lambda_b = \frac{\beta^2 \gamma_b}{1 + \mu(\beta) \gamma_b} \quad \text{or} \quad \gamma_b = \frac{\lambda_b}{\beta^2 - \mu(\beta) \lambda_b} \quad (3.37)$$

where $\mu(\beta) = \log_2 M(1 - \beta^2)$.

From Equation 3.37 we can find out that the effective SNR λ_b will be limited by the frequency offset even when γ_b goes to infinity:

$$\lim_{\gamma_b \rightarrow +\infty} \lambda_b = \frac{\beta^2}{\mu(\beta)} \quad (3.38)$$

The derivative of γ_b with respect to λ_b is deduced from Equation 3.37

$$\frac{d\gamma_b}{d\lambda_b} = \frac{\beta^2}{[\beta^2 - \mu(\beta)\lambda_b]^2} \geq 0 \quad (3.39)$$

Therefore, the conditional PDF of λ_b with respect to $\bar{\gamma}_b$ and β is obtained as [Proakis, 2000]

$$p(\lambda_b | \bar{\gamma}_b, \beta) = \frac{d\gamma_b}{d\lambda_b} p(\gamma_b | \bar{\gamma}_b, \beta) = \frac{d\gamma_b}{d\lambda_b} p(\gamma_b = g(\lambda_b) | \bar{\gamma}_b) \quad (3.40)$$

Combining Equation 3.37, 3.38, 3.39 and 3.40, the conditional PDF of λ_b can be expressed as

$$p(\lambda_b | \bar{\gamma}_b, \beta) = \begin{cases} \frac{\beta^2}{\bar{\gamma}_b [\beta^2 - \mu(\beta)\lambda_b]^2} \exp\left(-\frac{\lambda_b}{\bar{\gamma}_b [\beta^2 - \mu(\beta)\lambda_b]}\right) & , 0 \leq \lambda_b \leq \frac{\beta^2}{\mu(\beta)} \\ 0 & , \text{otherwise} \end{cases} \quad (3.41)$$

Averaging the instantaneous SER $P_M(\lambda_b)$ over the PDF of λ_b yields the SER of M -ary QAM signal in HSPA+ system over flat Rayleigh fading channel with frequency offset impairment

$$\begin{aligned} P_M^{(\text{fad})}(\bar{\gamma}_b, \beta) &= \int_{\lambda_b} P_M(\lambda_b) p(\lambda_b | \bar{\gamma}_b, \beta) d\lambda_b \\ &= \int_0^{\frac{\beta^2}{\mu(\beta)}} 4 \left(1 - \frac{1}{\sqrt{M}}\right) Q\left(\sqrt{\frac{3 \log_2 M}{M-1}} \lambda_b\right) \\ &\quad \cdot \left[1 - \left(1 - \frac{1}{\sqrt{M}}\right) Q\left(\sqrt{\frac{3 \log_2 M}{M-1}} \lambda_b\right)\right] \\ &\quad \cdot \frac{\beta^2}{\bar{\gamma}_b [\beta^2 - \mu(\beta)\lambda_b]^2} \exp\left(-\frac{\lambda_b}{\bar{\gamma}_b [\beta^2 - \mu(\beta)\lambda_b]}\right) d\lambda_b \end{aligned} \quad (3.42)$$

The close form result of the integral in Equation 3.42 does not exist. Hence, we resort to the numerical method to get the solution. Figure 3.5 shows the SER curves of 64-QAM signal in HSPA+ system with different frequency offsets over an AWGN channel and a flat Rayleigh fading channel respectively. We can find out that the performance loss of the system with frequency offset smaller than 200 Hz is negligible in the both cases. When the frequency offset is increased greater than 2 kHz, the performance loss in the case of the AWGN channel is quite remarkable, but that in the case of the flat Rayleigh fading channel is still negligible. It implies that the performance loss caused by the frequency offset is greater, when the *Line Of Sight (LOS)* part of the channel effect is stronger. From

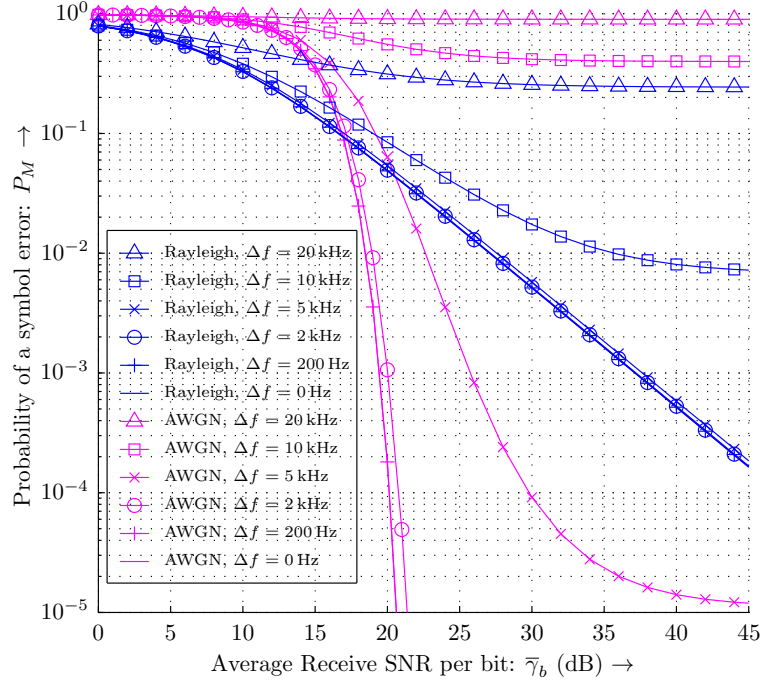


Figure 3.5: Symbol Error Rate of 64-QAM signal in HSPA+ System with Frequency Offset over an AWGN Channel and a Rayleigh Channel

point of view of LOS part of a channel response, the flat Rayleigh fading channel reflects the channel without LOS part. On the contrary, the AWGN channel can be seen as the channel with only LOS part. The result from above analysis suggests that the frequency offset of the decision symbol should be kept below 200 Hz to ensure the system performance under any channel.

3.3.2.2 Case II: Imperfect Channel Estimation

Above mentioned results are obtained under the assumption of perfect channel estimation. However, in the real system perfect channel estimation does not exist, furthermore, the ICI caused by the frequency offset will increase the channel estimation error, when the frequency offset is not perfectly compensated.

A. Data-aided Channel Estimation

HSPA+ system provides pilot signals to help the receiver to estimate and to track the fading effect of the channel.

Recall Equation 3.14 here

$$\tilde{d}_P[i] = \alpha_E e^{j\phi} \frac{\sin(\pi\Delta F W_P)}{W_P \sin(\pi\Delta F)} e^{j2\pi\Delta F(W_P-1)} e^{j2\pi W_P \Delta F i} d_P[i] + ICI_P[i] + \eta_E[i]$$

The receive symbols after descrambling and despreading process consist of the part from the de-

sired data symbol, ICI caused by the frequency offset and the additive Gaussian noise. If $d_P[i]$ is the pilot symbol, the receiver has prior knowledge of the pilot symbol and *Zero Forcing (ZF)* estimator can be employed to estimate the channel factor as

$$\tilde{h}[i] = \frac{\tilde{d}_P[i]}{d_P[i]} = h[i] + \frac{ICI[i] + \eta_E[i]}{d_P[i]} = h[i] + \frac{v[i]}{d_P[i]} \quad (3.43)$$

where $h[i] = \alpha_E e^{j\phi} \frac{\sin(\pi\Delta F W_P)}{W_P \sin(\pi\Delta F)} e^{j[2\pi\Delta F(W_P-1)+2\pi W_P\Delta F i]}$ is the effective channel fading effect when the frequency offset is not zero, and $v[i] = ICI[i] + \eta_E[i]$ denotes the interference plus noise in the pilot channel. The amplitude of $h[i]$ is $z_h[i] = \alpha_E \frac{\sin(\pi\Delta F W_P)}{W_P \sin(\pi\Delta F)}$ and the phase of $h[i]$ is $\phi_h[i] = \phi + 2\pi\Delta F(W_P - 1) + 2\pi W_P\Delta F i$.

Under the assumption of a flat Rayleigh fading channel, the fading amplitude of the channel $z_h = |h|$ follows the probability density function

$$p(z_h) = \frac{2z_h}{\Omega} \exp\left(-\frac{z_h^2}{\Omega}\right) \quad (3.44)$$

Meanwhile, z_h and its estimate $\hat{z}_h = |\tilde{h}|$ have a bivariate Rayleigh distribution given by [*Simon and Alouini, 1998*]

$$p(z_h, \hat{z}_h) = \frac{4z_h \hat{z}_h}{1-\rho} I_0\left(\frac{2\sqrt{\rho}z_h \hat{z}_h}{(1-\rho)\Omega\hat{\Omega}}\right) \exp\left[-\frac{1}{1-\rho}\left(\frac{z_h^2}{\Omega} + \frac{\hat{z}_h^2}{\hat{\Omega}}\right)\right] \quad (3.45)$$

where $\rho = \frac{\text{cov}(z_h^2, \hat{z}_h^2)}{\sqrt{\text{var}(z_h^2)\text{var}(\hat{z}_h^2)}}$ is the correlation coefficient between z_h^2 and \hat{z}_h^2 , $\Omega = E\{z_h^2\}$, $\hat{\Omega} = E\{\hat{z}_h^2\}$,

and $I_0(\cdot)$ is the zeroth-order modified Bessel function. The phase ϕ_h and its estimate $\hat{\phi}_h$ have a joint distribution given by [*Davenport and Root, 1958*]

$$p(\phi_h, \hat{\phi}_h) = \frac{1-\rho}{4\pi^2} \left[\frac{(1-q^2)^{\frac{1}{2}} + q(\pi - \cos^{-1} q)}{(1-q^2)^{\frac{3}{2}}} \right], \quad 0 \leq \phi_h, \hat{\phi}_h \leq 2\pi \quad (3.46)$$

where $q = \sqrt{\rho} \cos(\phi_h - \hat{\phi}_h)$. Note that the indices i in the equations are dropped for simplicity of notation.

B. Amplitude Estimation Error

Firstly, we take only the amplitude estimation error into account and assume perfect phase estimation, i.e. $\hat{\phi}_h = \phi_h$. Given the fading amplitude estimate \hat{z}_h , the decision symbol after channel equalization is then

$$\begin{aligned} \hat{d}_P &= \frac{e^{-j\hat{\phi}_h} \tilde{d}_P}{\hat{z}_h} \\ &= \frac{z_h}{\hat{z}_h} d_P + \frac{v}{\hat{z}_h} \end{aligned} \quad (3.47)$$

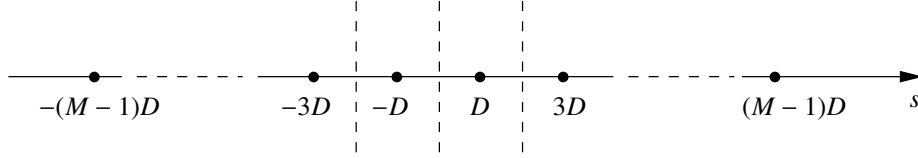


Figure 3.6: Signal points for M -ary PAM signals.

where $\nu = ICI_P + \eta_E$ is the combination of the interference and the additive Gaussian noise.

If the transmit symbol d_p is from M -ary rectangular QAM signal constellation and $M = 2^k$ where k is even, the probability of error for QAM is easily determined from the probability of error for PAM with \sqrt{M} signal points. Specially, the SER of M -ary QAM system is [Proakis, 2000]

$$P_M = 1 - \left(1 - P_{\sqrt{M}}\right)^2 \quad (3.48)$$

where $P_{\sqrt{M}}$ is the SER of an \sqrt{M} -ary PAM with one-half the average power in each quadrature signal of the equivalent QAM system. Therefore, we first study the SER of M -ary PAM signal when the system is affected by the frequency offset and the amplitude estimation error of the channel.

The signal constellation of M -ary PAM signals is shown in Figure 3.6. They are represented geometrically as M one-dimensional signal points with the amplitudes A_m as [Proakis, 2000]

$$A_m = (2m - 1 - M)D, \quad m = 1, 2, \dots, M \quad (3.49)$$

where D is a positive constant. The minimum Euclidean distance of the M signal points is $d_{min}^{(e)} = 2D$. The decision region of the symbol s_m is $|s - A_m| < \frac{1}{2}d_{min}^{(e)} = D$. Taking the difference of the two outside signals into account, assuming equally probable signals for the transmitted data symbol $d_p[i]$, the probability of error for M -ary PAM according conditioned on $z_h[i]$ and $\hat{z}_h[i]$ can be represented as

$$\begin{aligned} P_M(E | z_h[i], \hat{z}_h[i]) &= \frac{1}{M} \sum_{m=2}^{M-1} P\left(|\hat{d}_p[i] - A_m| > D | z_h[i], \hat{z}_h[i]\right) \\ &+ \frac{1}{M} P\left(\hat{d}_p[i] - A_1 > D | z_h[i], \hat{z}_h[i]\right) \\ &+ \frac{1}{M} P\left(\hat{d}_p[i] - A_M < -D | z_h[i], \hat{z}_h[i]\right) \end{aligned} \quad (3.50)$$

Using the result in Appendix B, we obtain

$$P_M(E | z_h, \hat{z}_h) = \frac{2}{M} \sum_{m=1}^{M-1} Q\left(\frac{[(2m - M)\hat{z}_h - (2m - 1 - M)z_h] \frac{\sqrt{2}D}{N_1}}{1}\right) \quad (3.51)$$

The SER of M -ary PAM is obtained by averaging the conditional SER over the joint distribution given in Equation 3.45

$$P_M(E) = \int_0^{+\infty} \int_0^{+\infty} P_M(E | z_h, \hat{z}_h) p(z_h, \hat{z}_h) dz_h d\hat{z}_h \quad (3.52)$$

Note that the conditional probability in Equation 3.51 is a weighted sum of $Q\left(\left[(a_m z_h + b_m \hat{z}_h)\right] \frac{\sqrt{2D}}{N_1}\right)$, with $a_m = M + 1 - 2m$ and $b_m = 2m - M$. Define integral $\mathcal{I}(a_m, b_m, \Omega, \hat{\Omega}, \rho)$ as

$$\mathcal{I}(a_m, b_m, \Omega, \hat{\Omega}, \rho) = \int_0^{+\infty} \int_0^{+\infty} Q\left(\left[(a_m z_h + b_m \hat{z}_h)\right] \frac{\sqrt{2D}}{N_1}\right) p(z_h, \hat{z}_h) dz_h d\hat{z}_h \quad (3.53)$$

and then Equation 3.52 can be expressed as

$$P_M(E) = \frac{2}{M} \sum_{m=1}^{M-1} \mathcal{I}(a_m, b_m, \Omega, \hat{\Omega}, \rho) \quad (3.54)$$

According to Equation 35 in [Tang et al., 1999], the integral in Equation 3.53 can also be represented as

$$\begin{aligned} \mathcal{I}(a_m, b_m, \Omega, \hat{\Omega}, \rho) &= \mathcal{I}(a_m, b_m, \bar{\lambda}_b, r, \rho) \\ &= \frac{1-\rho}{\pi} \int_0^{\frac{\pi}{2}} \int_{-\frac{\pi}{2}}^{\frac{\pi}{2}} \frac{\sin 2\theta \mathcal{J}_2\left(\sqrt{\rho} \sin 2\theta \sin \varphi + 1, \sqrt{(1-\rho)g_M \bar{\lambda}_b} (a_m \cos \theta + \sqrt{r} b_m \sin \theta)\right)}{\left(\sqrt{\rho} \sin 2\theta \sin \varphi + 1\right)^2} d\varphi d\theta \end{aligned} \quad (3.55)$$

where $g_M = \frac{6 \log_2 M}{M^2 - 1}$, $\bar{\lambda}_b$ is the average SINR per bit of the decision symbol, $r = \frac{\hat{\Omega}}{\Omega}$. The function $\mathcal{J}_2(c, d)$ is defined as

$$\mathcal{J}_2(c, d) = c^2 \int_0^{+\infty} e^{-ct} t Q(d\sqrt{t}) dt \quad (3.56)$$

and using integration by parts, it can be shown that

$$\mathcal{J}_2(c, d) = \frac{1}{2} - \frac{3}{4} \frac{d}{\sqrt{2c + d^2}} + \frac{1}{4} \left(\frac{d}{\sqrt{2c + d^2}} \right)^3 \quad (3.57)$$

Then, Equation 3.54 can also be represented as

$$P_M(E) = \frac{2}{M} \sum_{m=1}^{M-1} \mathcal{I}(a_m, b_m, \bar{\lambda}_b, r, \rho) \quad (3.58)$$

Assuming that the average power of the pilot symbols equals the average power of data symbols, using the result in Appendix C, we have $r = 1 + \frac{1}{\log_2 M \bar{\lambda}_b}$ and $\rho = \frac{\log_2 M \bar{\lambda}_b}{1 + \log_2 M \bar{\lambda}_b}$. Therefore, the SER of M -ary PAM signals can be written as

$$P_M(\bar{\lambda}_b) = \frac{2}{M} \sum_{m=1}^{M-1} \mathcal{I}(a_m, b_m, \bar{\lambda}_b) \quad (3.59)$$

where $a_m = M + 1 - 2m$ and $b_m = 2m - M$.

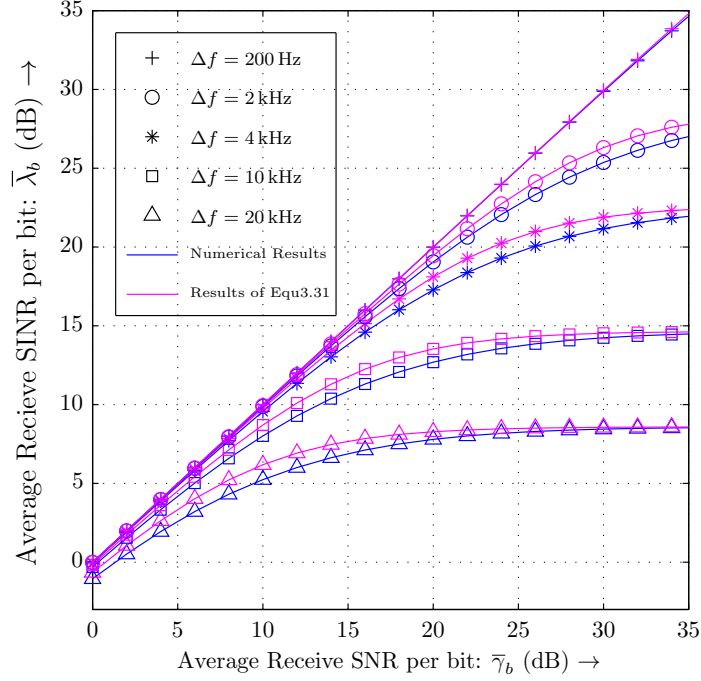


Figure 3.7: Average Receive SINR vs. Average Receive SNR of HSPA+ system with 64-QAM signal under different frequency offsets over a flat Rayleigh fading channel

According to Equation 3.41 we have the average SINR per bit as

$$\begin{aligned}\bar{\lambda}_b(\bar{\gamma}_b, \beta) &= \int_0^{\frac{\beta^2}{\mu(\beta)}} \lambda_b p(\lambda_b; \bar{\gamma}_b, \beta) d\lambda_b \\ &= \int_0^{\frac{\beta^2}{\mu(\beta)}} \frac{\beta^2 \lambda_b}{\bar{\gamma}_b [\beta^2 - \mu(\beta) \lambda_b]^2} \exp\left(-\frac{\lambda_b}{\bar{\gamma}_b [\beta^2 - \mu(\beta) \lambda_b]}\right) d\lambda_b\end{aligned}\quad (3.60)$$

In the previous section we have derived the degradation of SNR caused by frequency offset by treating the channel with a constant fading and obtained Equation 3.31. We can also approximate the result of the integral in Equation 3.60 as

$$\bar{\lambda}_b(\bar{\gamma}_b, \beta) [\text{dB}] = \bar{\gamma}_b [\text{dB}] - D(\bar{\gamma}_b, \beta) \quad (3.61)$$

Figure 3.7 shows us the results from the two different methods to obtain $\bar{\lambda}_b(\bar{\gamma}_b, \beta)$. The difference of the results from the two methods is shown to be less than 1 dB.

Substituting the obtained $\bar{\lambda}_b$ to Equation 3.59, yields the SER of M -ary PAM system $P_M^{(\text{PAM})}$, and

then recall Equation 3.48 to obtain the SER of M -ary QAM system as

$$P_M^{(\text{QAM})} = 1 - \left[1 - P_{\sqrt{M}}^{(\text{PAM})} \right]^2 \quad (3.62)$$

Thus, for a given receive SNR and frequency offset, the procedure to calculate the symbol error rate of an HSPA+ system with 64-QAM signal over a flat Rayleigh fading channel and impacted by the fading amplitude estimation error is summarized as follows:

STEP 1: Calculate $\bar{\gamma}_b = \frac{\text{SNR}}{\log_2 M}$ and $\beta = \frac{\sin(\pi \Delta F W)}{W \sin(\pi \Delta F)}$ for a given receive SNR and frequency offset ΔF , where $M = 64$ and $W = 16$.

STEP 2: Substitute the results from previous step into Equation 3.60 and calculate $\bar{\lambda}_b$ by executing numerical integration, or adopt Equation 3.61 to get an approximation of $\bar{\lambda}_b$.

STEP 3: Substitute the result from previous step into Equation 3.59 and execute numerical integration to calculate $P_8^{(\text{PAM})} = \frac{1}{4} \sum_{m=1}^7 \mathcal{I}(a_m, b_m, \bar{\lambda}_b)$ according to Equation 3.55, 3.57 and Table 3.1.

STEP 4: Calculate $P_{64}^{(\text{QAM})} = 1 - \left[1 - P_8^{(\text{PAM})} \right]^2$ by following Equation 3.62.

Table 3.1: a_m, b_m of 64-QAM

m	a_m	b_m
1	7	-6
2	5	-4
3	3	-2
4	1	0
5	-1	2
6	-3	4
7	-5	6

C. Amplitude and Phase Estimation Error

When the phase estimation is not perfect, the inphase and quadrature components of QAM signals interfere with each other. If we define the phase estimation error $\psi = \phi_h - \hat{\phi}_h$, Equation 3.47 can be rewritten as

$$\begin{aligned} \hat{d}_P &= \frac{z_h}{\hat{z}_h} e^{j(\phi_h - \hat{\phi}_h)} d_P + \frac{v}{\hat{z}_h} e^{-j\hat{\phi}_h} = \frac{z_h}{\hat{z}_h} e^{j\psi} d_P + \frac{\varpi}{\hat{z}_h} \\ &= \frac{z_h}{\hat{z}_h} (S_I \cos \psi - S_Q \sin \psi) + j \frac{z_h}{\hat{z}_h} (S_Q \cos \psi + S_I \sin \psi) + \frac{\varpi}{\hat{z}_h} \end{aligned} \quad (3.63)$$

where S_I and S_Q are the inphase part and the quadrature part of the data symbol d_P , $\varpi = v e^{-j\hat{\phi}_h}$ is

the effective noise. For simplicity of analysis, we still assume the effective noise ϖ is a zero-mean circular symmetric complex Gaussian process. Because multiplying a complex random variable with $e^{-j\hat{\phi}_h}$ does not change its variance, we have $\sigma_{\varpi}^2 = \sigma_v^2 = N_1$.

As above mentioned, the SER of a two dimensional QAM signal can be expressed by the SER of a one dimension PAM signal. Taking the inphase part from Equation 3.64, we have

$$\Re\{\hat{d}_P\} = \frac{z_h}{\hat{z}_h} \cos \psi S_I - \frac{z_h}{\hat{z}_h} \sin \psi S_Q + \frac{\varpi_I}{\hat{z}_h} \quad (3.64)$$

where S_I and S_Q can be seen as a M -ary PAM signal, when d_P is a square M^2 -ary QAM signal.

The phase estimation error ψ is seen as a random variable and its probability density function can be derived from Equation 3.46 as [Tang et al., 1999]

$$p(\psi) = \frac{1-\rho}{4\pi^2} \left[\frac{(1-q^2)^{\frac{1}{2}} + q(\pi - \cos^{-1} q)}{(1-q^2)^{\frac{3}{2}}} \right] (2\pi - |\psi|), \quad -2\pi \leq \psi \leq 2\pi \quad (3.65)$$

where $q = \sqrt{\rho} \cos \psi$. It is obvious that function $p(\psi)$ is even because $\cos \psi$ and $|\psi|$ are both even.

Using the result in Appendix D, the conditional SER of M -ary PAM signal is

$$P_M(E | z_h, \hat{z}_h, \psi) = \frac{2}{M^2} \sum_{m=1}^{M-1} \sum_{i=1}^M Q \left(\left[[(M+1-2m) \cos \psi + (2i-1-M) \sin \psi] z_h + (2m-M) \hat{z}_h \right] \frac{\sqrt{2D}}{N_1} \right) \quad (3.66)$$

It is proved in Appendix E that $P_M(E | z_h, \hat{z}_h, \psi)$ is even with respect to ψ .

Thus, assuming that the phase estimation error ψ is independent of z_h and \hat{z}_h , the average SER over the channel estimation error is given by

$$\begin{aligned} P_M^{(\text{PAM})}(E) &= \int_{-2\pi}^{2\pi} \int_0^{+\infty} \int_0^{+\infty} P_M(E | z_h, \hat{z}_h, \psi) p(z_h, \hat{z}_h, \psi) dz_h d\hat{z}_h d\psi \\ &= 2 \int_0^{2\pi} \int_0^{+\infty} \int_0^{+\infty} P_M(E | z_h, \hat{z}_h, \psi) p(z_h, \hat{z}_h) p(\psi) dz_h d\hat{z}_h d\psi \\ &= \frac{4}{M^2} \sum_{m=1}^{M-1} \sum_{i=1}^M \int_0^{2\pi} \left[\int_0^{+\infty} \int_0^{+\infty} Q((a_m \cos \psi + b_i \sin \psi) z_h + c_m \hat{z}_h) p(z_h, \hat{z}_h) dz_h d\hat{z}_h \right] p(\psi) d\psi \end{aligned} \quad (3.67)$$

where $a_m = M+1-2m$, $b_i = 2i-1-M$ and $c_m = 2m-M$. The probability density functions $p(z_h, \hat{z}_h)$ and $p(\psi)$ are given in Equation 3.45 and Equation 3.65 respectively.

Using the similar method adopted in Equation 3.53 and 3.55, Equation 3.67 can be represented as

$$P_M^{(\text{PAM})}(E) = \frac{4}{M^2} \sum_{m=1}^{M-1} \sum_{i=1}^M \mathcal{I}_2(a_m, b_i, c_m, \psi, \bar{\gamma}_b, \beta) \quad (3.68)$$

Table 3.2 – continued

m	i	a_m	b_i	c_m	m	i	a_m	b_i	c_m	m	i	a_m	b_i	c_m
7	4	-5	-2	6										
7	5	-5	1	6										
7	6	-5	3	6										
7	7	-5	5	6										
7	8	-5	7	6										

3.3.3 Numerical Results and Simulations

Previously we have derived the formulas to assess the SER performance of HSPA+ system with 64-QAM signal over flat Rayleigh fading channel in the case of considering frequency offset and channel estimation error. In this section we will show the numerical results. The Monte Carlo simulations are also conducted to verify the validity of these formulas. We use usually 100,000 runs of the simulations to derive the average SER under various SNR.

The SER curves of Monte Carlo simulation for the system with frequency offsets and ideal channel state information and those curves based on the results of Equation 3.42 are depicted in Figure 3.8. The SER curves of Monte Carlo simulation for the system with frequency offsets and channel amplitude estimation error and those curves based on the numerical results from above mentioned Four-Step procedure are shown in Figure 3.9. The results of considering both channel amplitude estimation error and phase estimation error are drawn in Figure 3.10. To compare the performance loss caused by the frequency offset the performance curve of the system with perfect frequency synchronization, i.e. $\Delta f = 0$ Hz, is also plotted in the figures. It is clear that simulation results closely match the analysis and the validity of our analysis is so proved.

Obviously the SER performance degrades with the increase of frequency offset. From all three figures we find that the SER curves will approach an error-rate floor when the frequency offset becomes larger. We have discussed in Equation 3.38 that the receive SINR will approach a constant asymptotically with the receive SNR approaching infinity, if the frequency offset is present. The reason is that the power of the interference caused by the frequency offset is determined by the signal power and the frequency offset and it is independent of the noise from the channel. In principle, the SER performance is in proportion to the receive SINR. Therefore, the SER curve will approach an error-rate floor with the SNR approaching infinity, if the frequency offset is present.

However, in the feasible receive SNR region of a practical system, the frequency offsets which will cause an error-rate floor are clearly not the same in different cases. Comparing Figure 3.9 and Figure 3.10 to Figure 3.8, we can easily find out that an error-rate floor can be caused by smaller frequency offset in the system with channel estimation error. The SER curves of the system without channel estimation error, as shown in Figure 3.8, illustrate that even the frequency offset reaches 4 kHz, the SER curve still does not show a clear error-rate floor until the SNR reaches 45 dB and there is only negligible performance loss compared to the perfect frequency synchronization case,

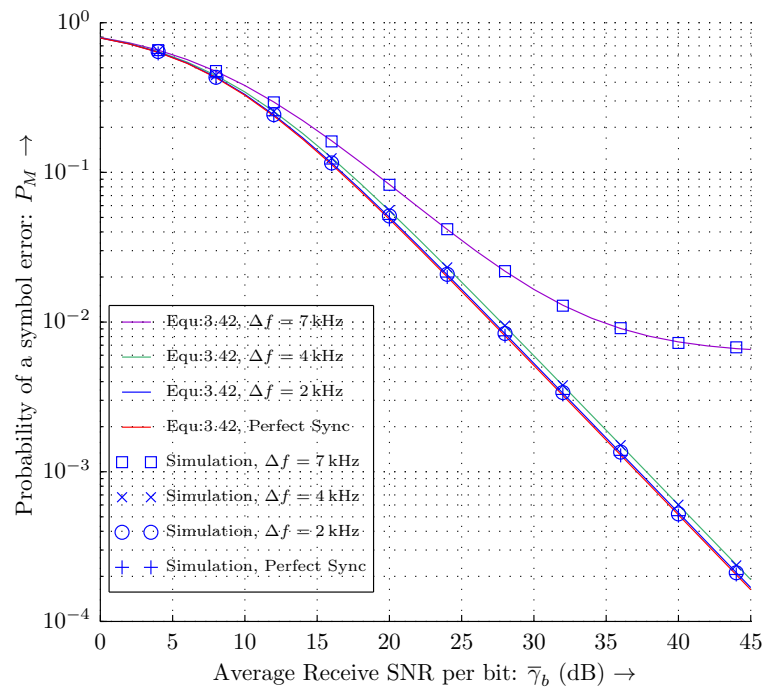


Figure 3.8: SER curves comparison: Equation 3.42 in Case I vs. Simulation

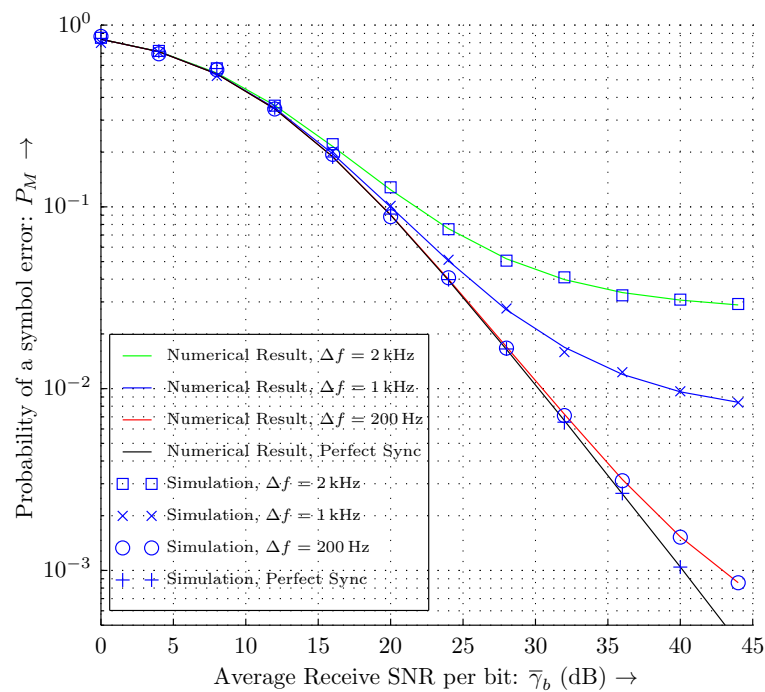


Figure 3.9: SER curves comparison: Numerical Results of Case II.B vs. Simulation

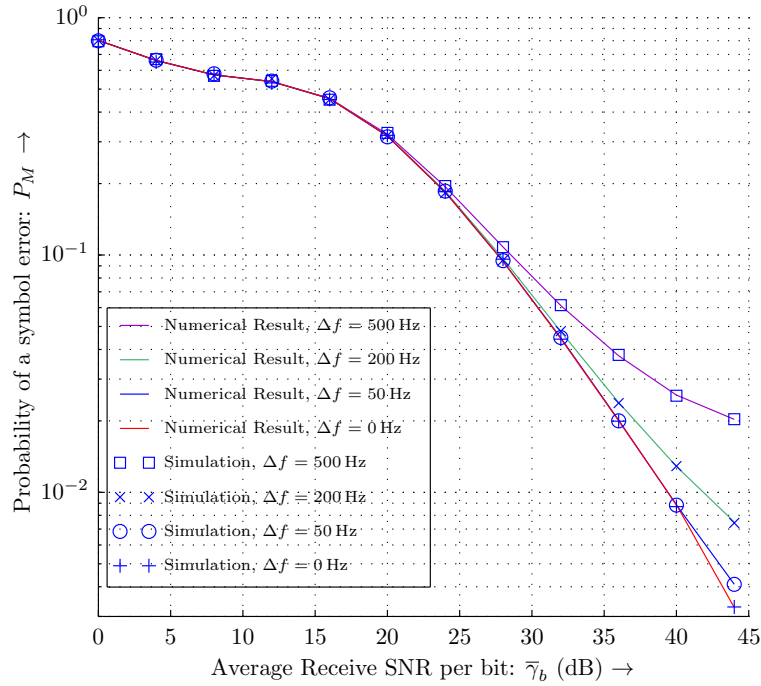


Figure 3.10: SER curves comparison: Numerical Results of Case II.C vs. Simulation

when the frequency offset equals to 2 kHz. If the system has only channel amplitude estimation error, as shown in Figure 3.9, the frequency offset of 200 Hz will cause 3 dB performance loss by $\text{SER} = 10^{-3}$. The frequency offset of 1 kHz will cause a remarkable error-rate floor and if the frequency offset reaches 2 kHz, the SER performance will never be lower than 10^{-2} . Furthermore, if both channel amplitude estimation error and phase estimation error are taken into account, the performance loss of $\Delta f = 200$ Hz reaches 2.5 dB by $\text{SER} = 10^{-2}$ and the frequency offset of 500 Hz will cause a remarkable error-rate floor when receive SNR is greater than 40 dB.

In the literatures [Tang *et al.*, 1999] and [Cao and Beaulieu, 2004], it was shown that the channel estimation error can have a serious effect on the received data error rate. That suggests us to try to develop an unbiased channel estimator with low variance to ensure the performance of the system. In estimation theory, the Cramér-Rao bound (CRB) expresses a lower bound on the variance of unbiased estimators of a deterministic parameter. From Equation 3.43 we got the observation of the channel efficient. Under the assumption that the combination of the interference and the noise has Gaussian distribution, the CRB can be derived as [Kay, 1993]

$$\text{var}(\tilde{h}) \geq \frac{\sigma_v^2}{N\mathcal{E}_{d_p}} \quad (3.70)$$

where σ_v^2 is the variance of the interference plus the noise, N depicts the number of our observations for estimating the channel and \mathcal{E}_{d_p} denotes the energy of the pilot symbols. In the normal communication systems, the energy of the pilot symbol is fixed. If the channel is assumed to have slow fading

rate and the channel fading coefficients keep unchanged during the observation. Then, the CRB is determined by the variance of the interference plus the noise.

If the frequency offset is absent, the interference is also absent and the CRB will taper off when the noise power becomes smaller and smaller. Normally, when the channel estimator is already chosen, the channel estimation error will become smaller with increasing of the receive SNR in a perfect synchronized system. Therefore, as shown in [Tang *et al.*, 1999] and [Cao and Beaulieu, 2004], under the assumption of perfect synchronization, even the channel estimation error was taken into account, the data error rate did not show a floor phenomenon.

However, that is not the case when the frequency offset is present. According to Equation 3.26, when the channel is chosen, the power of the interference caused by the frequency offset σ_{ICI}^2 is dependent on the frequency offset ΔF and the signal power σ_d^2 . Based on Equation 3.70, we know that no matter how high the receive SNR is, the CRB is limited by the interference caused by the frequency offset. That implies that the estimation error of the channel estimator is limited by the interference caused by the frequency offset. So both the SINR floor and the channel estimation error floor together cause the SER floor of the system.

3.4 Discussion

The SER performances curves of the system in different cases are gathered, grouped and drawn in Figure 3.11. Through comparison it is shown that channel estimation error has a remarkable impact on the performance of the HSPA+ system with 64-QAM signal. Meanwhile, when the frequency offset is present in the system, the channel estimation error and the received SINR will both be lower bounded by the interference caused from the frequency offset. Therefore, an error-rate floor does occur in the feasible receive SNR region and the acceptable residual frequency offset of the decision symbols is determined by the error-rate floor.

Meanwhile, the channel estimator adopted in the system is a key player, because it has great influence on the channel estimation error. As shown in Equation 3.70, the CRB will decrease if the number of the observation N becomes larger. For instance, according to the frame structure of HSPA+ system, there are 10 pilot symbols in each transmit slot. Assuming that the channel fading factor does not change during N pilot symbols, we can improve the performance of the channel estimation by simply adopting the arithmetic average of the successive N observations. The SER performance of the systems with $N = 1, 10, 20$ are shown in Figure 3.12. It is clear that the SER performance is improved with increasing N . However, the improvement will go to saturation when N grows sustainedly.

From the results shown in Figure 3.5 we can find that the performance loss caused by the frequency offset is also related to the channel. When the channel has more LOS component, the system performance loss is greater. On the contrary, when the channel has more diffusive component, the system performance loss is smaller. Therefore, the acceptable frequency offset based on the analysis of Rayleigh fading channel is essentially the upper bound of the acceptable frequency offset, because Rayleigh fading channel assumes no LOS component.

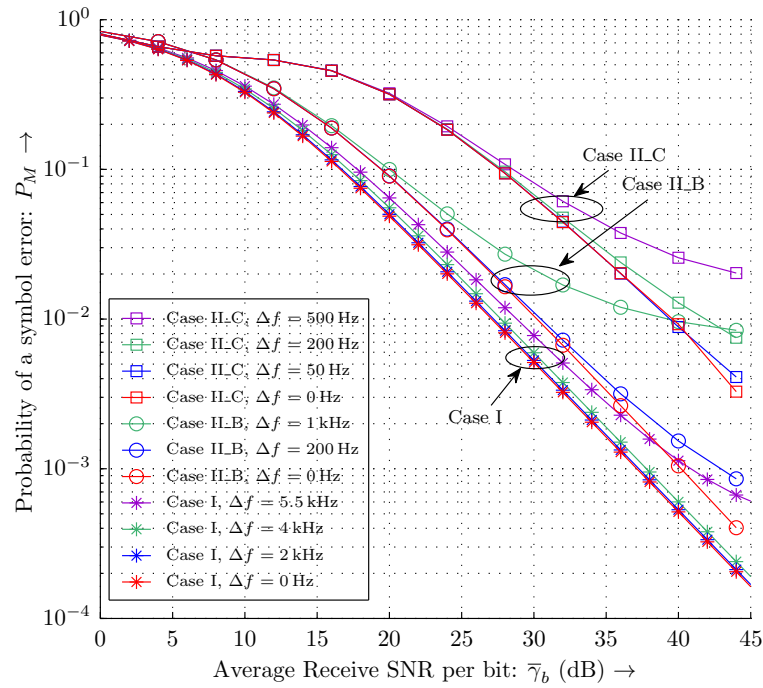


Figure 3.11: SER curves comparison: Case I, Case II_B and Case II_C

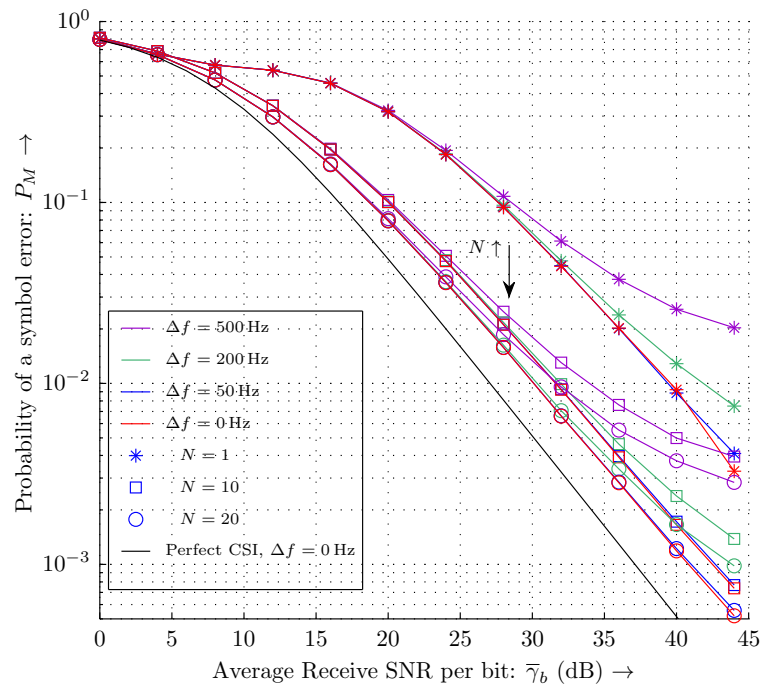


Figure 3.12: SER curves comparison: channel estimator with different average lengths

Another question is how to describe and assess the frequency offset of the system. Although we took absolute frequency offset Δf in Figure 3.8 – 3.12 to index different SER curves, the absolute frequency offset is not a good choice for assessing the synchronization performance or describing the system requirement. From above discussion we got to know that the performance loss is mainly caused by the ICI arising from the frequency offset, which degrades the receive SINR and affects the accuracy of the channel estimates. According to Equation 3.26 we can easily figure out the power of the ICI, which is determined by $\beta = \frac{\sin(\pi\Delta FW)}{W \sin(\pi\Delta F)}$, here $\Delta F = \frac{\Delta f}{f_{\text{chip}}}$. In the practical system, ΔF is normally much less than 1 and we have $\sin(\pi\Delta F) \approx \pi\Delta F$. Therefore, we can approximate β as

$$\beta \approx \frac{\sin(\pi\Delta FW)}{\pi\Delta FW} = \text{Sinc}(W\Delta F) = \text{Sinc}\left(\frac{\Delta f}{R_{\text{sym}}}\right) = \text{Sinc}(\Delta\mathcal{F}) \quad (3.71)$$

where $R_{\text{sym}} = \frac{f_{\text{chip}}}{W}$ depicts the symbol rate of each HS-PDSCH and we define $\Delta\mathcal{F} = \frac{\Delta f}{R_{\text{sym}}}$. Later we can find out that the ICI arising from the frequency offset in OFDM systems has the exact same form as here. Hence, $\Delta\mathcal{F}$ can be uniformly used to describe the frequency offset and to assess the frequency synchronization performance in both HSPA+ system and LTE system.

3.5 Summary

In this chapter, the impact of frequency offset on HSPA+ system has been discussed. The power of the ICI caused by frequency offset was derived and its impairment on the SNR was analyzed. Moreover, in order to evaluate the system error rate performance in the system without perfect frequency synchronization, an analytical method was proposed to take into account not only the interference, but also the channel estimation error, both caused by the frequency offset. The higher order modulation is introduced in HSPA+ system for achieving better spectrum efficiency and higher system throughput. However, the hardware imperfections may seriously influence its effectiveness. The proposed method helps to establish requirements for frequency synchronization.

Chapter 4

Impact of Frequency Offset on LTE System

In the walk of 21st century, diverse Internet-based applications promotes the blooming of the demands of wireless internet access systems with high capability. Starting from the end of 2004 3GPP works on the evolution of the 3G mobile system, which involves UTRA-UTRAN LTE and 3GPP *System Architecture Evolution (SAE)* [3GPP, 2006], in order to increase service provisioning, reduce user and operator cost, improve coverage and system capacity and increase data rate, reduce latency, so as to ensure the competitiveness of 3G technology during the next 10 years and beyond.

The new 3GPP UMTS LTE aims to offer 100 Mbit/s in the downlink and 50 Mbit/s in the uplink [Ekstrom et al., 2006]. By deploying a wireless system with broader bandwidth (up to 20 MHz) to provide high speed and high capability wireless access, UTRA-UTRAN LTE adopts OFDM-based technique as air interface technique. The downlink employs the *Orthogonal Frequency Division Multiple Access (OFDMA)* scheme and 64-QAM, while *SC-FDMA* scheme, also known as *Discrete Fourier Transform (DFT)*-spread OFDM, is chosen for the uplink due to its inherent low *Peak-to-Average Power Ratio (PAPR)* property, which enables a battery efficient operation of the power amplifier at the mobile terminal [Myung et al., 2006]. The primary advantage of OFDM over single-carrier schemes is its ability to cope with the frequency selective channel, which is quite normal for wideband wireless system in multipath wireless channel environment, without complex equalization filters.

The impact of frequency offset on LTE system will be discussed in this chapter.

4.1 OFDM Signal Model with Frequency Offset

The baseband signal of OFDM system with *Cyclic Prefix (CP)* can be expressed as [Speth et al., 1999]

$$s_T(t) = \frac{1}{\sqrt{T_d}} \sum_{i=-\infty}^{+\infty} \sum_{k=0}^{N-1} a_{i,k} e^{j\frac{2\pi k}{T_d}(t-T_g-iT_s)} u(t-iT_s) \quad (4.1)$$

where i denotes the index of the OFDM symbol, k denotes the index of the subcarrier in one OFDM symbol. N is the number of subcarriers employed in the system. T_d is the duration of the data symbol carried by each subcarrier, meanwhile, $\frac{1}{T_d}$ equals to the frequency distance between adjacent

subcarriers. T_g and T_s are the duration of CP and the duration of OFDM symbol, respectively. As shown in Fig. 4.1, $T_s = T_g + T_d$.

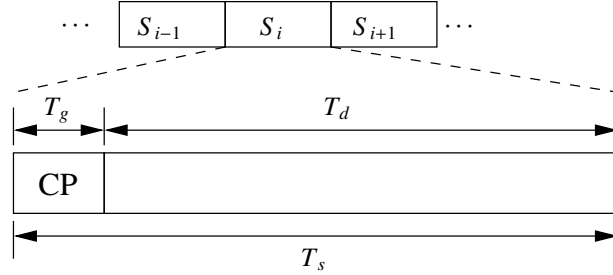


Figure 4.1: OFDM Symbols in Time Domain

The function $u(t)$ in Equation 4.1 represents the pulse shaping function of the system. To ensure the orthogonality of the subcarriers, the rectangular pulse is normally adopted and it can be expressed as

$$u(t) = \begin{cases} 1, & 0 \leq t < T_s \\ 0, & \text{else.} \end{cases} \quad (4.2)$$

The received signal is the convolution of $s_T(t)$ and the transmission channel plus additive noise. If the carrier frequency of the receiver is ideally synchronized to that of the transmitter, the baseband equivalent of the received signal at the input port of the Analog-to-Digital converter can be expressed as

$$s_R(t) = h(t) * s_T(t) + v(t) = \int_0^{\tau_L} h(\tau) s_T(t - \tau) d\tau + v(t) \quad (4.3)$$

where $v(t)$ denotes the additive white zero-mean circular symmetric complex Gaussian noise. $h(t)$ is the baseband equivalent of the transmission channel and assumed not change in the duration of one OFDM symbol. τ_L denotes the maximum delay of the channel profile and $\tau_L \geq 0$. However, the hardware imperfections will cause carrier frequency offset and Equation 4.3 should be modified in this case to

$$s_R(t) = e^{j2\pi\Delta f t} \int_0^{\tau_L} h(\tau) s_T(t - \tau) d\tau + v(t) \quad (4.4)$$

where Δf denotes the frequency offset between the transmitter and the receiver. Substituting Equation 4.1 to Equation 4.4, we obtain

$$s_R(t) = \frac{e^{j2\pi\Delta f t}}{\sqrt{T_d}} \sum_{i=-\infty}^{+\infty} \sum_{k=0}^{N-1} a_{i,k} e^{j\frac{2\pi k}{T_d}(t - T_g - iT_s)} \int_0^{\tau_L} h(\tau) e^{-j\frac{2\pi k}{T_d}\tau} u(t - iT_s - \tau) d\tau + v(t) \quad (4.5)$$

The continuous time signal is sampled with equal duration T , so the samples can be written as

$$\begin{aligned} s_R[n] &= \frac{e^{j2\pi\Delta f n T}}{\sqrt{N_d}} \sum_{i=-\infty}^{+\infty} \sum_{k=0}^{N-1} a_{i,k} e^{j\frac{2\pi k}{N_d}(n-N_g-iN_s)} \int_0^{\tau_L} h(\tau) e^{-j\frac{2\pi k}{N_d T} \tau} u(nT - iN_s T - \tau) d\tau + v[n] \\ &= \frac{e^{j2\pi\Delta f n T}}{\sqrt{N_d}} \sum_{i=-\infty}^{+\infty} \sum_{k=0}^{N-1} a_{i,k} e^{j\frac{2\pi k}{N_d}(n-N_g-iN_s)} \int_0^{\tau_L} h(\tau) e^{-j\frac{2\pi k}{N_d T} \tau} u(nT - iN_s T - \tau) d\tau + v[n] \end{aligned} \quad (4.6)$$

where we define $T_d = N_d T$, $T_g = N_g T$ and $T_s = N_s T$. Obviously, $N_s = N_g + N_d$. ΔF denotes the normalized frequency offset and it is defined as $\Delta F = \frac{\Delta f}{f_{\text{sampling}}} = \Delta f T$, which has the same definition as in Equation 3.7 for HSPA+ system.

Without loss of generality, assuming $n = pN_s + q$ and $0 \leq q \leq N_s - 1$, Equation 4.6 can be rewritten as

$$\begin{aligned} s_R[pN_s + q] &= \frac{e^{j2\pi\Delta F(pN_s+q)}}{\sqrt{N_d}} \sum_{i=-\infty}^{+\infty} \sum_{k=0}^{N-1} a_{i,k} e^{j\frac{2\pi k}{N_d}[(p-i)N_s+q-N_g]} \\ &\quad \int_0^{\tau_L} h(\tau) e^{-j\frac{2\pi k}{N_d T} \tau} u((p-i)N_s T + qT - \tau) d\tau + v[pN_s + q] \end{aligned} \quad (4.7)$$

Notice that $u(t)$ only has non-zero value when $t \in [0, T_s)$, i.e. $t \in [0, N_s T)$. Thus, the components of the first summation in Equation 4.7 may not equal zero only when $i = p-1$ and $i = p$. So Equation 4.7 can be simplified as

$$\begin{aligned} s_R[pN_s + q] &= \frac{e^{j2\pi\Delta F(pN_s+q)}}{\sqrt{N_d}} \sum_{k=0}^{N-1} a_{p-1,k} e^{j\frac{2\pi k}{N_d}(N_s+q-N_g)} \int_0^{\tau_L} h(\tau) e^{-j\frac{2\pi k}{N_d T} \tau} u(N_s T + qT - \tau) d\tau \\ &\quad + \frac{e^{j2\pi\Delta F(pN_s+q)}}{\sqrt{N_d}} \sum_{k=0}^{N-1} a_{p,k} e^{j\frac{2\pi k}{N_d}(q-N_g)} \int_0^{\tau_L} h(\tau) e^{-j\frac{2\pi k}{N_d T} \tau} u(qT - \tau) d\tau \\ &\quad + v[pN_s + q] \end{aligned} \quad (4.8)$$

Equation 4.8 shows that, the contribution of the signal to the current receive sample can only come from the previous OFDM symbol and the current OFDM symbol. The OFDM symbol synchronization process should firstly find out the correct starting point of an OFDM symbol for further processing to prevent performance loss originating from the presence of the ISI. That is to say, to find out any q_s , which can fulfill

$$\begin{cases} q_s T - \tau_L > 0 \\ q_s T + T_d < T_s \end{cases} \quad (4.9)$$

Therefore, a correct OFDM symbol synchronization algorithm should provide the starting point of an

OFDM symbol $q_s \in (\frac{\tau_L}{T}, N_g)$. And then the consecutive N_d samples from q_s on can be expressed as

$$s_R[pN_s + q_s + n_d] = \frac{e^{j2\pi\Delta F(pN_s + q_s + n_d)}}{\sqrt{N_d}} \sum_{k=0}^{N-1} a_{p,k} e^{j\frac{2\pi k}{N_d}(q_s - N_g + n_d)} \int_0^{\tau_L} h(\tau) e^{-j\frac{2\pi k}{N_d T} \tau} d\tau + v[pN_s + q_s + n_d], \quad 0 \leq n_d \leq N_d - 1 \quad (4.10)$$

Because p , q_s , N_s and N_g are all constant for just mentioned N_d samples, Equation 4.10 can be rewritten as

$$s_R^{(p,q_s)}[n_d] = \frac{e^{j[2\pi\Delta F n_d + 2\pi\Delta F(pN_s + q_s)]}}{\sqrt{N_d}} \sum_{k=0}^{N-1} H(k\Omega_c) a_{p,k} e^{j\frac{2\pi k}{N_d}(q_s - N_g + n_d)} + v^{(p,q_s)}[n_d], \quad 0 \leq n_d \leq N_d - 1 \quad (4.11)$$

where $H(\Omega)$ is the Fourier transform of the time-limited transmission channel $h(t)$, which is defined as $H(\Omega) = \int_0^{\tau_L} h(\tau) e^{-j\Omega\tau} d\tau$ [Oppenheim et al., 1999]. $\Omega_c = \frac{2\pi}{T_d}$ denotes the angular frequency distance between adjacent subcarriers.

The correlator receiver is adopted to demodulate each subcarrier [Sklar, 2001]. For example, the output of the correlator for the k_p -th subcarrier of the p -th OFDM symbol can be expressed as

$$\begin{aligned} z_p[k_p] &= \frac{1}{\sqrt{N_d}} \sum_{n_d=0}^{N_d-1} s_R^{(p,q_s)}[n_d] e^{-j(k_p \Omega_c n_d T)} \\ &= e^{j2\pi\Delta F(pN_s + q_s)} \sum_{k=0}^{N-1} H(k\Omega_c) e^{j\frac{2\pi k}{N_d}(q_s - N_g)} a_{p,k} \left[\frac{1}{N_d} \sum_{n_d=0}^{N_d-1} e^{j2\pi\Delta F n_d} e^{j\frac{2\pi}{N_d}(k - k_p)n_d} \right] \\ &\quad + \frac{1}{\sqrt{N_d}} \sum_{n_d=0}^{N_d-1} v^{(p,q_s)}[n_d] e^{j\frac{2\pi}{N_d} k_p n_d} \\ &= e^{j2\pi\Delta F(pN_s + q_s)} \sum_{k=0}^{N-1} H(k\Omega) e^{j\frac{2\pi k}{N_d}(q_s - N_g)} \hat{a}_{p,k} \left[\frac{1}{N_d} \sum_{n_d=0}^{N_d-1} e^{j2\pi\Delta F n_d} e^{j\frac{2\pi}{N_d}(k - k_p)n_d} \right] \\ &\quad + \varpi_p[k_p] \end{aligned} \quad (4.12)$$

where $\varpi[k_p]$ denotes the contribution from the additive noise to the output of the correlator and it is defined as

$$\varpi_p[k_p] = \frac{1}{\sqrt{N_d}} \sum_{n_d=0}^{N_d-1} v^{(p,q_s)}[n_d] e^{j\frac{2\pi}{N_d} k_p n_d} \quad (4.13)$$

We have assumed that $v(t)$ is additive white zero-mean circular symmetric complex Gaussian noise. Therefore, $v^{(p,q_s)}[n_d]$ are i.i.d. random variables with zero-mean circular symmetric complex Gaussian distribution. Because a circular symmetric Gaussian random variable will not change its distribution when it is multiplied with a phase rotator Tse and Viswanath [2005], $\varpi_p[k_p]$ is then the summation of circular symmetric Gaussian random variables and it is also a circular symmetric Gaussian random

variable. Meanwhile, taking $\text{Var}(v^{(p,q_s)}[n_d]) = \sigma_v^2$, we have

$$\text{Var}(\varpi_p[k_p]) = \frac{1}{N_d} \sum_{n_d=0}^{N_d-1} \text{Var}(v^{(p,q_s)}[n_d]) = \sigma_v^2 \quad (4.14)$$

4.2 Impact of Frequency Offset on the Output of the Correlator

Investigating the summation inside the square brackets of Equation 4.12, if the frequency offset ΔF is absent, it can be simplified as

$$\frac{1}{N_d} \sum_{n_d=0}^{N_d-1} e^{j\frac{2\pi}{N_d}(k-k_p)n_d} = \delta_{k,k_p} \quad (4.15)$$

where δ_{k,k_p} is the Kronecker delta defined in Equation 3.11. Therefore, the output of the correlator for the k_p -th subcarrier in the case without frequency offset degenerates to

$$\begin{aligned} z_p[k_p] &= e^{j\frac{2\pi k_p}{N_d}(q_s - N_g)} H(k_p \Omega_c) a_{p,k_p} + \varpi_p[k_p] \\ &= H_E(k_p \Omega_c) a_{p,k_p} + \varpi_p[k_p] \end{aligned} \quad (4.16)$$

where $H_E(k_p \Omega_c)$ denotes the effective channel frequency response at the angular frequency $\Omega = k_p \Omega_c$, which comprises the frequency response of the channel at the angular frequency $\Omega = k_p \Omega_c$ and a phase rotation of $\frac{2\pi k_p}{N_d}(q_s - N_g)$. It is obvious from Equation 4.16 that in the case without frequency offset and with correct OFDM symbol synchronization, the transmission by each subcarrier is equivalent to a traditional single carrier transmission through a frequency-nonsselective fading channel [Proakis, 2000], no matter whether the transmission channel of the whole system $h(t)$ is frequency-selective or not. Therefore, the wideband transmission channel is divided into multiple frequency-nonsselective narrow band transmission channels and the low-complexity linear equalizer with only one tap, such as the ZF equalizer expressed in Equation 4.17 or the *Minimum Mean Square Error (MMSE)* equalizer expressed in Equation 4.18, can be employed to help correctly detecting the transmitted data symbol carried by each subcarrier.

$$\text{ZF equalizer :} \quad \tilde{a}_{p,k_p} = \frac{H_E^*(k_p \Omega_c)}{|H_E(k_p \Omega_c)|^2} z_p[k_p] \quad (4.17)$$

$$\text{MMSE equalizer :} \quad \tilde{a}_{p,k_p} = \frac{H_E^*(k_p \Omega_c)}{|H_E(k_p \Omega_c)|^2 + \frac{\sigma_v^2}{\sigma_a^2}} z_p[k_p] \quad (4.18)$$

Meanwhile, Equation 4.16 shows us that the SNR of $z_p[k_p]$ in the case without frequency offset is only affected by the noise power σ_v^2 and the amplitude factor of the effective channel $|H_E(k_p \Omega_c)|$.

However, if the frequency offset is present, the summation in the square bracket can not be simpli-

fied by using Equation 4.15. We rewrite Equation 4.12 to

$$z_p[k_p] = e^{j2\pi\Delta F(pN_s+q_s)} \sum_{k=0}^{N-1} H_E(k\Omega_c) I_p[k, k_p] + \varpi_p[k_p] \quad (4.19)$$

where

$$I_p[k, k_p] = \frac{1}{N_d} \sum_{n_d=0}^{N_d-1} a_{p,k} e^{j2\pi\Delta F n_d} e^{j\frac{2\pi}{N_d}(k-k_p)n_d} \quad (4.20)$$

Specially, when $k = k_p$, we have

$$I_p[k_p, k_p] = \frac{1}{N_d} \sum_{n_d=0}^{N_d-1} a_{p,k_p} e^{j2\pi\Delta F n_d} = \frac{\sin(\pi\Delta F N_d)}{N_d \sin(\pi\Delta F)} e^{j\pi(N_d-1)\Delta F} a_{p,k_p} \quad (4.21)$$

Thus, Equation 4.12 can be further rewritten to

$$\begin{aligned} z_p[k_p] &= \frac{\sin(\pi\Delta F N_d)}{N_d \sin(\pi\Delta F)} e^{j\pi(N_d-1)\Delta F} e^{j2\pi\Delta F(pN_s+q_s)} H_E(k_p\Omega_c) a_{p,k_p} \\ &\quad + e^{j2\pi\Delta F(pN_s+q_s)} \sum_{\substack{k=0 \\ k \neq k_p}}^{N-1} H_E(k\Omega_c) I_{k,k_p} + \varpi_p[k_p] \\ &= \frac{\sin(\pi\Delta F N_d)}{N_d \sin(\pi\Delta F)} e^{j\pi(N_d-1)\Delta F} e^{j2\pi\Delta F(pN_s+q_s)} H_E(k_p\Omega_c) a_{p,k_p} + ICI_p[k_p] + \varpi_p[k_p] \end{aligned} \quad (4.22)$$

where $ICI_p[k_p]$ denotes the interference on the k_p -th subcarrier of the p -th OFDM symbol, which is contributed by the other subcarriers of the p -th OFDM symbol. Therefore, we entitle it **ICI** and it is defined as

$$ICI_p[k_p] = e^{j2\pi\Delta F(pN_s+q_s)} \sum_{\substack{k=0 \\ k \neq k_p}}^{N-1} H_E(k\Omega_c) I_p[k, k_p] \quad (4.23)$$

Comparing Equation 4.22 and 4.23 to Equation 3.14 and 3.15, we find out that, in the case of slow flat fading transmission channel, the signal model of the OFDM system has the same form as that of the CDMA system. Therefore, similar to the HSPA+ system, the impairments caused by the frequency offset rotate and attenuate the desired data symbol. In addition, signal components originating from subcarriers other than the considered one give rise to ICI.

Lemma 4.1. Suppose $a_{p,k}$ are i.i.d. random variables with zero mean and variance $E\{|a_{p,k}^2|\} = \sigma_a^2$ and $E\{|H_E(k\Omega_c)|^2\} = \mathcal{E}_h$ for all subcarriers noted by k . Then the following equality holds

$$E\left\{\left|\sum_{k=0}^{N_d-1} H_E(k\Omega_c) I_p[k, k_p]\right|^2\right\} = \mathcal{E}_h \sigma_a^2 \quad (4.24)$$

Proof. Similar to the proof for Equation 3.22, because $a_{p,k}$ are mutual independent, we obtain

$$E \left\{ \left| \sum_{k=0}^{N_d-1} H_E(k\Omega_c) I_p[k, k_p] \right|^2 \right\} = E \left\{ \sum_{k=0}^{N_d-1} |H_E(k\Omega_c) I_p[k, k_p]|^2 \right\} \quad (4.25)$$

Replacing $I_p[k, k_p]$ in the RHS of Equation 4.25 with Equation 4.20, we get

$$\begin{aligned} E \left\{ \sum_{k=0}^{N_d-1} |H_E(k\Omega_c) I_p[k, k_p]|^2 \right\} &= \sum_{k=0}^{N_d-1} E \left\{ |H_E(k\Omega_c)|^2 I_p[k, k_p] I_p^*[k, k_p] \right\} \\ &= \frac{\mathcal{E}_h \sigma_a^2}{N_d^2} \sum_{k=0}^{N_d-1} \sum_{m=0}^{N_d-1} \sum_{n=0}^{N_d-1} e^{j2\pi\Delta F(m-n)} e^{j\frac{2\pi}{N_d}(k-k_p)(m-n)} \\ &= \mathcal{E}_h \sigma_a^2 \frac{1}{N_d} \sum_{m=0}^{N_d-1} \sum_{n=0}^{N_d-1} e^{j2\pi\Delta F(m-n)} e^{j\frac{2\pi}{N_d}k_p(m-n)} \frac{1}{N_d} \sum_{k=0}^{N_d-1} e^{j\frac{2\pi}{N_d}(m-n)k} \\ &= \mathcal{E}_h \sigma_a^2 \frac{1}{N_d} \sum_{m=0}^{N_d-1} \sum_{n=0}^{N_d-1} e^{j2\pi\Delta F(m-n)} e^{j\frac{2\pi}{N_d}k_p(m-n)} \delta_{m,n} \\ &= \mathcal{E}_h \sigma_a^2 \end{aligned} \quad (4.26)$$

□

According to Equation 4.21, we have

$$E \left\{ |H_E(k_p\Omega_c) I_p[k_p, k_p]|^2 \right\} = \frac{\sin^2(\pi\Delta FN_d)}{N_d^2 \sin^2(\pi\Delta F)} \mathcal{E}_h \sigma_a^2 \quad (4.27)$$

Therefore, if the number of subcarriers $N = N_d$, according to Equation 4.23, we obtain

$$\begin{aligned} \sigma_{ICI}^2 &= E \left\{ \left| e^{j2\pi\Delta F(pN_s+q_s)} \sum_{\substack{k=0 \\ k \neq k_p}}^{N_d-1} H_E(k\Omega_c) I_p[k, k_p] \right|^2 \right\} \\ &= E \left\{ \sum_{k=0}^{N_d-1} |H_E(k\Omega_c) I_p[k, k_p]|^2 \right\} - E \left\{ |H_E(k_p\Omega_c) I_p[k_p, k_p]|^2 \right\} \\ &= \mathcal{E}_h \sigma_a^2 \left[1 - \frac{\sin^2(\pi\Delta FN_d)}{N_d^2 \sin^2(\pi\Delta F)} \right] = \mathcal{E}_h \sigma_a^2 (1 - \beta^2) \end{aligned} \quad (4.28)$$

where $\beta = \frac{\sin(\pi\Delta FN_d)}{N_d \sin(\pi\Delta F)}$ is defined as the amplitude attenuation factor caused by the frequency offset.

4.3 Discussion of the Impairments caused by the Frequency Offset in LTE system and HSPA+ system

Through comparing Equation 4.22, 4.23 and 4.28 to Equation 3.14, 3.15 and 3.26, we discover that the impairments arising from the frequency offset have the same form in both OFDM system and HSPA+ system, if all the subcarriers of the OFDM system and all the HS-PDSCHs are used in the systems, although OFDM system belongs to multi-carrier system and HSPA+ belongs to single-carrier system.

It is also quite obvious that the amplitude attenuation factor caused by the frequency offset is a key role of assessing the impairments. We recall them here and denote them as β_c and β_o for the HSPA+ system and OFDM system, respectively.

$$\beta_c = \frac{\sin(\pi\Delta FW)}{W \sin(\pi\Delta F)} \quad (4.29a)$$

$$\beta_o = \frac{\sin(\pi\Delta FN_d)}{N_d \sin(\pi\Delta F)} \quad (4.29b)$$

ΔF in the equations denotes the normalized frequency offset and it has the same definition in the CDMA system and the OFDM system as $\Delta F = \frac{\Delta f}{f_{\text{sampling}}}$. In a practical system Δf is normally 4 ~ 5 orders of magnitude smaller than f_{sampling} . Therefore, $\pi\Delta F \ll 1$ and $\sin(\pi\Delta F) \approx \pi\Delta F$. β_c and β_o can then be rewritten to

$$\beta_c = \frac{\sin(\pi\Delta FW)}{\pi\Delta FW} = \text{Sinc}(W\Delta F) \quad (4.30a)$$

$$\beta_o = \frac{\sin(\pi\Delta FN_d)}{\pi\Delta FN_d} = \text{Sinc}(N_d\Delta F) \quad (4.30b)$$

Recall Equation 3.71, for HSPA+ system we have

$$\beta_c = \text{Sinc}\left(\frac{\Delta f}{R_{\text{sym}}}\right) = \text{Sinc}(\Delta\mathcal{F}) \quad (4.31)$$

where $R_{\text{sym}} = \frac{f_{\text{chip}}}{W}$ depicts the symbol rate of the HS-PDSCH and $\Delta\mathcal{F}$ is the frequency offset normalized to the symbol rate.

For the OFDM system, we can also have

$$N_d\Delta F = N_d \frac{\Delta f}{f_{\text{sampling}}} = \Delta f N_d T = \Delta f T_d = \frac{\Delta f}{R_{\text{sym}}} = \Delta\mathcal{F} \quad (4.32)$$

where R_{sym} depicts the symbol rate of each subcarrier before adding CP. Substituting Equation 4.32 to Equation 4.30b, we get

$$\beta_o = \text{Sinc}(\Delta\mathcal{F}) \quad (4.33)$$

So far, we can find that β_c and β_o have exactly the same form, if we normalize the frequency offset to the symbol rate of the single transmission resource, which is one HS-PDSCH for the HSPA+

system and one subcarrier for the OFDM system. On the one hand, some conclusions for the OFDM system fit also to the HSPA+ system. For instance, the approximated SNR degradation factor in Equation 4.34 for the OFDM system [Pollet *et al.*, 1995] is also suitable for the HSPA+ system.

$$D \approx \frac{10}{\ln 10} \frac{1}{3} (\pi \Delta \mathcal{F})^2 \frac{E_s}{N_0} \quad (4.34)$$

Therefore, not like the single carrier system with *Time Division Multiplex (TDM)* technique or the single carrier system with CP [Pollet and Moeneclaey, 1996], the degradation factor D of HSPA+ system is not only proportional to the square of the frequency offset $\Delta \mathcal{F}$, but also proportional to the received SNR.

On the other hand, the analysis on the degradation of the system performance in Chapter 3 for the HSPA+ system can be also reused here for the OFDM system. We recall the results in Figure 3.12 and replace the absolute frequency offset Δf with the normalized frequency offset $\Delta \mathcal{F}$ by taking $R_{\text{sym}} = \frac{3.84 \text{ MHz}}{16} = 240 \text{ kHz}$.

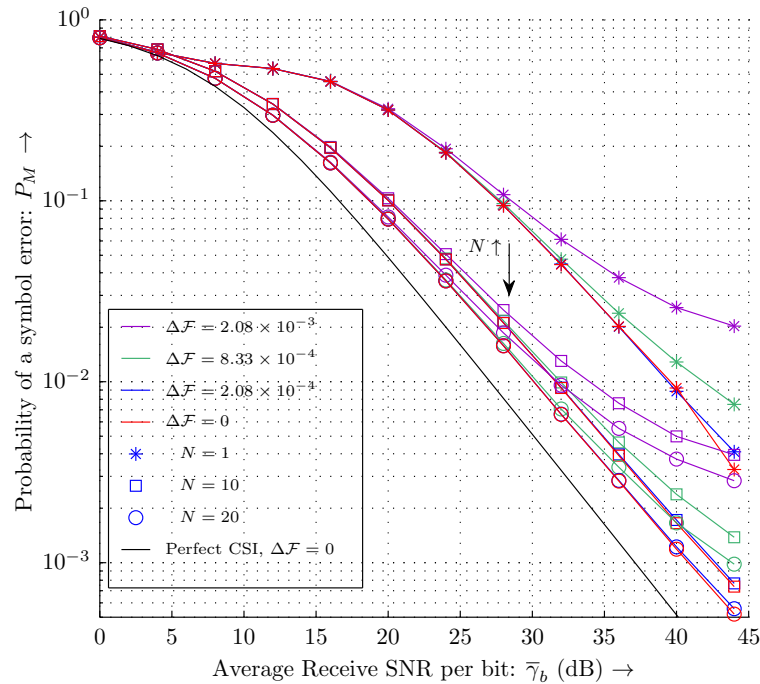


Figure 4.2: SER curves comparison: channel estimator with different average lengths

The results in Figure 4.2 illustrate that the frequency offset $\Delta \mathcal{F}$ should be kept below 3×10^{-4} in the presence of the channel estimation error to ensure small performance loss arising from the frequency offset, which corresponds to 4.5 Hz for the LTE system with $R_{\text{sym}} = 15 \text{ kHz}$. Obviously, the system based on OFDM technique is much more sensitive to the frequency offset compared to the single carrier system.

The modern digital communication systems employ channel coding/decoding technique to combat

the receive errors caused by channel fading, transient noise and hardware imperfections. Although the channel coding/decoding function can relax the requirement of the frequency synchronization, the larger frequency offset requires stronger channel coding scheme at the cost of more overhead and higher computation complexity.

4.4 Impact of Frequency Offset on the Uplink of LTE System

The previous analysis has shown that the performance of the OFDM-based systems is sensitive to the frequency offset. It gets even worse for the uplink transmission of LTE system, because different User Equipments (UEs) can exhibit different frequency offsets to the *Base Station (BS)*. Meanwhile, different resource allocation schemes for multiple UEs affect also the sensitivity of the system to the frequency offset.

Figure 4.3 sketches two most common resource allocation schemes, the interleaved mapping scheme, which is also referenced as *IFDMA*, and the localized mapping scheme, which is also called *LFDMA* [Ekstrom et al., 2006].

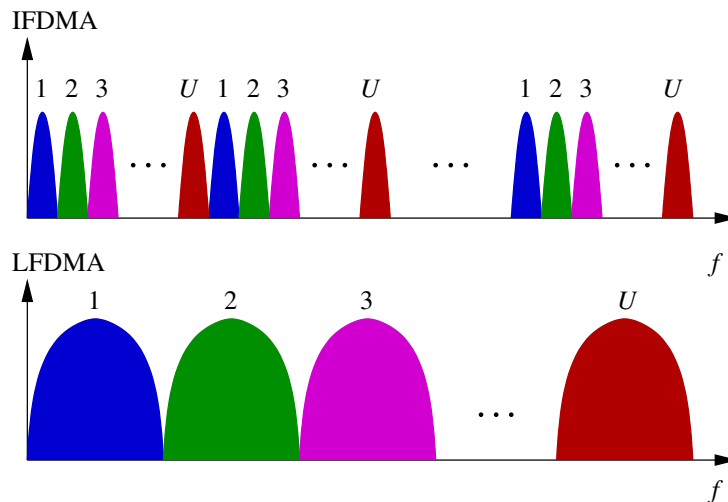


Figure 4.3: Subcarrier Mapping of IFDMA and LFDMA

In this section we would like to investigate the impairments arising from the user-specific frequency offset on the *SC-FDMA* system with aforementioned two different subcarrier mapping schemes.

4.4.1 Matrix Expression of the OFDM System and SC-FDMA System

Based on the framework we provided in [Wilzeck et al., 2007], the matrix expression of the p -th decision symbol block in the presence of frequency offset is obtained by stacking $z_p[k_p]$ in Equation 4.19

as

$$\begin{aligned}
\mathbf{Z}_p &= [z_p[0], z_p[1], \dots, z_p[N-1]]^T \\
&= e^{j\Delta F(pN_s+q_s)} \mathbf{W} \Delta_{\text{CFO}} \mathbf{H}_c \mathbf{W}^{-1} \mathbf{a}_p + \mathbf{W} \boldsymbol{\nu}_p \\
&= \mathbf{W} \Delta_{\text{CFO}} \tilde{\mathbf{H}}_c \mathbf{W}^{-1} \mathbf{a}_p + \boldsymbol{\varpi}_p
\end{aligned} \tag{4.35}$$

where $[\cdot]^T$ denotes the matrix transpose operation. \mathbf{H}_c is the circulant channel matrix obtained by employing CP adding and removing process [Starr *et al.*, 2003] and $\tilde{\mathbf{H}}_c$ denotes the equivalent circulant matrix after \mathbf{H}_c absorbs the initial phase rotation $e^{j\Delta F(pN_s+q_s)}$ originating from the frequency offset. \mathbf{W}^{-1} and \mathbf{W} denote the IDFT and DFT matrix with dimension $N_d \times N_d$ [Lin and Phoong, 2003], respectively. Δ_{CFO} is the diagonal matrix, which represents the continuous phase rotation of the received samples caused by the frequency offset and has the elements $[\Delta_{\text{CFO}}]_{n,n} = e^{j2\pi\Delta F n}$. \mathbf{a}_p denotes the data symbol vector. $\boldsymbol{\varpi}_p$ represents the equivalent noise vector for the current decision symbol block.

As previously mentioned, SC-FDMA system is also referred to DFT-Spread OFDM system. In order to reduce the high PAPR of the OFDM system, the data symbols will be first processed by a DFT matrix before assigned to the subcarriers. Not like the downlink, which is a point-to-multipoint communication, the uplink is a multipoint-to-point communication. In the SC-FDMA system, different UEs not only occupy different subcarriers, but also exhibit different frequency offsets to the common BS. Therefore, the p -th decision symbol block for all UEs at the BS can be expressed as

$$\mathbf{Z}_p = \mathbf{W} \sum_{u=1}^U \Delta_{\text{CFO}}^{(u)} \tilde{\mathbf{H}}_c^{(u)} \mathbf{W}^{-1} \mathbf{M}^{(u)} \mathbf{F}^{(u)} \mathbf{a}_p^{(u)} + \boldsymbol{\varpi}_p \tag{4.36}$$

where U is the number of the UEs. The user terminal index u indicates that the value is user-specific. $\mathbf{F}^{(u)}$ and $\mathbf{M}^{(u)}$ are the DFT matrix and the subcarrier mapping matrix for the u -th UE, respectively, which are all known by the BS. Without loss generality, the first UE is assumed to be desired, its decision symbol vector can be expressed as

$$\begin{aligned}
\mathbf{Z}_p^{(1)} &= [\mathbf{F}^{(1)}]^{-1} [\mathbf{M}^{(1)}]^{-1} \mathbf{Z}_p \\
&= [\mathbf{F}^{(1)}]^{-1} [\mathbf{M}^{(1)}]^\dagger \mathbf{W} \sum_{u=1}^U \Delta_{\text{CFO}}^{(u)} \tilde{\mathbf{H}}_c^{(u)} \mathbf{W}^{-1} \mathbf{M}^{(u)} \mathbf{F}^{(u)} \mathbf{a}_p^{(u)} + \boldsymbol{\varpi}_p^{(1)}
\end{aligned} \tag{4.37}$$

where $[\mathbf{F}^{(1)}]^{-1}$ is the inverse matrix of the DFT-spread matrix for the desired UE. $[\mathbf{M}^{(1)}]^\dagger$ is the pseudoinverse matrix of the subcarrier mapping matrix for the desired UE. $\boldsymbol{\varpi}_p^{(1)}$ denotes the noise component for the desired UE and $\boldsymbol{\varpi}_p^{(1)} = [\mathbf{F}^{(1)}]^{-1} [\mathbf{M}^{(1)}]^\dagger \boldsymbol{\varpi}_p$.

4.4.2 Effect of User-Specific Frequency Offsets on the SC-FDMA system

We know that OFDM-based systems are sensitive to the frequency offset. To prevent the performance loss, the receiver should first estimate the frequency offset and then compensate it before making

decision. Therefore, we assume that the frequency offset of the desired UE is correctly compensated and Equation 4.37 is then rewritten as

$$\begin{aligned}
\tilde{\mathbf{z}}_p^{(1)} &= [\mathbf{F}^{(1)}]^{-1} [\mathbf{M}^{(1)}]^\dagger \mathbf{W} [\Delta_{\text{CFO}}^{(1)}]^{-1} \sum_{u=1}^U \Delta_{\text{CFO}}^{(u)} \tilde{\mathbf{H}}_c^{(u)} \mathbf{W}^{-1} \mathbf{M}^{(u)} \mathbf{F}^{(u)} \mathbf{a}_p^{(u)} + \tilde{\mathbf{w}}_p^{(1)} \\
&= [\mathbf{F}^{(1)}]^{-1} [\mathbf{M}^{(1)}]^\dagger \mathbf{W} \tilde{\mathbf{H}}_c^{(1)} \mathbf{W}^{-1} \mathbf{M}^{(1)} \mathbf{F}^{(1)} \mathbf{a}_p^{(1)} + \\
&\quad [\mathbf{F}^{(1)}]^{-1} [\mathbf{M}^{(1)}]^\dagger \mathbf{W} \sum_{u=2}^U \Delta_{\text{RFO}}^{(1,u)} \tilde{\mathbf{H}}_c^{(u)} \mathbf{W}^{-1} \mathbf{M}^{(u)} \mathbf{F}^{(u)} \mathbf{a}_p^{(u)} + \tilde{\mathbf{w}}_p^{(1)} \\
&= [\mathbf{F}^{(1)}]^{-1} [\mathbf{M}^{(1)}]^\dagger \Lambda^{(1)} \mathbf{M}^{(1)} \mathbf{F}^{(1)} \mathbf{a}_p^{(1)} + \\
&\quad \underbrace{[\mathbf{F}^{(1)}]^{-1} [\mathbf{M}^{(1)}]^\dagger \mathbf{W} \sum_{u=2}^U \Delta_{\text{RFO}}^{(1,u)} \tilde{\mathbf{H}}_c^{(u)} \mathbf{W}^{-1} \mathbf{M}^{(u)} \mathbf{F}^{(u)} \mathbf{a}_p^{(u)} + \tilde{\mathbf{w}}_p^{(1)}}_{\text{interference originating from other UEs}}
\end{aligned} \tag{4.38}$$

where $\Lambda^{(1)} = \mathbf{W} \tilde{\mathbf{H}}_c^{(1)} \mathbf{W}^{-1}$. Because the column vector of the DFT matrix is the eigen vector of the circulant matrix [Gray, 2006], $\Lambda^{(1)}$ is a diagonal matrix. The matrix $\Delta_{\text{RFO}}^{(1,u)}$ is a diagonal matrix to describe the remaining frequency offset of the u -th UE after correcting the frequency offset of the desired UE. The elements of the matrix are given as

$$[\Delta_{\text{RFO}}^{(1,u)}]_{n,n} = e^{j2\pi\Delta F^{(1,u)}} = e^{j2\pi[\Delta F^{(u)} - \Delta F^{(1)}]n} \tag{4.39}$$

The absolute value of the remaining frequency offset of the u -th UE $|\Delta F^{(1,u)}| = |\Delta F^{(u)} - \Delta F^{(1)}|$ can be greater than $|\Delta F^{(u)}|$, which means that frequency offset correction for the desired UE can cause additional interference to the desired UE arising from the remaining frequency offset of other UEs. Therefore, for the uplink of the LTE system, the frequency offset of all the UEs $\{\Delta F^{(u)}\}$ should be maintained per user on the entire received signal [Wilzcek et al., 2007].

We will now further analyze the interference to the desired UE originating from the signal of other UEs with the remaining frequency offsets after frequency offset compensation of the desired UE.

The exponential function e^x can be approximated as follows by using its Taylor series, when $|x| \ll 1$.

$$e^x = \sum_{n=0}^{\infty} \frac{x^n}{n!} \approx 1 + x, \quad \forall |x| \ll 1 \tag{4.40}$$

Since $|\Delta F^{(u)} - \Delta F^{(1)}|$ is in practical systems in the order of $10^{-4} \sim 10^{-3}$, by taking $\Delta F^{(1,u)} = \Delta F^{(u)} - \Delta F^{(1)}$, we can write

$$\Delta_{\text{RFO}}^{(1,u)} \approx \mathbf{I}_{N_d} + j2\pi\Delta F^{(1,u)} \mathbf{C} \tag{4.41}$$

where $\mathbf{C} = \text{diag}(0, 1, 2, \dots, N_d - 1)$. Then, the second term of the RHS of Equation 4.38, i.e. the interference originating from other UEs to the p -th decision symbol block of the desired UE, can be

rewritten to

$$\begin{aligned}
\mathbf{m}_p^{(1)} &= [\mathbf{F}^{(1)}]^{-1} [\mathbf{M}^{(1)}]^\dagger \mathbf{W} \sum_{u=2}^U \Delta_{\text{RFO}}^{(1,u)} \tilde{\mathbf{H}}_c^{(u)} \mathbf{W}^{-1} \mathbf{M}^{(u)} \mathbf{F}^{(u)} \mathbf{a}_p^{(u)} \\
&\approx [\mathbf{F}^{(1)}]^{-1} [\mathbf{M}^{(1)}]^\dagger \mathbf{W} \sum_{u=2}^U [\mathbf{I}_{N_d} + j2\pi\Delta F^{(1,u)} \mathbf{C}] \tilde{\mathbf{H}}_c^{(u)} \mathbf{W}^{-1} \mathbf{M}^{(u)} \mathbf{F}^{(u)} \mathbf{a}_p^{(u)} \\
&= [\mathbf{F}^{(1)}]^{-1} [\mathbf{M}^{(1)}]^\dagger \sum_{u=2}^U \Lambda^{(u)} \mathbf{M}^{(u)} \mathbf{F}^{(u)} \mathbf{a}_p^{(u)} + \\
&\quad [\mathbf{F}^{(1)}]^{-1} [\mathbf{M}^{(1)}]^\dagger \sum_{u=2}^U j2\pi\Delta F^{(1,u)} \mathbf{W} \mathbf{C} \tilde{\mathbf{H}}_c^{(u)} \mathbf{W}^{-1} \mathbf{M}^{(u)} \mathbf{F}^{(u)} \mathbf{a}_p^{(u)}
\end{aligned} \tag{4.42}$$

Because different UEs should occupy different subcarrier sets, the subcarrier mapping matrices hold

$$[\mathbf{M}^{(u)}]^\dagger \Lambda \mathbf{M}^{(v)} = \mathbf{0}, \quad \text{if } \Lambda \text{ is a diagonal matrix and } u \neq v \tag{4.43}$$

Therefore, Equation 4.42 can be simplified to

$$\begin{aligned}
\mathbf{m}_p^{(1)} &\approx [\mathbf{F}^{(1)}]^{-1} [\mathbf{M}^{(1)}]^\dagger \sum_{u=2}^U j2\pi\Delta F^{(1,u)} \mathbf{W} \mathbf{C} \tilde{\mathbf{H}}_c^{(u)} \mathbf{W}^{-1} \mathbf{M}^{(u)} \mathbf{F}^{(u)} \mathbf{a}_p^{(u)} \\
&= [\mathbf{F}^{(1)}]^{-1} [\mathbf{M}^{(1)}]^\dagger \sum_{u=2}^U \underbrace{j2\pi\Delta F^{(1,u)} \mathbf{W} \mathbf{C} \mathbf{W}^{-1} \Lambda^{(u)}}_{\mathbf{B}^{(1,u)}} \mathbf{M}^{(u)} \mathbf{F}^{(u)} \mathbf{a}_p^{(u)}
\end{aligned} \tag{4.44}$$

where $\Lambda^{(u)} = \mathbf{W} \tilde{\mathbf{H}}_c^{(u)} \mathbf{W}^{-1}$ are diagonal matrices.

Of special interest is now the term

$$\mathbf{B}^{(1,u)} = j2\pi\Delta F^{(1,u)} \mathbf{W} \mathbf{C} \mathbf{W}^{-1} \tag{4.45}$$

which is responsible for the interference from the u -th UE to the desired UE.

Upon taking the element from $\mathbf{B}^{(1,u)}$, we have

$$[\mathbf{B}^{(1,u)}]_{i,j} = j2\pi\Delta F^{(1,u)} \sum_{l=0}^{N_d-1} \sum_{k=0}^{N_d-1} \mathbf{W}_{i,k} \mathbf{C}_{k,l} \mathbf{W}_{l,j}^{-1} \tag{4.46}$$

Using the result in Appendix F, we have

$$[\mathbf{B}^{(1,u)}]_{i,j} = j2\pi\Delta F^{(1,u)} \cdot \begin{cases} \frac{N_d - 1}{2}, & i = j \\ \frac{1}{e^{-j\frac{2\pi}{N_d}(j-i)} - 1}, & i \neq j \end{cases} \tag{4.47}$$

The element $[\mathbf{B}^{(1,u)}]_{i,j}$ can be seen as a factor to indicate the interference arising from the subcarrier j of the u -th UE to the subcarrier i of the desired UE. However, whether the interference is really

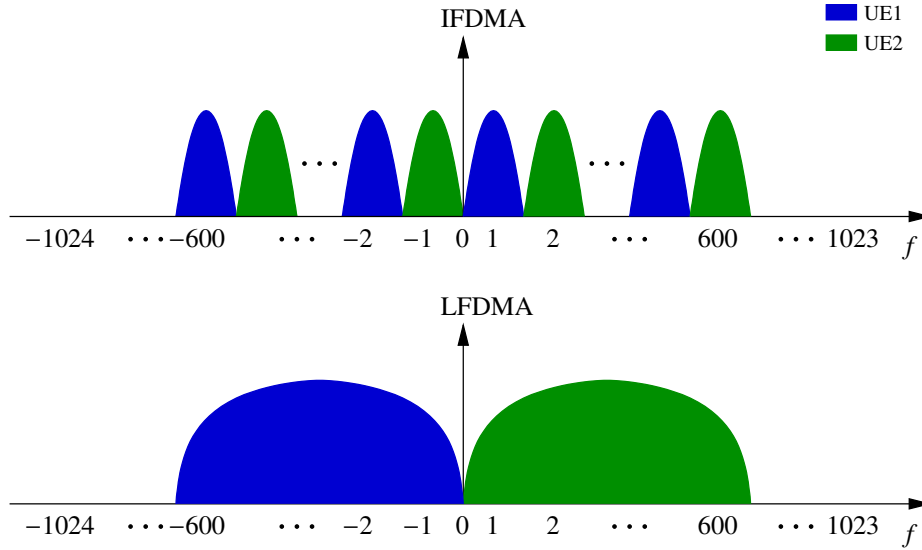


Figure 4.4: Example: IFDMA and LFDMA with two UEs

generated, it depends on whether the subcarrier i and subcarrier j are assigned to the desired UE and the u -th UE, respectively.

To simplify the analysis, we take the AWGN transmission channel, then $\Lambda^{(u)}$ degenerate to identity matrices and Equation 4.44 can be expressed as

$$\begin{aligned}
 \mathbf{m}_p^{(1)} &\approx [\mathbf{F}^{(1)}]^{-1} \sum_{u=2}^U [\mathbf{M}^{(1)}]^\dagger \mathbf{B}^{(1,u)} \mathbf{M}^{(u)} \mathbf{F}^{(u)} \mathbf{a}_p^{(u)} \\
 &= [\mathbf{F}^{(1)}]^{-1} \sum_{u=2}^U \widetilde{\mathbf{B}}^{(1,u)} \mathbf{F}^{(u)} \mathbf{a}_p^{(u)} \\
 &= [\mathbf{F}^{(1)}]^{-1} \mathbf{ICI}_p^{(1)}
 \end{aligned} \tag{4.48}$$

where $\widetilde{\mathbf{B}}^{(1,u)}$ is the interference factor matrix for the u -th UE and the desired UE and is defined as

$$\widetilde{\mathbf{B}}^{(1,u)} = [\mathbf{M}^{(1)}]^\dagger \mathbf{B}^{(1,u)} \mathbf{M}^{(u)} \tag{4.49}$$

The interference vector $\mathbf{ICI}_p^{(1)} = \sum_{u=2}^U \widetilde{\mathbf{B}}^{(1,u)} \mathbf{F}^{(u)} \mathbf{a}_p^{(u)}$ describes the interference originating from other UEs to the subcarriers of the desired UE. Note that the interference on the decision symbols is generated by taking the IDFT of the interference on the subcarriers.

Different matrix sets $\{\mathbf{M}^{(u)}\}$ correspond to different subcarrier mapping schemes. It is obvious from Equation 4.49 that subcarrier mapping schemes affect the interference among UEs. The aforementioned LFDMA system and IFDMA system with two UEs are taken as an example to illustrate the effect of different subcarrier mapping schemes on the interference. The LTE system has maximal 2048 subcarriers, i.e. $N_d = 2048$. Given the system with 20 MHz bandwidth, there are 1200 available subcarriers around DC subcarrier shown as in Figure 4.4 and each UE occupies 600 subcarriers.

Therefore, the size of $\mathbf{B}^{(1,u)}$ is 2048×2048 . $\mathbf{M}^{(u)}$ describe 2048×600 subcarrier mapping matrices and the interference factor matrix $\tilde{\mathbf{B}}^{(1,2)}$ has a dimension of 600×600 . Figure 4.5 shows the results of $\mathbf{m}_p^{(1)}$ and $\mathbf{ICI}_p^{(1)}$ in a AWGN channel.

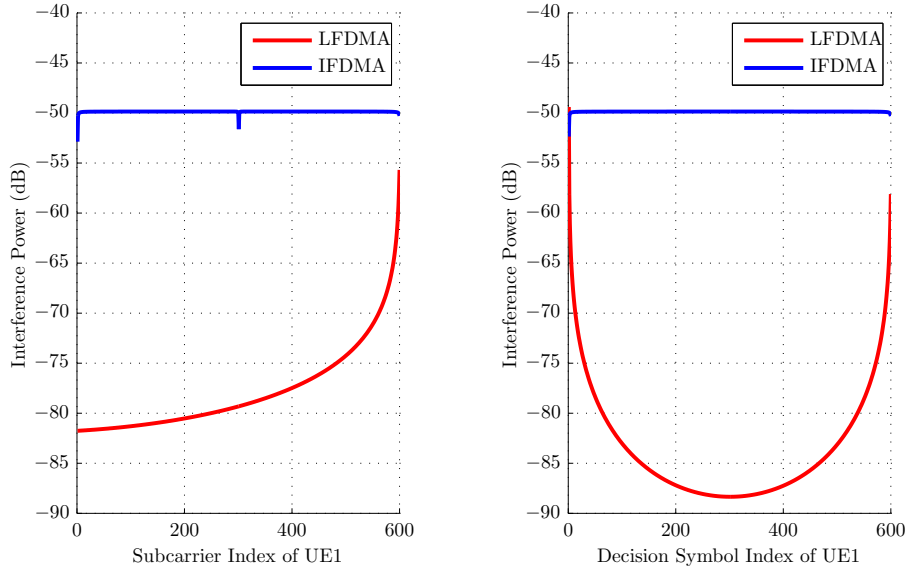


Figure 4.5: Interference Power to UE1. Parameters: $U = 2$, $\Delta F^{(1,2)} = 10^{-6}$, $N_d = 2048$, $N^{(u)} = 600$, Zeroed DC subcarrier.

When we investigate the interference on the subcarriers $\mathbf{ICI}_p^{(1)}$, in the case of LFDMA scheme UE1 observes significant interference power near the border between the two UE locations in the spectrum, whereas the IFDMA scheme results in an almost constant interference power for all subcarriers of UE1. The small down peak in the result for the IFDMA scheme near the central subcarriers is generated by the zeroed DC carrier. When we investigate the interference on the decision symbols $\mathbf{m}_p^{(1)}$, we find out that, in the case of LFDMA scheme the IDFT process in Equation 4.48 spreads the interference on the subcarriers to the decision symbols so as that the interference on the decision symbols is almost symmetric to the central symbol of the symbol block. The IDFT process redistributes the interference power more uniformly and helps to reduce the number of decision symbols with high interference power and improves the system performance. If -80 dB is chosen as the target, it is shown from Figure 4.5 that in the case of LFDMA scheme the number of decision symbols with the interference above the target is much smaller than the number of the subcarriers with the interference above the target. However, the IDFT process will not improve the distribution of the interference power in the case of IFDMA scheme, because the interference caused by the user-specific frequency offset is already uniformly distributed on the subcarriers in the IFDMA scheme.

Figure 4.5 also shows us that no matter on the subcarriers or on the decision symbols, the interference caused by the user-specific frequency offset in IFDMA system is much stronger than that of the LFDMA system, except the subcarriers or the decision symbols near the border. Hence, the IFDMA system is much more sensitive to the frequency offsets among UEs than the LFDMA system. If the

frequency offsets among UEs get larger, LFDMA has clearly an advantage over IFDMA.

4.5 Summary

In this chapter, we discussed the impairment of frequency offset on LTE system, including the downlink system and the uplink system. For downlink system, the signal model for the received signals was first derived. By comparing the signal models of HSPA+ system and that of LTE system, we figured out their similarity, and then a general model for the received signals of both HSPA+ system and LTE system was proposed. Therefore, the method for assessing error rate performance was unified for both HSPA+ system and LTE system.

Concerning the uplink system, it is a multiple access system and has a *Multipoint-to-Point* topology. Therefore, the discussion focused on the influence of user-specific frequency offset under different resource allocation schemes, i.e. LFDMA and IFDMA. The results reveal that the interference caused by user-specific frequency offset is distributed to all the received data symbols by the DFT process and the interference power is dispensed more uniformly over the received data symbols in the case of IFDMA, compared to LFDMA case. However, under the same user-specific frequency offset, the total interference power in an LFDMA system is remarkably smaller than that in an IFDMA system. Therefore, LFDMA scheme has clearly an advantage over IFDMA scheme when the frequency offsets among UEs get larger.

Chapter 5

Lower Bounds for Parameter Estimation from Observations of Pilot Signals

This chapter discusses the problem of estimating the parameters of pilot signals from a finite number of noisy discrete-time observations. The problem is of practical significance for commercial wireless communication systems.

In the wireless communication systems, pilot signals are usually introduced to help data-aided algorithms achieving reliable parameter estimations in order to ensure the system performance. To estimate the parameters of the pilot signal, such as the frequency, the phase and the amplitude, is an important part of the parameter estimation in the wireless communication systems. The analysis on the lower bounds for the parameter estimation can help us to optimize the design of the pilot signal and to establish a benchmark for assessing the performance of the estimator.

In this chapter, a general signal model for the observations of the pilot signal in an HSPA+ system and an LTE system is first summarized according to the derivations in the previous two chapters. Later, the lower bounds analysis based on the new signal model is conducted.

5.1 Signal Model of the Observations

The signal model with a single complex exponential under additive Gaussian noise is widely used in the literature for analyzing the observations of the pilot signal [*Huang and Letaief, 2006*][*Li et al., 2010*], which is represented as

$$r[n] = A e^{j(2\pi F n + \phi)} + w[n] \quad (5.1)$$

where A , F and ϕ represent the amplitude, the frequency normalized to the sampling frequency and the initial phase of the complex exponential, respectively. $w[n]$ denotes the zero-mean circular symmetric complex additive Gaussian noise with variance σ_w^2 . The CRBs for the parameter estimation based on Equation 5.1 were extensively discussed in the literature [*Rife and Boorstyn, 1974*][*Barbieri and Colavolpe, 2007*][*Li et al., 2010*].

However, according to our derivation, we find out that the traditional signal model in Equation 5.1 does not depict the observations of the pilot signal in both HSPA+ and LTE systems. To develop the

new signal model for our observations, we recall Equation 3.14 and Equation 4.22 as follows

$$\begin{aligned} \text{HSPA+: } \tilde{d}_P[i] &= \alpha_E e^{j\phi} \frac{\sin(\pi\Delta F W_P)}{W_P \sin(\pi\Delta F)} e^{j2\pi\Delta F(W_P-1)} e^{j2\pi W_P \Delta F i} d_P[i] + ICI_P[i] + \eta_E[i] \\ \text{LTE: } z_p[k_p] &= \frac{\sin(\pi\Delta F N_d)}{N_d \sin(\pi\Delta F)} e^{j\pi(N_d-1)\Delta F} e^{j2\pi\Delta F(pN_s+q_s)} H_E(k_p \Omega_c) a_{p,k_p} + ICI_p[k_p] + \varpi_p[k_p] \end{aligned}$$

where i and p in the equations denote the temporal index, respectively. When $\tilde{d}_P[i]$ and $z_p[k_p]$ are the observation of the pilot signals, the receiver should have prior knowledge of the pilot signals, i.e. $d_P[i]$ and a_{p,k_p} are known at the receivers. Therefore, by multiplying the observations with the conjugate of the pilot signals, we obtain

$$\hat{d}_P[i] = \alpha_E e^{j\phi} \frac{\sin(\pi\Delta F W_P)}{W_P \sin(\pi\Delta F)} e^{j2\pi\Delta F(W_P-1)} e^{j2\pi W_P \Delta F i} |d_P[i]|^2 + \widetilde{ICI}_P[i] + \tilde{\eta}_E[i] \quad (5.2a)$$

$$\hat{z}_p[k_p] = H_E(k_p \Omega_c) \frac{\sin(\pi\Delta F N_d)}{N_d \sin(\pi\Delta F)} e^{j\pi(N_d-1)\Delta F} e^{j2\pi\Delta F(pN_s+q_s)} |a_{p,k_p}|^2 + \widetilde{ICI}_p[k_p] + \tilde{\varpi}_p[k_p] \quad (5.2b)$$

The effective channels here are flat fading channels. Without loss of generality, we take the power of the pilot signals as 1, i.e. $|d_P[i]|^2 = |a_{p,k_p}|^2 = 1$. Assuming that the fading rate of the channel is much slower compared to the observation rate and the channel factors keep almost constant during the observation, Equation 5.2a and 5.2b can be rewritten as

$$\text{HSPA+: } \hat{d}[i] = \alpha_E e^{j\theta} \frac{\sin(\pi\Delta F W_P)}{W_P \sin(\pi\Delta F)} e^{j2\pi W_P \Delta F i} + \widetilde{ICI}[i] + \tilde{\eta}_E[i] \quad (5.3a)$$

$$\text{LTE: } \hat{z}[p] = \kappa_E e^{j\varphi} \frac{\sin(\pi\Delta F N_d)}{N_d \sin(\pi\Delta F)} e^{j2\pi N_s \Delta F p} + \widetilde{ICI}[p] + \tilde{\varpi}[p] \quad (5.3b)$$

where α_E and κ_E represent the amplitude of the effective channel factor, θ and φ are the combined phase factor which absorbs the phase of the effective channel and all the constant phase factors during observation, for instance, $\psi = \phi + 2\pi\Delta F(W_P - 1)$. The pilot channel index P in HSPA+ system and the pilot subcarrier index k_p in LTE system will not change during observation. Therefore, they are ignored in Equation 5.3a and 5.3b for simplicity. Meanwhile, the power of the pilot signal is assumed to be unit. Thus, the power of the interference and the noise in Equation 5.3a and 5.3b will keep the same as that in Equation 3.14 and 4.22. Since we have $\Delta F \ll 1$ in practical systems, we can approximate $\sin(\pi\Delta F)$ as $\pi\Delta F$. Thus, Equation 5.3a and 5.3b can be simplified to

$$\text{HSPA+: } \hat{d}[i] = \alpha_E e^{j\psi} \frac{\sin(\pi\Delta F W_P)}{\pi\Delta F W_P} e^{j2\pi W_P \Delta F i} + \widetilde{ICI}[i] + \tilde{\eta}_E[i] \quad (5.4a)$$

$$\text{LTE: } \hat{z}[p] = \kappa_E e^{j\varphi} \frac{\sin(\pi\Delta F N_d)}{\pi\Delta F N_d} e^{j2\pi N_s \Delta F p} + \widetilde{ICI}[p] + \tilde{\varpi}[p] \quad (5.4b)$$

So far, we can summarize the discrete observations of the pilot signals in HSPA+ system and LTE

system uniformly as

$$\begin{aligned} z[m] &= \alpha e^{j\theta} A(k\Omega) e^{j\Omega m} + ICI[m] + v[m] \\ &= \alpha e^{j\theta} A(k\Omega) e^{j\Omega m} + \chi[m] \end{aligned} \quad (5.5)$$

where Ω denotes the normalized angle frequency offset, which is defined as

$$\Omega = \begin{cases} 2\pi\Delta F W_P; & \text{HSPA+} \\ 2\pi\Delta F N_s; & \text{LTE} \end{cases} \quad (5.6)$$

$A(k\Omega)$ denotes amplitude attenuation caused by the frequency offset, which is defined as

$$A(k\Omega) = \frac{\sin \frac{k\Omega}{2}}{\frac{k\Omega}{2}} = \text{Sinc} \left(\frac{k\Omega}{2\pi} \right) \quad (5.7)$$

where k describes the bandwidth efficiency of the system and it is defined as

$$k = \begin{cases} 1; & \text{HSPA+} \\ \frac{N_d}{N_s}; & \text{LTE} \end{cases} \quad (5.8)$$

According to Equation 4.6, we have

$$\frac{N_d}{N_s} = \frac{T_d}{T_s} = \frac{T_d}{T_d + T_g} \quad (5.9)$$

Substituting the parameters of LTE system $T_d \approx 66.7 \mu\text{s}$ and $T_g \approx 5 \mu\text{s}$ into the equation, yields

$$k = \begin{cases} 1; & \text{HSPA+} \\ 0.93; & \text{LTE} \end{cases} \quad (5.10)$$

The interference term $ICI[m]$ in Equation 5.5 is assumed to have zero-mean circular symmetric complex Gaussian distribution. According Equations 3.26 and 4.28, we find out that the power of the interference in HSPA+ system and that in LTE system have also the same form. Combining Equations 4.30a, 4.30b and taking the average power of the data symbol as unit, the variance of the interference term can be expressed as

$$\sigma_{ICI}^2 = \alpha^2 \left[1 - \text{Sinc}^2 \left(\frac{k\Omega}{2\pi} \right) \right] = \alpha^2 [1 - A^2(k\Omega)] \quad (5.11)$$

The additive noise term $v[m]$ represents the result of the additive channel noise after despreading process in HSPA+ system or multi-carrier demodulation process in LTE system. The channel noise is here assumed to have zero-mean circular symmetric complex Gaussian distribution with variance σ_N^2 . Since $v[m]$ is the linear combination of the channel noise, it is also a zero-mean circular symmetric

complex Gaussian random variable. However, because of the difference between the despreading process in HSPA+ system and the demodulation process in LTE system, the variances of $v[m]$ in the two systems are

$$\sigma_v^2 = \begin{cases} \frac{\sigma_N^2}{W_P}; & \text{HSPA+} \\ \sigma_N^2; & \text{LTE} \end{cases} \quad (5.12)$$

where W_P is the spreading factor. Obviously, after the despreading process the additive noise power is reduced by the factor of W_P , which describes the spreading gain to the SNR by using CDMA technique. Since the interference term $ICI[m]$ and the noise term $v[m]$ are assumed to be mutually independent, the interference and noise term $\chi[m]$ is therefore a zero-mean circular symmetric complex Gaussian random variable too and its variance is the addition of the variance of the interference and that of the noise, i.e. $\sigma_\chi^2 = \sigma_v^2 + \alpha^2 [1 - A^2(k\Omega)]$.

5.2 Lower Bounds for Parameter Estimation

By this time, we have established a uniform signal model for HSPA+ system and LTE system and completely described the statistical properties of the observations $z[m]$. Compare Equation 5.5 to Equation 5.1, the amplitude of the single complex exponential in Equation 5.5 is frequency dependent, not like that in Equation 5.1, which is constant. The property of $A(k\Omega)$ affects the estimation performance. Therefore, the CRBs derived from Equation 5.1 in [Rife and Boorstyn, 1974] cannot be directly used here for Equation 5.5.

Intuitively, if $A(k\Omega) \approx 1$, the CRBs derived from Equation 5.1 should be very close to the CRBs based on Equation 5.5. However, according to Equation 5.7, $A(k\Omega) \approx 1$ implies $\Omega \approx 0$. That means, if the observations can be modeled by Equation 5.5, the CRBs from [Rife and Boorstyn, 1974] are only appropriate for the signal with frequency in a very small range around DC.

5.2.1 PDF and Likelihood Function of the Observations

If we have M observations and the unknown parameter vector is $\boldsymbol{\eta} = (\Omega, \theta, \alpha, \sigma_v^2)^T$, because $\chi[m]$ is circular symmetric complex Gaussian random variables, then the joint probability density function (pdf) of the observation vector \mathbf{z} is given by [Gallager, 2008b]

$$\begin{aligned} f(\mathbf{z}; \boldsymbol{\eta}) &= p(\boldsymbol{\chi}; \boldsymbol{\eta}) \\ &= \frac{1}{\pi^M \det(\mathbf{K}_\chi)} \exp(-\boldsymbol{\chi}^H \mathbf{K}_\chi^{-1} \boldsymbol{\chi}) \end{aligned} \quad (5.13)$$

where, \mathbf{K}_χ is the covariance matrix of the interference plus noise vector $\boldsymbol{\chi}$.

Since $\chi[m]$ are assumed to be independent and have zero-mean, from Equation 5.5 we obtain

$$\mu_{z[m]} = \alpha A(k\Omega) e^{j(\Omega m + \theta)} \quad (5.14)$$

$$\mathbf{K}_\chi = \sigma_\chi^2 \mathbf{I} = \left[\sigma_v^2 + \alpha^2 (1 - A^2(k\Omega)) \right] \mathbf{I} \quad (5.15)$$

where $\mu_{z[m]}$ is the mean value of $z[m]$ and \mathbf{I} denotes the identity matrix. Substituting Equation 5.15 to Equation 5.13, we obtain the pdf function as

$$f(\mathbf{z}; \boldsymbol{\eta}) = \frac{1}{(\pi\sigma_\chi^2)^M} \exp \left[-\frac{(z - \alpha A(k\Omega) e^{j\theta} \mathbf{p})^H (z - \alpha A(k\Omega) e^{j\theta} \mathbf{p})}{\sigma_\chi^2} \right] \quad (5.16)$$

where $\mathbf{p} = [1, e^{j\Omega}, \dots, e^{j(M-1)\Omega}]^T$ denotes the phase rotation vector.

Upon taking the natural logarithm of $f(\mathbf{z}; \boldsymbol{\eta})$, the Log-likelihood function can be expressed as

$$\begin{aligned} L(\boldsymbol{\eta}|\mathbf{z}) &= \ln f(\mathbf{z}; \boldsymbol{\eta}) \\ &= -\frac{\alpha^2 M}{\sigma_\chi^2} A^2(k\Omega) - M \ln \sigma_\chi^2 - \frac{1}{\sigma_\chi^2} \sum_{m=0}^{M-1} |z[m]|^2 - M \ln \pi + \\ &\quad \frac{1}{\sigma_\chi^2} \alpha A(k\Omega) e^{j\theta} \sum_{m=0}^{M-1} e^{j\Omega m} z^*[m] + \frac{1}{\sigma_\chi^2} \alpha A(k\Omega) e^{-j\theta} \sum_{m=0}^{M-1} e^{-j\Omega m} z[m] \\ &= -\frac{M}{\sigma_\chi^2} \alpha^2 A^2(k\Omega) + \frac{2}{\sigma_\chi^2} \alpha A(k\Omega) \Re \left[e^{-j\theta} \mathcal{Z}(\Omega) \right] - M \ln \sigma_\chi^2 - \frac{1}{\sigma_\chi^2} \mathcal{E} - M \ln \pi \end{aligned} \quad (5.17)$$

where $\Re[x]$ represents the real part of a complex value x , $\mathcal{Z}(\Omega) = \sum_{m=0}^{M-1} e^{-j\Omega m} z[m]$ is the Fourier transform of a finite discrete-time sequence [Oppenheim et al., 1999], $\mathcal{E} = \sum_{m=0}^{M-1} |z[m]|^2$ is a constant value representing the energy of the observations. According to Equation 5.14, we obtain the expectation of $\mathcal{Z}(\Omega)$ as

$$\begin{aligned} \mathbf{E} \{ \mathcal{Z}(\Omega) \} &= \sum_{m=0}^{M-1} e^{-j\Omega m} \mu_{z[m]} \\ &= M \alpha A(k\Omega) e^{j\theta} \end{aligned} \quad (5.18)$$

Recall Equation 5.6 here

$$\Omega = \begin{cases} 2\pi \Delta F W_P; & \text{HSPA+} \\ 2\pi \Delta F N_s; & \text{LTE} \end{cases}$$

where $\Delta F = \frac{\Delta f}{f_{\text{sampling}}}$. UE has a typical frequency stability tolerance of ± 10 ppm. Consider an oscillator for HSPA+ system or LTE system at 2 GHz, ± 10 ppm results in an offset of ± 20 kHz [Rupp et al., 2011]. Given $f_{\text{sampling}} = 3.84$ MHz and 30.72 MHz for HSPA+ system and LTE system, respectively,

ΔF for HSPA+ system and LTE system can achieve 5.21×10^{-3} and 6.51×10^{-4} , respectively. Because $W_p = 16$ for HSPA+ system and $N_s \approx 2200$ for LTE system, $|A(k\Omega)|$ will be 0.989 and 0.217, respectively. It means that $A(k\Omega)$ should not be simply approximated as unit to simplify the analysis.

5.2.2 Regularity of the PDF

Minimal performance bounds allow for calculation of the best performance that may be achieved, in the *Mean Square Error (MSE)* sense, when estimating a set of model parameters from noisy observations. Historically the first MSE lower bound for unbiased estimators of deterministic parameters was derived as Cramér-Rao Bound, which has been the most widely used since [*Chaumette et al., 2009*]. Its popularity is largely due to its simplicity of calculation leading to closed form expressions useful for system analysis and design. However, the probability density function of the observations should verify the regularity condition to obtain the CRBs.

Specifically, suppose $\mathbf{x} = (x_1, \dots, x_n)^T$ is the random observation vector with pdf $p(\mathbf{x}; \theta)$, where θ is a real parameter belonging to some parameter set \mathcal{S} . The following regularity condition is assumed to hold for the existence of the CRB:

$$\mathbb{E} \left[\frac{\partial \ln p(\mathbf{x}; \theta)}{\partial \theta} \right] = 0 \quad (5.19)$$

As described in [*Kay, 1993*], the regularity condition in Equation 5.19 will be satisfied if the order of differentiation and integration may be interchanged. This implies that the domain of the pdf for which it is nonzero should not depend on the unknown parameter.

When the regularity conditions are violated, the CRB cannot be applied to the problem and other approaches to construct the lower bounds must be used. D.G. Chapman and H. Robbins first discussed the minimum variance estimation without regularity assumptions. Later, the discussion was further extended by the works from Kiefer [*Kiefer, 1952*], Fraser and Guttman [*Fraser and Guttman, 1952*] and Blischke [*Blischke et al., 1969*].

To choose the appropriate tool to construct the lower bound for the unbiased estimator, we should first investigate whether the pdf of the observations could verify the regularity conditions. Checking the pdf expressed in Equation 5.16, it is obvious that the width of the pdf does depend on the parameter α, Ω , as shown in Figure 5.1, but it does not depend on θ .

In order to verify the regularity condition, substituting Equation 5.17 to the RHS of Equation 5.19 yields

$$\mathbb{E} \left[\frac{\partial \ln f(\mathbf{z}; \boldsymbol{\eta})}{\partial \Omega} \right] = \frac{4M\alpha A^3(k\Omega)A'(k\Omega)}{\sigma_x^4} \neq 0 \quad (5.20)$$

$$\mathbb{E} \left[\frac{\partial \ln f(\mathbf{z}; \boldsymbol{\eta})}{\partial \theta} \right] = 0 \quad (5.21)$$

$$\mathbb{E} \left[\frac{\partial \ln f(\mathbf{z}; \boldsymbol{\eta})}{\partial \alpha} \right] = 0 \quad (5.22)$$

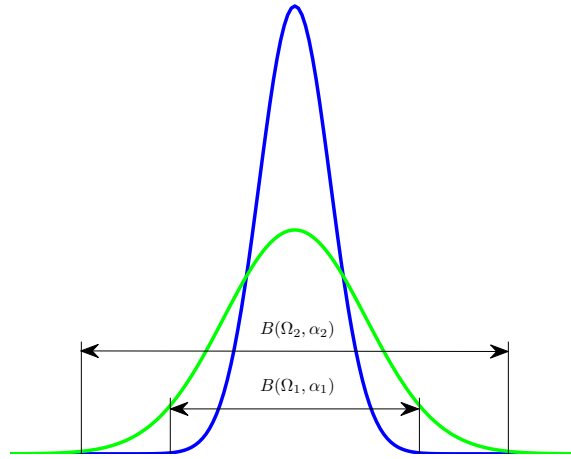


Figure 5.1: Non-regular PDF whose nonzero region depends on the unknown parameters

Therefore, usually, Equation 5.16 violates the regularity condition w.r.t Ω and the Cramér-Rao Bound for the unbiased estimator of frequency offset does not exist. However, we can still get Cramér-Rao Bound for estimating α or θ , if we assume that other parameters are known.

Another special case is that the interference is absent. The systems are assumed to be fully loaded for the derivations in the previous two chapters, i.e. all the HS-PDSCHs in an HSPA+ system or all the subcarriers in an LTE system are used to carry data symbols. However, in an extreme case, where only the pilot channel of the systems are active and all other resources are silent, χ consists of only the term ν , which is contributed by the channel noise, and the interference term is vanished. Consequently, the pdf becomes to verify the above regularity condition.

Next, we will first derivate the CRBs for the extreme case of without interference, and then analyze the lower bounds for the normal case.

5.2.3 Cramér-Rao Bounds when the interference is absent

If there is no interference, the Log-likelihood function in Equation 5.17 can be simplified to

$$\begin{aligned} L &= \frac{1}{\sigma_v^2} \alpha A(k\Omega) \left\{ -M\alpha A(k\Omega) + 2\Re \left[e^{-j\theta} \mathcal{Z}(\Omega) \right] \right\} - M \ln \sigma_v^2 - \frac{1}{\sigma_v^2} \mathcal{E} - M \ln \pi \\ &= \frac{1}{\sigma_v^2} \alpha A(k\Omega) \left\{ -M\alpha A(k\Omega) + 2\Re \left[e^{-j\theta} \mathcal{Z}(\Omega) \right] \right\} + C \end{aligned} \quad (5.23)$$

where $C = -M \ln \sigma_v^2 - \frac{1}{\sigma_v^2} \mathcal{E} - M \ln \pi$ is a constant.

The unbiased CRB are the diagonal element of the inverse of the Fisher information matrix \mathbf{J} [Kay,

1993], whose typical element is given by

$$J_{ij} = -\mathbf{E} \left\{ \frac{\partial^2 L}{\partial \eta_i \partial \eta_j} \right\} \quad (5.24)$$

The bounds are given by

$$\text{CRB}_{\eta_i} = \mathbf{J}^{ii} \quad (5.25)$$

where \mathbf{J}^{ii} is the i -th diagonal element of \mathbf{J}^{-1} .

When σ_v^2 is assumed to be known, the unknown parameter vector is degenerated to $\boldsymbol{\eta} = (\Omega, \theta, \alpha)^T$, then the derivatives are found as

$$\begin{aligned} \frac{\partial L}{\partial \Omega} &= \frac{1}{\sigma_v^2} \alpha A'(k\Omega) \left\{ -M\alpha A(k\Omega) + 2\Re \left[e^{-j\theta} \mathcal{Z}(\Omega) \right] \right\} \\ &\quad + \frac{1}{\sigma_v^2} \alpha A(k\Omega) \left\{ -M\alpha A'(k\Omega) + 2\Re \left[e^{-j\theta} \mathcal{Z}'(\Omega) \right] \right\} \\ \frac{\partial L}{\partial \theta} &= \frac{2}{\sigma_v^2} \alpha A(k\Omega) \Im \left[e^{-j\theta} \mathcal{Z}(\Omega) \right] \\ \frac{\partial L}{\partial \alpha} &= \frac{2M}{\sigma_v^2} \alpha A^2(k\Omega) + \frac{2}{\sigma_v^2} A(k\Omega) \Re \left[e^{-j\theta} \mathcal{Z}(\Omega) \right] \\ \frac{\partial^2 L}{\partial \Omega^2} &= \frac{1}{\sigma_v^2} \alpha A''(k\Omega) \left\{ -M\alpha A(k\Omega) + 2\Re \left[e^{-j\theta} \mathcal{Z}(\Omega) \right] \right\} \\ &\quad + \frac{2}{\sigma_v^2} \alpha A'(k\Omega) \left\{ -M\alpha A'(k\Omega) + 2\Re \left[e^{-j\theta} \mathcal{Z}'(\Omega) \right] \right\} \\ &\quad + \frac{1}{\sigma_v^2} \alpha A(k\Omega) \left\{ -M\alpha A''(k\Omega) + 2\Re \left[e^{-j\theta} \mathcal{Z}''(\Omega) \right] \right\} \\ \frac{\partial^2 L}{\partial \theta^2} &= -\frac{2}{\sigma_v^2} \alpha A(k\Omega) \Re \left[e^{-j\theta} \mathcal{Z}(\Omega) \right] \\ \frac{\partial^2 L}{\partial \alpha^2} &= -\frac{2M}{\sigma_v^2} A^2(k\Omega) \\ \frac{\partial^2 L}{\partial \Omega \partial \theta} &= \frac{2}{\sigma_v^2} \alpha A(k\Omega)' \Im \left[e^{-j\theta} \mathcal{Z}(\Omega) \right] + \frac{2}{\sigma_v^2} \alpha A(k\Omega) \Im \left[e^{-j\theta} \mathcal{Z}'(\Omega) \right] \\ \frac{\partial^2 L}{\partial \Omega \partial \alpha} &= -\frac{4M}{\sigma_v^2} \alpha A'(k\Omega) A(k\Omega) + \frac{2}{\sigma_v^2} A'(k\Omega) \Re \left[e^{-j\theta} \mathcal{Z}(\Omega) \right] \\ &\quad + \frac{2}{\sigma_v^2} A(k\Omega) \Re \left[e^{-j\theta} \mathcal{Z}'(\Omega) \right] \\ \frac{\partial^2 L}{\partial \theta \partial \alpha} &= \frac{2}{\sigma_v^2} A(k\Omega) \Im \left[e^{-j\theta} \mathcal{Z}(\Omega) \right] \\ \frac{\partial^2 L}{\partial \theta \partial \Omega} &= \frac{\partial^2 L}{\partial \Omega \partial \theta} \\ \frac{\partial^2 L}{\partial \alpha \partial \Omega} &= \frac{\partial^2 L}{\partial \Omega \partial \alpha} \\ \frac{\partial^2 L}{\partial \alpha \partial \theta} &= \frac{\partial^2 L}{\partial \theta \partial \alpha} \end{aligned}$$

where $\Im[x]$ represents the imaginary part of a complex value x , $A'(k\Omega)$ and $A''(k\Omega)$ are the first and second order derivative of $A(k\Omega)$, respectively.

Upon taking the expected value and using Equation 5.16 we have

$$\mathbf{E} \left\{ \Re \left[e^{-j\theta} \mathcal{Z}(\Omega) \right] \right\} = M\alpha A(k\Omega), \quad \mathbf{E} \left\{ \Re \left[e^{-j\theta} \mathcal{Z}'(\Omega) \right] \right\} = 0, \quad \mathbf{E} \left\{ \Re \left[e^{-j\theta} \mathcal{Z}''(\Omega) \right] \right\} = -\alpha Q A(k\Omega) \quad (5.26)$$

and

$$\mathbf{E} \left\{ \Im \left[e^{-j\theta} \mathcal{Z}(\Omega) \right] \right\} = 0, \quad \mathbf{E} \left\{ \Im \left[e^{-j\theta} \mathcal{Z}'(\Omega) \right] \right\} = \alpha P A(k\Omega) \quad (5.27)$$

where $P = \frac{M(M-1)}{2}$ and $Q = \frac{M(M-1)(2M-1)}{6}$.

Then, we obtain the Fisher information matrix as

$$\mathbf{J} = \begin{pmatrix} \frac{2\alpha^2}{\sigma_v^2} \left\{ M [A'(k\Omega)]^2 + Q A^2(k\Omega) \right\} & \frac{2\alpha^2}{\sigma_v^2} P A^2(k\Omega) & \frac{2\alpha M}{\sigma_v^2} A(k\Omega) A'(k\Omega) \\ \frac{2\alpha^2}{\sigma_v^2} P A^2(k\Omega) & \frac{2M}{\sigma_v^2} \alpha^2 A^2(k\Omega) & 0 \\ \frac{2\alpha M}{\sigma_v^2} A(k\Omega) A'(k\Omega) & 0 & \frac{2M}{\sigma_v^2} A^2(k\Omega) \end{pmatrix} \quad (5.28)$$

According to Equation 5.25, the CRBs are listed as follows

$$\text{CRB}_\Omega = \frac{6\sigma_v^2}{\alpha^2 A^2(k\Omega) M (M^2 - 1)} \quad (5.29)$$

$$\text{CRB}_\theta = \frac{\sigma_v^2}{\alpha^2 A^2(k\Omega)} \frac{2M - 1}{M (M + 1)} \quad (5.30)$$

$$\text{CRB}_\alpha = \frac{\sigma_v^2}{2M A^2(k\Omega)} \left[1 + \frac{12}{M^2 - 1} \left(\frac{A'(k\Omega)}{A(k\Omega)} \right)^2 \right] \quad (5.31)$$

5.2.4 Lower Bounds for the normal case

We have discussed the CRBs for the extreme case of without interference. However, it is more meaningful to analyze the system with high load, which will generate the interference, especially in the initial acquisition step of the receiving process.

It is concluded that the pdf is non-regular w.r.t. Ω when the interference is present. Therefore, the normal CRB for frequency offset estimation does not exist. To override the regularity condition, we take advantage of Barankin Bound [Barankin, 1949] and its approximations [Chaumette et al., 2008, 2009] to construct the lower bounds for unbiased estimators.

5.2.4.1 Barankin Bound and its approximations

Bhattacharyya's works [Bhattacharyya, 1947] first proved the initial characterization of locally unbiased estimators and refined the characterization of local unbiasedness, which is later significantly generalized by Barankin's works [Barankin, 1949]. Barankin established the general form of the greatest lower bound on MSE taking into account a uniform unbiasedness definition [Chaumette et al., 2009].

Taking the estimation of a single unknown real deterministic parameter μ for example, the random observation vector \mathbf{x} of dimension M in the observation space Ω has the pdf function $p(\mathbf{x}; \mu)$ depending on $\mu \in \mathcal{S}$, where \mathcal{S} denotes the parameter space. An unbiased estimator $T(\mathbf{x})$ of μ should be uniformly unbiased. Therefore, if μ_0 is a selected value of the parameter μ , the following expression holds

$$\int T(\mathbf{x})p(\mathbf{x}; \mu)d\mathbf{x} = \mu = \int T(\mathbf{x})\frac{p(\mathbf{x}; \mu)}{p(\mathbf{x}; \mu_0)}p(\mathbf{x}; \mu_0)d\mathbf{x} \quad (5.32)$$

To simplify the notation, Equation 5.32 can be represented as

$$E_{\mu} [T(\mathbf{x})] = \mu = E_{\mu_0} [T(\mathbf{x})R(\mathbf{x}; \mu)] \quad (5.33)$$

where $R(\mathbf{x}; \mu) = \frac{p(\mathbf{x}; \mu)}{p(\mathbf{x}; \mu_0)}$ denotes the *Likelihood Ratio (LR)*.

Let $L^2(\Omega)$ be the real Hilbert space of square integrable functions over Ω and the unbiased estimator $T(\mathbf{x})$ belongs to $L^2(\Omega)$. The MSE of $T(\mathbf{x})$ for μ_0 is defined to be a norm associated with a particular scalar inner product $\langle \cdot, \cdot \rangle_{\mu}$ of $L^2(\Omega)$ as

$$\begin{aligned} \text{MSE}_{\mu_0}[T(\mathbf{x})] &= \|T(\mathbf{x}) - \mu_0\|_{\mu_0}^2 \\ \langle \alpha(\mathbf{x}), \beta(\mathbf{x}) \rangle_{\mu_0} &= E_{\mu_0} [\alpha(\mathbf{x})^* \beta(\mathbf{x})] \end{aligned} \quad (5.34)$$

As a consequence, the *Locally (at μ_0) Minimum Variance Unbiased (LMVU)* estimator $T_{\mu_0}^{\text{LMVU}}(\mathbf{x})$ is the solution of a norm minimization under linear constraints, which can be expressed as:

$$T_{\mu_0}^{\text{LMVU}}(\mathbf{x}) = \underset{E_{\mu_0}[T(\mathbf{x})R(\mathbf{x}; \mu)] = \mu}{\text{argmin}} \text{MSE}_{\mu_0}[T(\mathbf{x})] \quad (5.35)$$

and the MSE of any unbiased estimator $T(\mathbf{x})$ in $L^2(\Omega)$ holds

$$\text{MSE}_{\mu_0}[T(\mathbf{x})] \geq \text{MSE}_{\mu_0} [T_{\mu_0}^{\text{LMVU}}(\mathbf{x})] \quad (5.36)$$

The solution of Equation 5.35 can be obtained by using the norm minimization lemma. However, as discussed in [Chaumette et al., 2008], if the parameter space \mathcal{S} contains a continuous subset of \mathbb{R} , the norm minimization under a set of an infinite number of linear constraints in Equation 5.33 leads to an integral equation with no analytical solution in general. Therefore, many studies [McAulay and Seidman, 1969][Abel, 1993][Todros and Tabrikian, 2008] have been dedicated to the derivation of "computable" lower bounds approximating the Barankin Bound $\text{MSE}_{\mu_0} [T_{\mu_0}^{\text{LMVU}}(\mathbf{x})]$. All these approximations are derived from sets of discrete or integral linear transform of Equation 5.33. They can be obtained by using the simple rationale in [Chaumette et al., 2009], which is repeated here as follows.

A. Barankin Bound approximations by linear transformations

Let $\boldsymbol{\mu}^N = (\mu_1, \dots, \mu_N)^T \in \mathcal{S}^N$ be a vector of N test points, $e(\mu_i) = \mu_i - \mu_0$ be the error value of μ_i to μ_0 and $\mathbf{e}(\boldsymbol{\mu}^N) = [e(\mu_1), \dots, e(\mu_N)]^T$ be the error vector associated to the test points, $\mathbf{R}(\mathbf{x}; \boldsymbol{\mu}^N) =$

$[R(\mathbf{x}; \boldsymbol{\mu}^1), \dots, R(\mathbf{x}; \boldsymbol{\mu}^N)]^T$ be the vector of LR associated to $\boldsymbol{\mu}^N$. Any unbiased estimator $T(\mathbf{x})$ verifying Equation 5.33 must comply with

$$E_{\mu_0} [(T(\mathbf{x}) - \mu_0) \mathbf{R}(\mathbf{x}; \boldsymbol{\mu}^T)] = \mathbf{e}(\boldsymbol{\mu}^N) \quad (5.37)$$

and with any subsequent linear transformation of Equation 5.37. Suppose $\mathbf{h}_k \in \mathbb{R}^N$, $k \in [1, K]$ represents any set of K ($K \leq N$) independent linear transformation. Then, the linear transformation of Equation 5.37 expressed as

$$E_{\mu_0} [(T(\mathbf{x}) - \mu_0) \mathbf{h}_k^T \mathbf{R}(\mathbf{x}; \boldsymbol{\mu}^T)] = \mathbf{h}_k^T \mathbf{e}(\boldsymbol{\mu}^N) \quad (5.38)$$

provides with a lower bound on the MSE as

$$\text{MSE}_{\mu_0}[T(\mathbf{x})] \geq \mathbf{e}^T(\boldsymbol{\mu}^N) \mathbf{G}_{\mathbf{H}_K} \mathbf{e}(\boldsymbol{\mu}^N) \quad (5.39)$$

where $\mathbf{G}_{\mathbf{H}_K} = \mathbf{H}_K (\mathbf{H}_K^T \mathbf{C}_R \mathbf{H}_K)^{-1} \mathbf{H}_K^T$, $\mathbf{H}_K = [\mathbf{h}_1, \dots, \mathbf{h}_K]$ and $[\mathbf{C}_R]_{n,m} = E_{\mu_0} [R(\mathbf{x}; \mu_n) R(\mathbf{x}; \mu_m)]$.

The Barankin Bound is obtained by taking the supremum of Equation 5.39 over all the existing degrees of freedom $(N, \boldsymbol{\mu}^N, K, \mathbf{H}_K)$. Moreover, for a given vector of testing points $\boldsymbol{\mu}^N$, the lower bound reaches its maximum iff the matrix \mathbf{H}_K is invertible ($K = N$) [McAulay and Seidman, 1969], which represents a bijective transformation of the set of the N initial constraints as

$$\text{MSE}_{\mu_0}[T(\mathbf{x})] \geq \mathbf{e}^T(\boldsymbol{\mu}^N) \mathbf{G}_{\mathbf{I}_N} \mathbf{e}(\boldsymbol{\mu}^N) \geq \mathbf{e}^T(\boldsymbol{\mu}^N) \mathbf{G}_{\mathbf{H}_K} \mathbf{e}(\boldsymbol{\mu}^N) \quad (5.40)$$

where \mathbf{I}_N denotes the identity matrix with dimension N .

B. Barankin Bound approximations by non-linear transformations

A non-linear transformation of the unbiasedness definition in Equation 5.33 is defined as

$$E_{\mu_0} [T(\mathbf{x}) t(R(\mathbf{x}; \boldsymbol{\mu}))] = h(\boldsymbol{\mu}) \quad (5.41)$$

Although it seems a difficult mathematical task to obtain the result from Equation 5.41, there is a class of estimation problems where non-linear transformation of the LR can be used to derive new lower bounds on the MSE. If the pdf of the observation vector $p(\mathbf{x}; \boldsymbol{\mu})$ exists at least one real valued function $t(\cdot)$ which fulfills

$$t(p(\mathbf{x}; \boldsymbol{\mu})) = k(\boldsymbol{\mu}, t) \tilde{p}(\mathbf{x}; \boldsymbol{\gamma}(\boldsymbol{\mu}, t)); \quad k(\boldsymbol{\mu}, t) = \int_{\mathcal{S}} t(p(\mathbf{x}; \boldsymbol{\mu})) d\mathbf{x} \quad (5.42)$$

where $k(\boldsymbol{\mu}, t)$ is a constant w.r.t. the observation vector \mathbf{x} , $\boldsymbol{\gamma}(\boldsymbol{\mu}, t)$ denotes the modified parameter value associated to the transformation $t(\cdot)$ and $\tilde{p}(\mathbf{x}; \boldsymbol{\gamma}(\boldsymbol{\mu}, t))$ fulfills the requirements of a probability density function, then the results from the above discussed approximations by linear transformation still holds

through the modifications:

$$R(\mathbf{x}; \mu) = \frac{t_\mu(\mathbf{x}; \mu)}{p(\mathbf{x}; \mu_0)}, \quad e(\mu) = k(\mu, t_\mu) [\gamma(\mu, t_\mu) - \mu_0] \quad (5.43)$$

5.2.4.2 Barankin Bound approximation for our signal model

We have derived the pdf of our observations in Equation 5.16 and now recall it here:

$$f(\mathbf{z}; \boldsymbol{\eta}) = \frac{1}{(\pi\sigma_\chi^2)^M} \exp \left[-\frac{(\mathbf{z} - \alpha A(k\Omega)\mathbf{e}^{j\theta}\mathbf{p})^H (\mathbf{z} - \alpha A(k\Omega)\mathbf{e}^{j\theta}\mathbf{p})}{\sigma_\chi^2} \right]$$

Taking the transformation $t_q(y) = y^q$ on the pdf, yields

$$\begin{aligned} t_q[f(\mathbf{z}; \boldsymbol{\eta})] &= \frac{1}{(\pi\sigma_\chi^2)^{qM}} \exp \left[-\frac{(\mathbf{z} - \alpha A(k\Omega)\mathbf{e}^{j\theta}\mathbf{p})^H (\mathbf{z} - \alpha A(k\Omega)\mathbf{e}^{j\theta}\mathbf{p})}{\frac{\sigma_\chi^2}{q}} \right] \\ &= \frac{\pi(1-q)^M}{q^{qM}} \left(\frac{\sigma_\chi^2}{q} \right)^{(1-q)M} \frac{1}{\left(\pi \frac{\sigma_\chi^2}{q} \right)^M} \exp \left[-\frac{(\mathbf{z} - \alpha A(k\Omega)\mathbf{e}^{j\theta}\mathbf{p})^H (\mathbf{z} - \alpha A(k\Omega)\mathbf{e}^{j\theta}\mathbf{p})}{\frac{\sigma_\chi^2}{q}} \right] \\ &= k(\boldsymbol{\eta}, q) p(\mathbf{z}; \gamma(\boldsymbol{\eta}, q)) \end{aligned} \quad (5.44)$$

where the constant term w.r.t. \mathbf{x} is expressed as

$$k(\boldsymbol{\eta}, q) = \frac{1}{q^M} (\pi\sigma_\chi^2)^{(1-q)M} \quad (5.45)$$

and the new pdf is expressed as

$$p(\mathbf{z}; \gamma(\boldsymbol{\eta}, q)) = \frac{1}{\left(\pi \frac{\sigma_\chi^2}{q} \right)^M} \exp \left[-\frac{(\mathbf{z} - \alpha A(k\Omega)\mathbf{e}^{j\theta}\mathbf{p})^H (\mathbf{z} - \alpha A(k\Omega)\mathbf{e}^{j\theta}\mathbf{p})}{\frac{\sigma_\chi^2}{q}} \right], \quad (5.46)$$

which describes an M -dimension circular symmetric Gaussian random vector with a covariance matrix $\mathbf{K} = \frac{\sigma_\chi^2}{q} \mathbf{I}$. It is worth noticing that the expressions of the unknown parameters do not change after the transformation, i.e. $\gamma(\boldsymbol{\eta}, q) = \boldsymbol{\eta} = (\Omega, \theta, \alpha)^T$.

It is obvious that the non-linear transformation $t_q(y) = y^q$ of our signal model complies with the requirements in Equation 5.42. Therefore, after replacing $R(\mathbf{x}; \mu)$ and $e(\mu)$ in Equation 5.40 with Equation 5.43, we can use the results obtained from linear transformation.

Let us now consider the simplest approximation of Barankin Bound for the frequency Ω based on 2 test-points $\boldsymbol{\Omega}^2 = (\Omega_1, \Omega_2)^T = (\Omega + h, \Omega - h)^T$ where $\mathbf{H}_2 = \mathbf{I}_2$. According to Equation 5.40 and

Equation 5.43, we define the lower bound as

$$\begin{aligned}
BB_{\Omega} &= \sup_{h,q} \left\{ \mathbf{e}^T(\Omega^2) \mathbf{G}_{I_N} \mathbf{e}(\Omega^2) \right\} \\
&= \sup_{h,q} \left\{ \begin{bmatrix} h k(\Omega_1, q) \\ -h k(\Omega_2, q) \end{bmatrix}^T \mathbb{E}_{\Omega} \left[\begin{pmatrix} \frac{k(\Omega_1, q)p(\mathbf{z}; \Omega_1)}{f(\mathbf{z}; \Omega)} \\ \frac{k(\Omega_2, q)p(\mathbf{z}; \Omega_2)}{f(\mathbf{z}; \Omega)} \end{pmatrix} \begin{pmatrix} \frac{k(\Omega_1, q)p(\mathbf{z}; \Omega_1)}{k(\Omega_2, q)p(\mathbf{z}; \Omega_2)} \\ \frac{f(\mathbf{z}; \Omega)}{f(\mathbf{z}; \Omega)} \end{pmatrix}^T \right]^{-1} \begin{bmatrix} h k(\Omega_1, q) \\ -h k(\Omega_2, q) \end{bmatrix} \right\} \quad (5.47)
\end{aligned}$$

By using the results in Appendix G, we further obtain

$$\begin{aligned}
BB_{\Omega} &= \sup_{h,q} \left\{ \begin{bmatrix} h k(\Omega_1, q) \\ -h k(\Omega_2, q) \end{bmatrix}^T \begin{bmatrix} k^{11}(q)\tilde{\mathbf{G}}_{1,1}^z & k^{12}(q)\tilde{\mathbf{G}}_{1,2}^z \\ k^{21}(q)\tilde{\mathbf{G}}_{2,1}^z & k^{22}(q)\tilde{\mathbf{G}}_{2,2}^z \end{bmatrix}^{-1} \begin{bmatrix} h k(\Omega_1, q) \\ -h k(\Omega_2, q) \end{bmatrix} \right\} \\
&= \sup_{h,q} \left\{ \frac{h^2 \left[k^{11}(q)k^{22}(q)\tilde{\mathbf{G}}_{1,1}^z + k^{12}(q)k^{12}(q)\tilde{\mathbf{G}}_{1,2}^z + k^{21}(q)k^{21}(q)\tilde{\mathbf{G}}_{2,1}^z + k^{11}(q)k^{22}(q)\tilde{\mathbf{G}}_{2,2}^z \right]}{k^{11}(q)k^{22}(q)\tilde{\mathbf{G}}_{1,1}^z\tilde{\mathbf{G}}_{2,2}^z - k^{21}(q)k^{12}(q)\tilde{\mathbf{G}}_{1,2}^z\tilde{\mathbf{G}}_{2,1}^z} \right\} \\
&= \sup_{h,q} \left\{ \frac{h^2 \left(\tilde{\mathbf{G}}_{1,1}^z + 2\tilde{\mathbf{G}}_{1,2}^z + \tilde{\mathbf{G}}_{2,2}^z \right)}{\tilde{\mathbf{G}}_{1,1}^z\tilde{\mathbf{G}}_{2,2}^z - \left(\tilde{\mathbf{G}}_{1,2}^z \right)^2} \right\} \quad (5.48)
\end{aligned}$$

where

$$\tilde{\mathbf{G}}_{i,j}^z = \left[\frac{\sigma_z^2(\Omega)c_z^{ij}}{q\sigma_z^2(\Omega_i)\sigma_z^2(\Omega_j)} \right]^M \exp \left(c_z^{ij} \|\tilde{\mathbf{m}}_z^{ij}\|^2 - \tilde{\delta}_z^{ij} \right) \quad (5.49a)$$

$$c_z^{ij} = \left[\frac{1}{\sigma_z^2(\Omega_i)} + \frac{1}{\sigma_z^2(\Omega_j)} - \frac{1}{q\sigma_z^2(\Omega)} \right]^{-1} \quad (5.49b)$$

$$\tilde{\mathbf{m}}_z^{ij} = \frac{\mathbf{m}_z(\Omega_i)}{\sigma_z^2(\Omega_i)} + \frac{\mathbf{m}_z(\Omega_j)}{\sigma_z^2(\Omega_j)} - \frac{\mathbf{m}_z(\Omega)}{q\sigma_z^2(\Omega)} \quad (5.49c)$$

$$\tilde{\delta}_z^{ij} = \frac{\|\mathbf{m}_z(\Omega_i)\|^2}{\sigma_z^2(\Omega_i)} + \frac{\|\mathbf{m}_z(\Omega_j)\|^2}{\sigma_z^2(\Omega_j)} - \frac{\|\mathbf{m}_z(\Omega)\|^2}{q\sigma_z^2(\Omega)} \quad (5.49d)$$

$$\mathbf{m}_z(\Omega_i) = \alpha A(k\Omega_i) e^{j\theta} \mathbf{p}_{\Omega_i}, \quad \sigma_z^2(\Omega_i) = \sigma_{\chi}^2(\Omega_i) = \sigma_v^2 + \alpha^2 \left[1 - A^2(k\Omega_i) \right] \quad (5.49e)$$

Although the non-linear approximation is adopted here, it is obvious that the linear approximation is just a special case of taking $q = 1$ to the result from the non-linear approximation.

5.3 Properties of the Barakin bound for frequency estimation

We have derived the lower bounds for parameter estimation, especially for frequency estimation, based on the signal model in Equation 5.5, which depicts the more general case in practical HSPA+ system and LTE system. Although the derivation of lower bounds cannot provide us the estimator which can achieve the bounds, the properties of the lower bounds can indeed direct us to choose

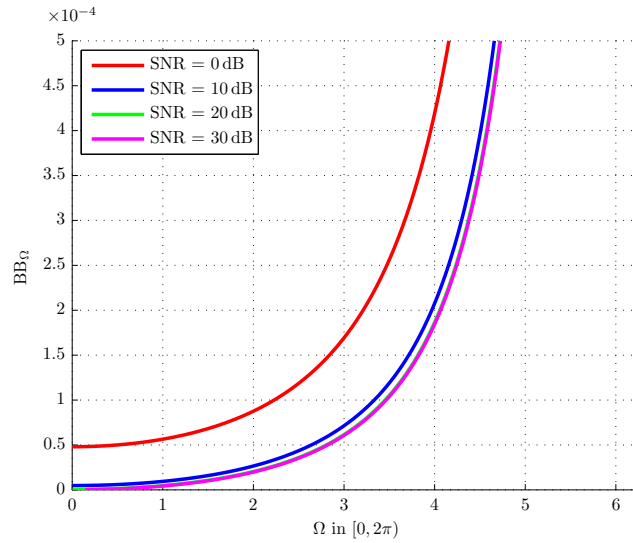


Figure 5.2: BB_{Ω} w.r.t. Ω at $\alpha = 1$, $k = 1$, $q = 1$, $M = 32$

better strategies for conducting parameter estimation.

Later, we focus on frequency estimation. Without loss generality, $\alpha = 1$, $q = 1$, $k = 1$ are given for the further discussion.

The curves in Figure 5.2 depict the BB_{Ω} over Ω for different receive SNRs by the estimator. As expected, the estimation variance becomes smaller when the receive SNR is increased. However, increasing receive SNR over 20 dB seems not bring much improvement to the BB_{Ω} any more. Furthermore, it is shown that BB_{Ω} is a monotonic increasing function of Ω and it grows much more rapidly after Ω is larger than $\frac{\pi}{2}$. It implies that the estimated frequency Ω should be kept in a relatively small range for the unbiased estimator to achieve more accurate estimation.

Duo to the nonlinear nature of the frequency estimation problem, the so-called threshold effect [Rife and Boorstyn, 1974][James et al., 1995] exists whenever the SNR drops below a critical data-length dependent level $SNR(M)$. For estimating the frequency of a sinusoid only in additive Gaussian noise, the threshold effect can be characterized by an almost instant and drastic deterioration of the frequency estimator variance with respect to the CRB below this critical SNR level [Knockaert, 1997]. Therefore, all SNR above the threshold can be considered to be "high SNR", oppositely, the SNR below the threshold belongs to "low SNR" region.

However, our signal model considers not only the additive Gaussian noise, but also the interference caused by the frequency offset. We compare the BB_{Ω} w.r.t. SNR for different signal models in Figure 5.3. The dashed curve is the result of the traditional signal model considering only the additive Gaussian noise and the solid curve is obtained from the signal model taking care of both additive Gaussian noise and the interference. It is clear that the NDR for the new model corresponds to the low SNR region of the traditional model. It is interesting to note that BB_{Ω} of our model will go to a performance floor with the SNR increasing over 20 dB, just as we conclude previously from Figure 5.2. We know that the interference power is relevant to the frequency offset and independent of the additive

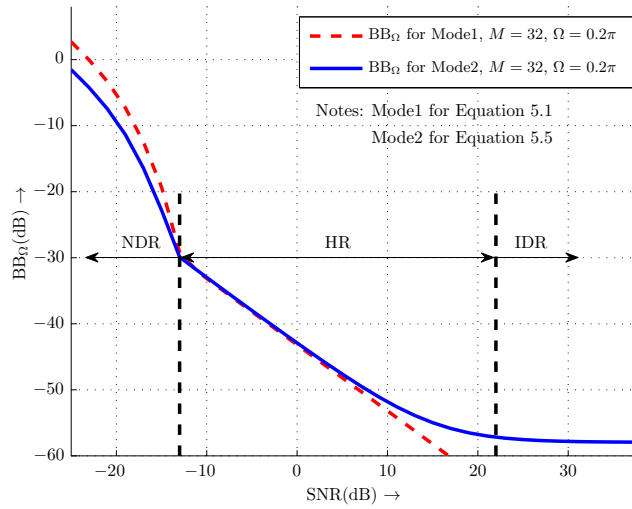


Figure 5.3: BB_{Ω} w.r.t. SNR for different signal models

Gaussian noise. For a given frequency offset, the interference power can be seen as invariant. Then, with the decreasing of the strength of the additive Gaussian noise, the interference becomes gradually the dominant part of the undesired signal and it causes the variance floor. Therefore, as shown in the figure, the SNR region can be generally divided into three parts: *Noise Dominant Region (NDR)*, *Interference Dominant Region (IDR)* and *Hybrid Region (HR)* in which the additive Gaussian noise and the interference have similar significance and none of them can be ignored.

On the other hand, Equation 5.49a implies that the number of observations M will influence the accuracy of the estimation. The effect of different M is drawn in Figure 5.4(a). As expected, the bound is inversely proportional to M . Of course, the performance improvement is achieved at the cost of the computation complexity. It is interesting to note that BB_{Ω} gains 9 dB lower when M is doubled. Consequently, BB_{Ω} can direct us to trade computation complexity for the required estimation accuracy, which can be obtained based on the analysis in Chapter 3 and Chapter 4. Meanwhile, Figure 5.2 already tells us that BB_{Ω} is dependent on Ω . The curves in Figure 5.4(b) shows us BB_{Ω} w.r.t. SNR for different Ω by taking $M = 32$. It is obvious that the smaller Ω , the smaller estimation variance.

We will further combine the analysis for BB_{Ω} and the simulation result in Chapter 3 to select the parameters for constructing the frequency offset estimator in HSPA+ system and LTE system.

5.4 Parameter selection for frequency estimation

In Chapter 4 we have unified the analysis of the symbol error rate w.r.t. the frequency offset in HSPA+ system and in LTE system with the help of introducing the normalized frequency offset $\Delta\mathcal{F}$ and the results were shown in Figure 4.2.

Meanwhile, Equation 5.5 also abstracted and unified the signal model of the observations for frequency offset estimation in HSPA+ system and in LTE system. Therefore, the analysis here fits to

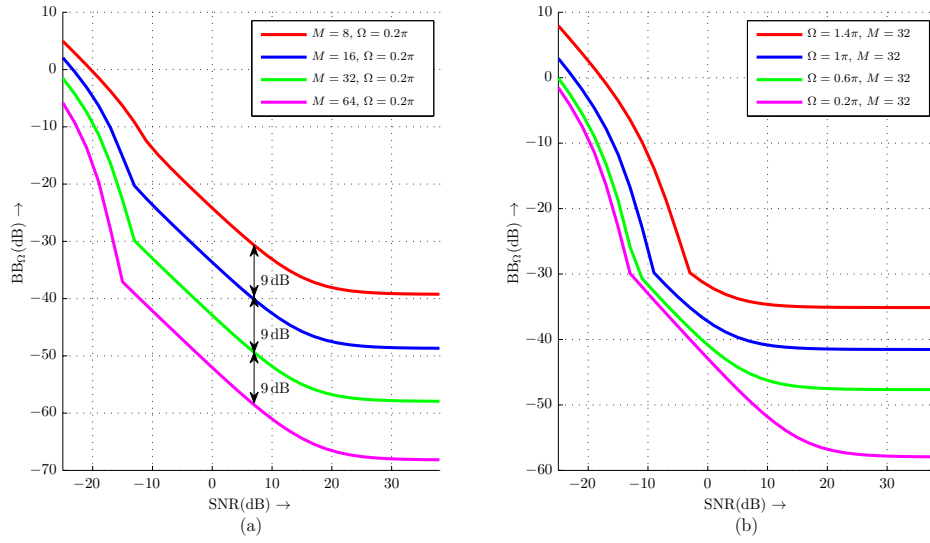


Figure 5.4: BB_{Ω} w.r.t. SNR for different M and Ω

both HSPA+ system and LTE system.

Combining Equation 3.71, 4.32, 5.6, and 5.8, yields

$$\Delta\mathcal{F} = \frac{k\Omega}{2\pi} \quad (5.50)$$

In HSPA+ system and LTE system, the frequency offset between the transmitter and the receiver will be first estimated and compensated before demodulation. If we attempt to reduce the performance loss of symbol error rate P_M caused by the frequency error to a negligible level after frequency offset correction, the error of frequency offset estimation should of course be limited in a corresponding level. According to the simulation results shown in Figure 4.2, if the target P_M is 10^{-2} , the frequency estimation error for $\Delta\mathcal{F}$ should be smaller as 8.33×10^{-4} , and if setting 10^{-3} as target P_M , the corresponding frequency estimation error should be upper bounded by 2.08×10^{-4} . We express it in a formula as

$$\text{RMSE}(\Delta\mathcal{F}) \leq \begin{cases} 8.33 \times 10^{-4}, & \text{target } P_M = 10^{-2} \\ 2.08 \times 10^{-4}, & \text{target } P_M = 10^{-3} \end{cases} \quad (5.51)$$

where $\text{RMSE}(\cdot)$ denotes taking *Root Mean Square Error* value [Schonhoff and Giordano, 2006].

Based on Equation 5.50 and taking $k \approx 1$, it is obtained that

$$\text{RMSE}(\Omega) = 2\pi \text{RMSE}(\Delta\mathcal{F}) \leq \begin{cases} 5.23 \times 10^{-3}, & \text{target } P_M = 10^{-2} \\ 1.31 \times 10^{-3}, & \text{target } P_M = 10^{-3} \end{cases} \quad (5.52)$$

Consequently, we get the required bound for frequency estimation variance as

$$\text{Var}(\Omega) = [\text{RMSE}(\Omega)]^2 \leq \begin{cases} 2.74 \times 10^{-5} \approx -46 \text{ dB}, & \text{target } P_M = 10^{-2} \\ 1.72 \times 10^{-6} \approx -58 \text{ dB}, & \text{target } P_M = 10^{-3} \end{cases} \quad (5.53)$$

Considering to limit computation complexity and keep timeliness of the estimation, we limit the observation length $M \leq 64$. By comparing the results to the curves in Figure 5.4, there are two choices for target P_M at 10^{-2} : $\Omega \leq 0.2\pi$, $M = 16$ or $\Omega \leq 0.6\pi$, $M = 32$. For target P_M at 10^{-3} , we have only one choice: $\Omega \leq 0.2\pi$, $M = 32$. Converting Ω to $\Delta\mathcal{F}$, yields

$$\begin{cases} \text{target } P_M = 10^{-2} : & \Delta\mathcal{F} \leq 0.1, M = 16 \text{ or } \Delta\mathcal{F} \leq 0.3, M = 32 \\ \text{target } P_M = 10^{-3} : & \Delta\mathcal{F} \leq 0.1, M = 32 \end{cases} \quad (5.54)$$

5.5 Summary

In this chapter, we made effort to establish a performance benchmark for unbiased frequency estimators for both HSPA+ system and LTE system. The CRB is widely adopted in literature for this purpose. However, it only exists when the pdf of the observations obeys the regularity conditions. Unfortunately, based on the general signal model proposed in chapter 4, we get to know that, the pdf of the observations for frequency estimation in HSPA+ system and in LTE system violates those regularity conditions and the CRB is not available. Therefore, we resort to the Barankin Bound, which is broadly used to overcome the requirement of regularity conditions. Although it is not tractable to calculate the Barankin Bound, its approximation is derived and the simulation results establish the performance benchmark for the frequency estimation, which help us to design appropriate parameters for frequency synchronizer in the real systems.

Chapter 6

Implementation of Frequency Synchronization in HSPA+ System and LTE System

Coherent receiving is usually adopted in the high speed digital communication system for higher spectral and power efficiency and better error-rate performance. That is to say, timing and frequency synchronization should be achieved first before demodulation can be conducted.

Concerning the baseband receiver, because each system has its specified frame structure to burden the signaling and the payload, to achieve timing synchronization for the desired system, such as the slot boundary and the frame boundary, is usually the first step of receiving process.

From synchronization point of view, current cellular mobile communication systems can be classified to *Synchronized* network and *Asynchronous* network. In a synchronized network, all of the base stations use the same timing over the air interface, whereas in an asynchronous network, a base station's air interface timing could differ from its neighbor's. The boundary information as mentioned before is normally embedded in synchronization channels of the systems. Auto-correlation and cross-correlation are the two normal methods to obtain the timing information.

HSPA+ system is an asynchronous wideband DSSS CDMA system. For coherent receiving in HSPA+ system, the parameters of scrambling code number, frame or slot timing, frequency offset and channel state information are all required. *Initial Acquisition* process is one part of cell search procedure and consists of *scramble code searching*, *timing acquisition* and *frequency acquisition* [Wang and Ottosson, 2000]. For a sizeable frequency offset, as described in [Meyr et al., 1997], frequency acquisition process should firstly estimate and compensate this frequency offset, before the other parameters can be estimated. The similar requirement is also desired for LTE technology, which operates in both synchronized and asynchronous networks. This implies that frequency acquisition algorithm must work independently of the values of the other parameters in HSPA+ system or LTE system.

Mass produced consumer electronics commonly use inexpensive and rather inaccurate crystal oscillators. Such crystal oscillators have inaccuracies in the range of 3–13 ppm, giving rise to a frequency error in the range of 6–26 kHz, when operated at 2 GHz. Such a frequency error, if not corrected, results in severe degradation in receiver performance so that the receiver communication functions

fail [Wang and Ottosson, 2000]. The performance loss caused by the frequency offset in HSPA+ system and LTE system has been discussed in Chapter 3 and Chapter 4. In Chapter 5 the unified signal model for pilot signal in HSPA+ system and LTE system is introduced and the lower bound for frequency estimation based on it is derived. In this chapter we first compare the performance of different frequency estimation methods and later introduce the fast frequency acquisition algorithms in both systems.

6.1 Frequency Synchronization Strategy

Frequency synchronization aims to first estimate the frequency offset embedded in the received signal and then compensate it in order to yield a target error-rate degradation (which should not exceed about 0.2 dB compared to the performance under the assumption of perfect synchronization)[Meyr et al., 1997].

Frequency synchronization procedures can usually be classified to *Frequency Acquisition* and *Frequency Tracking*. Frequency acquisition and frequency tracking have different working condition. At the start of signal reception, the synchronizer has no knowledge about the synchronization parameter values. After some processing of the received signal, the synchronizer is able to deliver accurate estimates of the synchronization parameters that are needed for reliable data detection. This transition from a large initial uncertainty about the synchronization parameters to a small steady-state estimation error variance is called *Acquisition* [Meyr et al., 1997]. After frequency acquisition, the frequency offset is reduced to a much smaller range and the synchronizer is switched to tracking mode, which takes care of small frequency offset usually caused by the steady-state estimation error, slow oscillator drift or Doppler shifts.

According to Figure 5.4(b) in Chapter 5, for a given algorithm complexity, the smaller operation range for the frequency offset yields the better variance performance. Therefore, the performance degradation requirement may call for a small range of frequency offset. This may entail an extremely narrow acquisition range which, on the contrary, should be large enough to accommodate the maximum *a priori* uncertainty on the carrier frequency due to the instability of oscillators and/or to a Doppler shift. Furthermore, frequency acquisition is one part of initial acquisition procedure. The system requirement of switch-on delay limits the time consume of frequency acquisition process, which also bounds the number of observations used for estimation and the complexity of the algorithm.

To ensure correct operation of the frequency recovery algorithm both in the acquisition and in the tracking mode, a two-step approach can be pursued [Luise and Reggiannini, 1996]. Specially, the number of observation M and the algorithm are initially chosen to provide an adequate lock-in range for frequency acquisition. Once a frequency estimate has been obtained in the frequency acquisition stage, coarse frequency correction takes places, and the algorithm switches to tracking mode, whereby the number of observation M and the algorithm are changed so as to bring the steady-state estimation error down to a level ensuring a specified performance degradation.

6.2 Performance Comparison of Frequency Estimation Algorithms

For both frequency acquisition and frequency tracking we should select an appropriate algorithm to build up the frequency estimator. Frequency estimation based on the signal model in Equation 5.1 has long been discussed in literature. The *Maximum Likelihood Estimator (MLE)* is derived in [Rife and Boorstyn, 1974]. Periodogram algorithm and its several variants have also been studied in [So et al., 1999]. *Least-squares (LS)* approaches have been discussed in [Besson and Stoica, 1995] and [Besson and Stoica, 1998].

It is straightforward that the signal model in Equation 5.1 fulfills the regularity conditions, which have been listed in Chapter 5. Therefore, the MLE based on it is consistent, asymptotically normal and asymptotically efficient [Kutoyants, 2008]. Furthermore, the standard Periodogram Estimator and the LS Estimator are both equivalent to the MLE for the signal model in Equation 5.1.

However, if the self interference caused by the frequency offset is not ignored in HSPA+ system and LTE system, the signal model of the observations in both systems is unified to Equation 5.5, which has also been proved to be non-regular in Chapter 5. Then, the periodogram estimator and also the LS estimator are not equivalent to the MLE any more. Besides, the asymptotic properties of the MLE of finite dimensional parameters of any statistical model depend strongly on the regularity conditions [Kutoyants, 2008]. From estimation performance point of view, the MLE is not necessarily the best choice in non-regular cases. Therefore, we first assess the performance of different estimation approaches for signal model in Equation 5.5 and select an appropriate one to build up our frequency synchronizer.

A. Maximum Likelihood Estimator(MLE)

Recall the Log-likelihood function in Equation 5.17

$$L(\boldsymbol{\eta}|z) = \frac{2}{\sigma_x^2} \alpha A(k\Omega) \Re \left[e^{-j\theta} \mathcal{Z}(\Omega) \right] - \frac{1}{\sigma_x^2} M \alpha^2 A^2(k\Omega) - M \ln \sigma_x^2 - \frac{1}{\sigma_x^2} \mathcal{E} - M \ln \pi$$

where $\boldsymbol{\eta} = (\Omega, \theta, \alpha)^T$. The ML estimate of $\boldsymbol{\eta}$ is the value of $\boldsymbol{\eta}$, say $\hat{\boldsymbol{\eta}}$, that maximizes $L(\boldsymbol{\eta}|z)$ when z is the observation vector, i.e.

$$\hat{\boldsymbol{\eta}} = (\hat{\Omega}, \hat{\theta}, \hat{\alpha})^T = \underset{\Omega, \theta, \alpha}{\operatorname{argmax}} L(\boldsymbol{\eta}|z) \quad (6.1)$$

Now suppose all three parameters are unknown and $\alpha > 0$. It is easy to show that L is maximized over θ , for a fixed Ω , if $\theta = \arg[\mathcal{Z}(\Omega)]$, where $\arg[\cdot]$ means the operation of taking the phase of a complex value. Then we obtain

$$\hat{\Omega}_{\text{MLE}} = \underset{\Omega}{\operatorname{argmax}} \left\{ \frac{2}{\sigma_x^2} \alpha A(k\Omega) |\mathcal{Z}(\Omega)| - \frac{1}{\sigma_x^2} M \alpha^2 A^2(k\Omega) - M \ln \sigma_x^2 - \frac{1}{\sigma_x^2} \mathcal{E} \right\} \quad (6.2)$$

The last term in the Log-likelihood function is discarded in Equation 6.2, because it is a constant and does not affect the result of searching maximal value. Note that σ_x^2 depends also on the estimated

parameter and it does affect the estimation result. Therefore, it cannot be ignored as a constant value.

B. Periodogram Estimator(PE)

The standard periodogram of an M -point sequence, $z[0], z[1], \dots, z[M-1]$, is defined as [So et al., 1999]

$$S_z(\Omega) = \frac{1}{M} \left| \sum_{m=0}^{M-1} z[m] e^{-jm\Omega} \right|^2 \quad (6.3)$$

A direct method for tone detection and frequency estimation is to find the maximizer of the periodogram over the frequency, which can be expressed as

$$\hat{\Omega}_{\text{PE}} = \underset{\Omega}{\operatorname{argmax}} S_z(\Omega) = \underset{\Omega}{\operatorname{argmax}} \frac{1}{M} |\mathcal{Z}(\Omega)|^2 \quad (6.4)$$

C. Least-squares Estimator(LSE)

The method of least squares is about estimating parameters by minimizing the squared discrepancies between observed data, on the one hand, and their expected values on the other [Everitt and Howell, 2005]. According to Equation 5.5 and Equation 5.14, the estimates are obtained as the minimizing arguments of the criterion

$$|z - m_z|^2 = \left[z - \alpha A(k\Omega) e^{j\theta} \mathbf{p} \right]^H \left[z - \alpha A(k\Omega) e^{j\theta} \mathbf{p} \right] \quad (6.5)$$

where $\mathbf{p} = [1, e^{j\Omega}, \dots, e^{j(M-1)\Omega}]^T$ denotes the phase rotation vector.

Through simply manipulation and neglecting the constant term, the arguments of the criterion can be modified to

$$M\alpha^2 A^2(k\Omega) - 2\Re \left[e^{-j\theta} \mathcal{Z}(\Omega) \right] \quad (6.6)$$

Similar to the derivation of the MLE, the LS estimate can be represented as

$$\hat{\Omega}_{\text{LS}} = \underset{\Omega}{\operatorname{argmax}} \left\{ 2 |\mathcal{Z}(\Omega)| - M\alpha^2 A^2(k\Omega) \right\} \quad (6.7)$$

D. Performance comparison

We can conclude that from Equation 6.2, 6.4 and Equation 6.7, except the periodogram approach, the ML estimate and LS estimate for Ω both depend on the *priori* knowledge of α . The ML estimate even needs the information about the noise power σ_v^2 . To assess the estimators, the upper bounds for the estimator performance are obtained through simulation under the assumption of known α and σ_v^2 , as shown in Figure 6.1.

All three frequency estimation approaches show the threshold phenomenon, which we have mentioned in Chapter 5. In the SNR region above the threshold, although the MLE is superior to the other methods, the differences among them are almost negligible. However, the SNR thresholds, below which the estimation variance will deteriorate dramatically, are different for the estimators. The Periodogram estimator has the smallest threshold and the threshold of the LS estimator is the largest. Meanwhile, considering that the Periodogram estimator does not need other *priori* knowledge, we

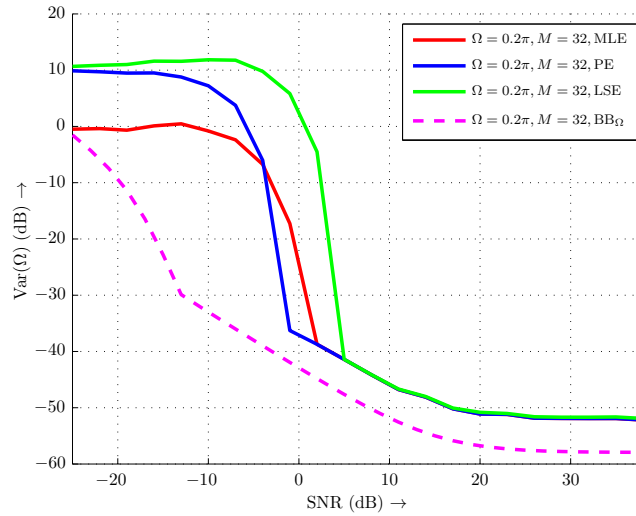


Figure 6.1: Variance of the estimates: $\alpha = 1$, $p = 1$ for BB_{Ω}

prefer to choose the periodogram approach as the basic frequency estimation algorithm to build up the frequency synchronizer.

6.3 Approximation of the Periodogram Estimate

Recall the periodogram approach

$$\hat{\Omega}_{PE} = \underset{\Omega}{\operatorname{argmax}} \frac{1}{M} |\mathcal{Z}(\Omega)|^2$$

In practice, it is not possible to use infinite number of hypotheses and the *Discrete-Time Fourier Transform (DTFT)* computation over the continuum of $[0, 2\pi)$ is a formidable operation. From the discrete-time signal processing theory [Oppenheim et al., 1999], we know that the DFT of the signal are just the samples of the DTFT of the signal and the DFT can be computed in a very efficient way by using *Fast Fourier Transform (FFT)* [Burrus et al., 2010]. Therefore, the approaches by using the interpolation of the DFT results have been proposed to approximate the DTFT result for the frequency estimation.

The methods of applying three DFT samples are proposed in [Quinn, 1994][Macleod, 1998][Cai et al., 2005]. Jacobsen has suggested a simple relation for DFT domain fine frequency estimation based on empirical observations [Jacobsen and Kootsookos, 2007]. The proof of Jacobsen's approach is given in [Candan, 2011] and Candan further proposed an improved alternative by introducing a nonlinear factor.

We evaluate the performance of Jacobsen's approach and Candan's approach on the new observation signal model. Generally, if M -point DFT is conducted to approximate DTFT, the resolution in frequency domain is $\frac{2\pi}{M}$. The true value of the frequency can be expressed as $\Omega = \frac{2\pi}{M}(k_p + \delta)$, where

$\frac{2\pi}{M}k_p$ corresponds to one of the frequency samples taken by DFT, which is closet to the true value. The main objective of the interpolation is to estimate δ , where $\delta < \frac{1}{2}$, from three samples around the peak in DFT spectrum.

Recall Jacobsen's approach and Candan's approach

$$k_p = \underset{k}{\operatorname{argmax}} |\mathcal{Z}[k]|^2 = \underset{k}{\operatorname{argmax}} \left| \sum_{m=0}^{M-1} z[m] e^{-j\frac{2\pi mk}{M}} \right|^2 \quad (6.8a)$$

$$\hat{\delta} = \begin{cases} \Re \left[\frac{\mathcal{Z}[k_p - 1] - \mathcal{Z}[k_p + 1]}{2\mathcal{Z}[k_p] - \mathcal{Z}[k_p - 1] - \mathcal{Z}[k_p + 1]} \right], & \text{Jacobsen's approach} \\ \frac{\tan(\frac{\pi}{M})}{\frac{\pi}{M}} \Re \left[\frac{\mathcal{Z}[k_p - 1] - \mathcal{Z}[k_p + 1]}{2\mathcal{Z}[k_p] - \mathcal{Z}[k_p - 1] - \mathcal{Z}[k_p + 1]} \right], & \text{Candan's approach} \end{cases} \quad (6.8b)$$

$$\hat{\Omega} = \frac{2\pi}{M}(k_p + \hat{\delta}) \quad (6.8c)$$

where $\Re[\cdot]$ denotes the operation taking the real part of a complex value.

It is obvious from Equation 6.8 that the complexity of Candan's approach is a little bit more than Jacobsen's approach because of the nonlinear factor. However, as illustrated in Figure 6.2(a), their performance curves are almost overlapped every where, i.e. Candan's approach does not show remarkable benefit on our signal model, as described in [Candan, 2011]. Therefore, Jacobsen's approach is chosen as our basic algorithm for building up the frequency estimator.

Meanwhile, when the number of observation $M = 32$, comparing the variance of the estimate obtained from the interpolation to that of the periodogram estimate, there exists around 3 dB performance loss, if $M = 64$, then the performance loss is around 5 dB.

The required asymptotic performance of the frequency estimator is discussed and given at the end of Chapter 5. According to the simulation results in Figure 6.2(a), the estimate from the interpolation of DFT cannot fulfill the requirement, if taking only 32 observations. To reduce the variance of the estimates, two common methods can be carried out: 1. taking more observations; 2. conducting averaging.

In Figure 6.2(b) we compare the performance of these two approaches, where N denotes the number of the estimate for averaging operation. We see that the estimate by taking $M = 32$, $N = 6$ has similar variance with the estimate by taking $M = 64$, $N = 1$ and both are very close to the system requirement.

Since the two approaches we took have similar performance, the coming question is, which one is preferred? Usually, more observations imply longer observation time. Therefore, to track fast frequency change $M = 32$ is preferred. Figure 6.2(b) has shown us that with help of averaging, the estimator utilizing 32 observations can achieve similar performance to the estimator with $M = 64$. However, is it possible to get multiple independent estimates with $M = 32$ for averaging, meanwhile not to extend the observation duration? For HSPA+ and LTE system, the answer is positive. In fact, we can take advantage of the diversity in time domain for HSPA+ system or in frequency domain for

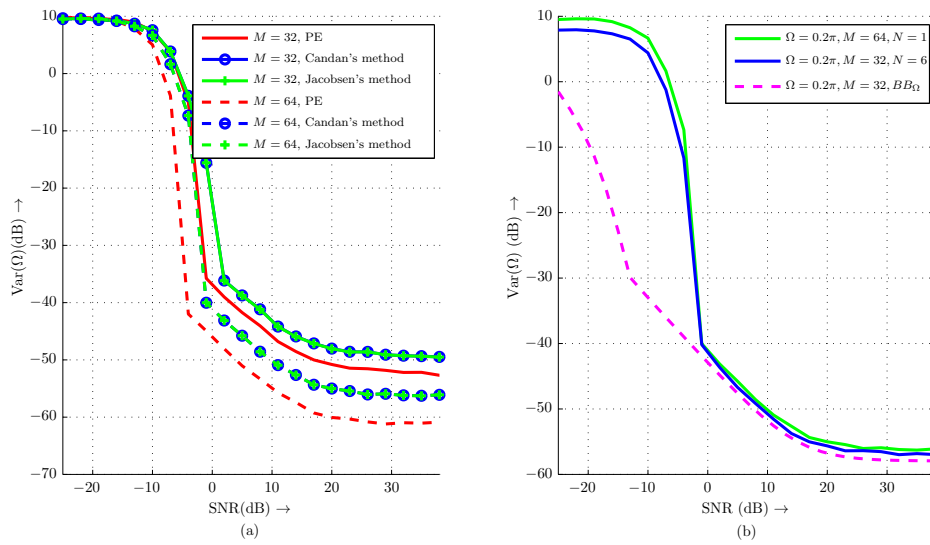


Figure 6.2: Performance comparison for the approximations of PE

LTE system to enhance frequency estimation performance.

In HSPA+ system, if the transmission channel can be modeled as a multipath channel, the rake receiver will pick up the signals from each path and treat each transmission path as a flat-fading channel, as shown in Figure 3.3. Consequently, for each finger of the rake receiver, the pilot observations can be obtained and the frequency estimation can be conducted. Similar to utilizing multipath diversity in the rake receiver, various diversity combining techniques, such as *Maximal Ratio Combining (MRC)* and *Equal Gain Combining (EGC)* [Brennan, 2003], can be exploited to enhance the estimation performance. In [ITU, 1997], most channel models suggested by ITU for IMT-2000 have six transmission paths. As to how many estimates can be obtained, it depends on how many distinguishable transmission paths the rake receiver can find out.

In LTE system, according to the frame structure in Figure 6.3, reference signal is transmitted at OFDM symbol 0 and 4 of each slot. Meanwhile, in OFDM symbol 0 and 4, multiple subcarriers are chosen for carrying reference signal. Therefore, in a dedicated observation time, all the observations from the subcarriers with same index can be grouped together as the observation vector for the estimator. Concerning the computation complexity, it is not necessary to conduct estimation process on all observation vectors. We can select several observation vectors with the largest norm to derive the estimates, and later use abovementioned diversity combining techniques to improve the estimation performance.

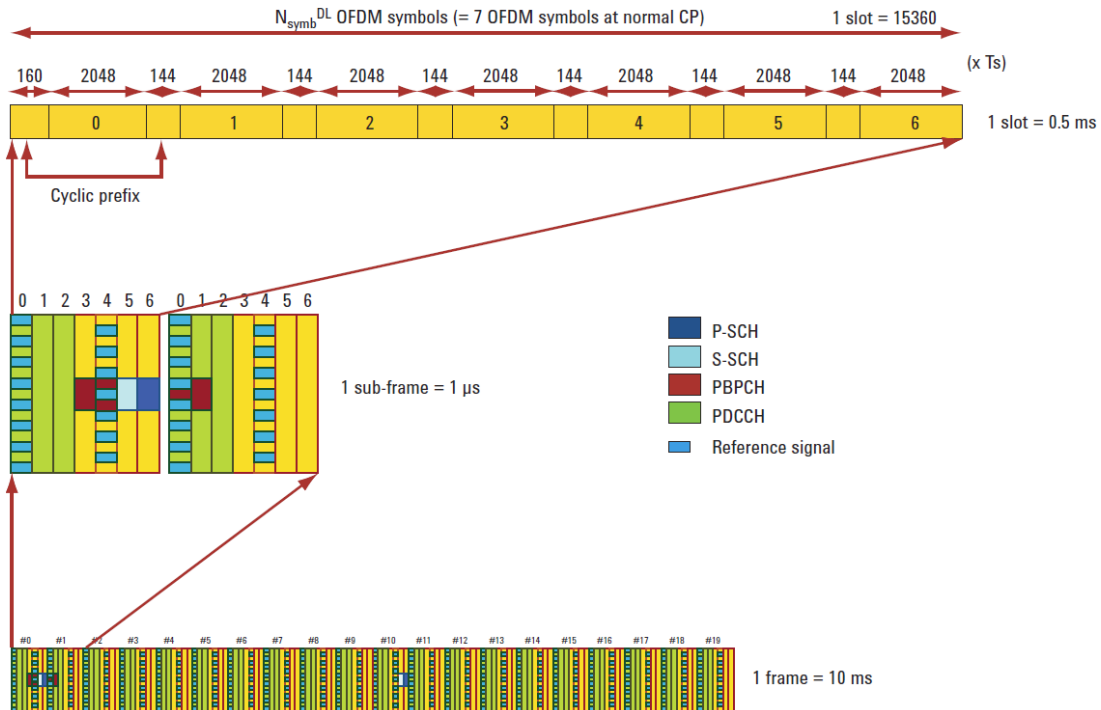


Figure 6.3: LTE FDD Frame: Type I. (From *Agilent Technologies* [2007])

6.4 Temporal-Synchronization-Aided Fast Frequency Acquisition

At the start of signal reception, the receiver has no knowledge about the synchronization parameter values. The synchronizer should be able to deliver accurate estimates of the synchronization parameters after some processing of the received signal in initial acquisition stage. Of course, for shorter switch-on delay, the sooner to achieve the estimate with required accuracy, the better. However, we have concluded previously that the estimator achieves smaller variance when the frequency offset is smaller. The large initial uncertainty about the frequency offset will limit the performance of the estimation. That means that, more observations, i.e. longer synchronization delay, are indispensable to improve estimation accuracy.

Is it possible to accelerate the frequency acquisition process and reduce the acquisition latency? As mentioned in the beginning of this chapter, for asynchronous systems the first stage in initial acquisition process is normally temporal synchronization. In HSPA+ system and LTE system, the received baseband signals are usually processed in block-wise way. This implies that different boundaries of the frame structure is required for the baseband process to correctly segment the received signals. We find out that for HSPA+ system and also LTE system, the metric for temporal synchronization, such as for slot boundary or for symbol boundary, can be utilized at the same time for coarse frequency estimation. By compensating the frequency offset obtained from coarse frequency estimation the residual frequency offset will be limited in a much smaller range and help the further frequency estimator based on the periodogram approach to provide more accurate estimates. The general structure

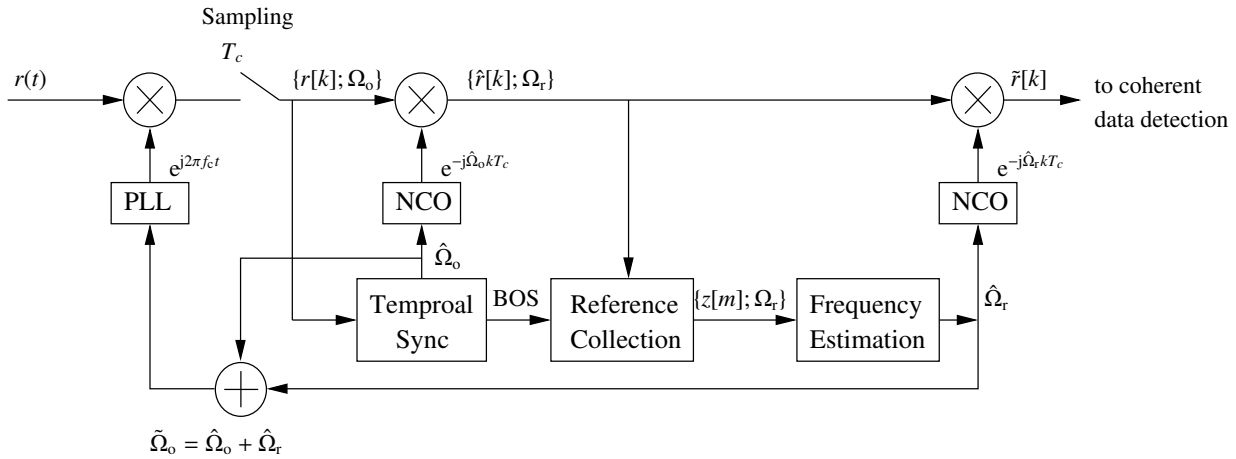


Figure 6.4: Block diagram of temporal-synchronization-aided frequency acquisition

of the algorithm is shown in Figure 6.4, which fits to both HSPA+ system and LTE system.

The received RF signal $r(t)$ is down-converted to baseband by multiplied with the local carrier $e^{j2\pi f_c t}$. The baseband signals are sampled at uniform intervals of T_c . Note that the baseband samples $\{r[k]\}$ embed the frequency offset Ω_o , which is caused by the oscillator uncertainties between the transmitter and the receiver or by the Doppler shift. The function of temporal synchronization processes $\{r[k]\}$ to acquire the timing information and provides the *Boundary of Slot or Boundary of Symbol* (BOS). If the temporal synchronization algorithm provides meanwhile the estimate of frequency offset $\hat{\Omega}_o$, it is possible to compensate the frequency offset partly. Then, the residual frequency offset $\Omega_r = \Omega_o - \hat{\Omega}_o$ will be limited in a smaller range. Of course, if the temporal sync block cannot provide any information about the frequency offset, we can just simply set $\hat{\Omega}_o = 0$, then $\Omega_r = \Omega_o$.

Later, the Reference Collection block picks up the received reference signal from the compensated samples $\{\hat{r}[k]\}$ and generates the observations $\{z[m]\}$. The estimate of the residual frequency offset $\hat{\Omega}_r$ is obtained by utilizing abovementioned periodogram approach from the observations. As shown in Figure 6.4, the applications of $\hat{\Omega}_o$ and $\hat{\Omega}_r$ are twofold: 1. compensating the frequency offset of the data in the process; 2. assisting the *Phase Lock Loop* (PLL) to generate accurate local carrier frequency.

The realization of temporal-synchronization-aided fast frequency acquisition will be introduced in the following sections for HSPA+ system and for LTE system, respectively.

6.5 Slot-Sync-Aided Frequency Acquisition in HSPA+ system

For HSPA+ system, the Temporal Sync block in Figure 6.4 refers to slot synchronization process. The metric for searching slot boundary is able to provide not only the BOS, but also the coarse frequency offset estimate.

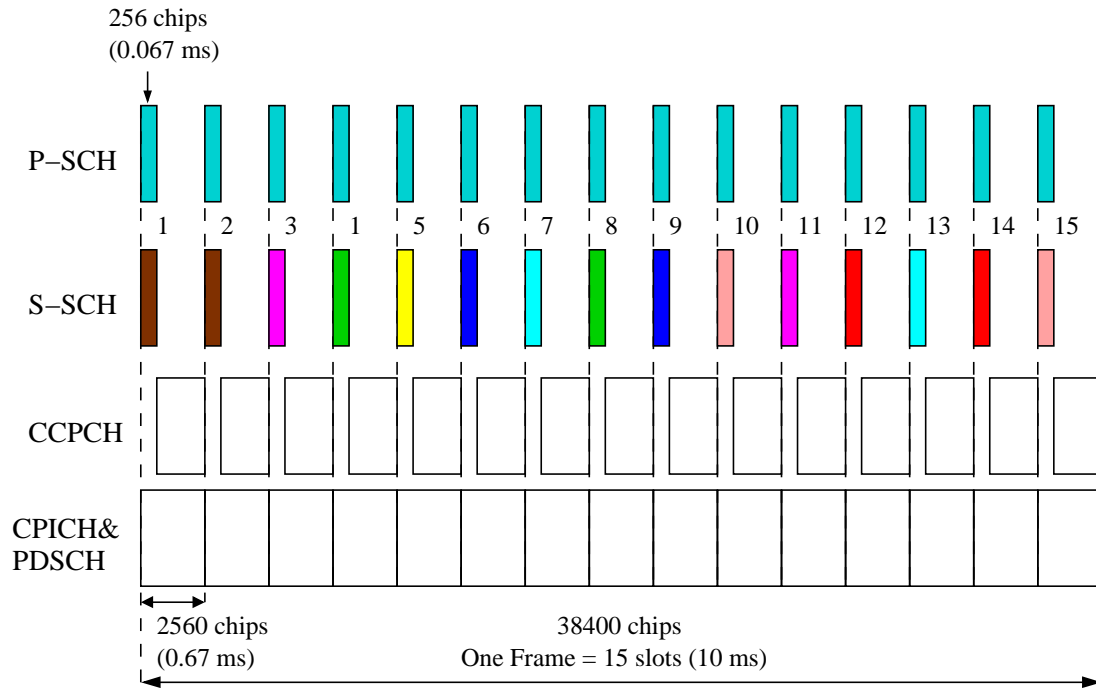


Figure 6.5: Frame and Slot Structure of HSPA+ Downlink Signals

6.5.1 Primary Synchronization Channel

HSPA+ system is an evolution version of current UMTS system, which supports asynchronous base stations. To help achieve temporal synchronization and to facilitate cell search, three channels are transmitted, namely the *Primary Synchronization Channel (P-SCH)*, the *Secondary Synchronization Channel (S-SCH)*, and the *Common Pilot Channel (CPICH)* [3GPP, 2008b]. The P-SCH together with the S-SCH are also referred to as the **SCH**.

Figure 6.5 illustrates the slot and frame formats of these channels. Each frame of 38400 chips (or 10 ms) is divided into 15 slots, of each 2560 chips (or 0.67 ms). Observe that both P-SCH and S-SCH have a 10% duty factor. The CPICH carries the reference signals, which helps the receiver to estimate the transmission channel effect and also the frequency offset. Within each CPICH time slot, there are 10 pilot symbols, each spread by 256 chips. All symbols are *Quadrature Phase-Shift Keying (QPSK)* modulated, and the modulation values of the pilot symbols are known once the receiver knows the slot boundary.

Usually, the receiver has the priori knowledge about the synchronization code carried in P-SCH and peak searching the results of the correlation operation is commonly used to determine the slot boundary of the received signal. After achieving temporal synchronization, the observed reference signals $\{z[m]\}$ are obtained by despreading CPICH signal and the parameters required for reliable data detection can be estimated based on the observations. Therefore, the correlators are the core operation units of Temporal Sync block and Reference Collection block in Figure 6.4.

Primary Synchronization Code (PSC) in P-SCH consists of 256 chips and is termed *Generalized Hierarchical Golay Sequence*. As described in [Siemens and Texas Instruments, 1999], it can be

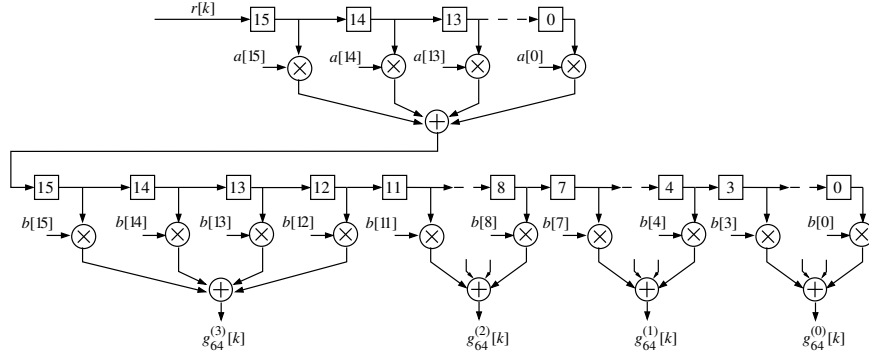


Figure 6.6: Hierarchical PSC correlator.(64-chip partial correlation)

generated by two component sequences a and b of length 16 as follows:

$$\begin{aligned}
 a &= [1, 1, 1, 1, 1, 1, -1, -1, 1, -1, 1, -1, 1, -1, -1, 1], \\
 b &= [1, 1, 1, -1, -1, 1, -1, -1, 1, 1, 1, -1, 1, -1, 1, 1], \\
 C_{\text{psc}}[k] &= (1 + j) \cdot a[k \bmod 16] \cdot b[k \div 16], \quad 0 \leq k \leq 255.
 \end{aligned} \tag{6.9}$$

The structure of the PSC allow us to use partial correlation to construct a hierarchical correlator with low complexity, as shown in Figure 6.6. Normally, the correlator of a sequence with length L_s needs L_s multipliers. However, the hierarchical correlator of the PSC with $L_s = 256$ here needs only 32 multipliers.

The correlation length of the partial correlation is $L = 64$ and the partial correlation can be expressed as

$$g_{64}^{(m)}[k] = \frac{1 - j}{128} \sum_{n=64m}^{64(m+1)-1} r[k+n] \cdot a[n \bmod 16] \cdot b[n \div 16], \quad 0 \leq m \leq 3. \tag{6.10}$$

Here the power of $g_{64}^{(m)}[k]$ is already normalized. Further, the full correlation with $L = 256$ can be expressed as

$$g_{256}^{(0)}[k] = \frac{1}{4} \sum_{m=0}^3 g_{64}^{(m)}[k] \tag{6.11}$$

6.5.2 Optimal Correlation Length in Non-coherent Case

In non-coherent case, it has been shown that the performance of the correlator suffers from the phase rotation caused by the frequency offset. Before the receiver achieves frequency synchronization, for example, in the initial acquisition stage of receiving, the received signals in the process may embed large frequency offset. Hence, the correlation length L has to be chosen carefully to avoid incoherency loss.

The objective function for optimizing the output SNR of the correlator relative to the correlation

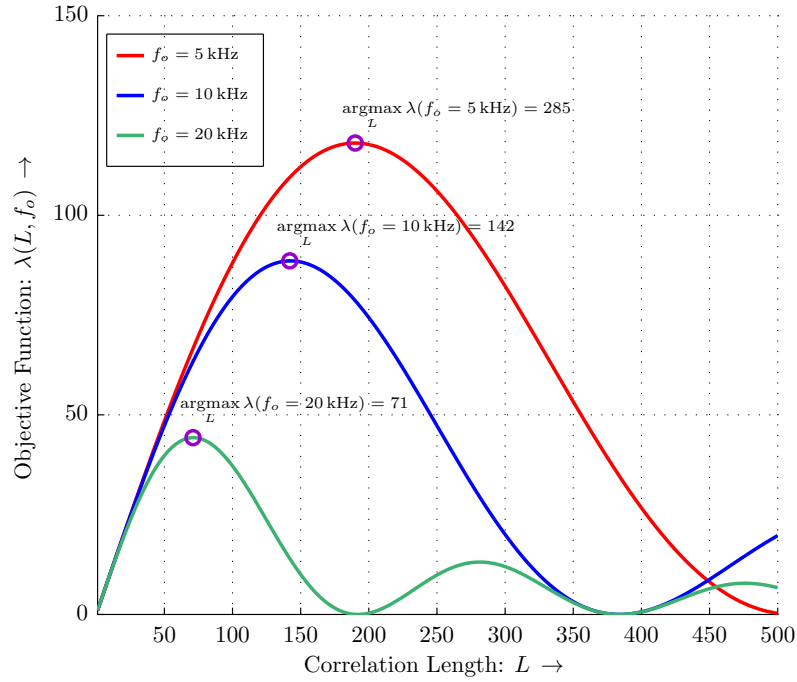


Figure 6.7: The function $\lambda(L, f_o)$ for frequency offset $f_o = 5, 10,$ and 20 kHz

length L and the frequency offset f_o can be expressed as [Wang and Ottosson, 1999]

$$\lambda(L, f_o) = \frac{\sin^2(\pi f_o L T_c)}{L \sin^2(\pi f_o T_c)} \quad (6.12)$$

For HSPA+ system, given $f_o = 5, 10, 20$ kHz and $T_c = \frac{1}{3.84 \text{ MHz}}$, the function $\lambda(L, f_o)$ is shown in Figure 6.7. The optimal correlation length for the three cases are 285, 142, and 71, respectively. Restricting L to a power of 2 for simply manipulation, the best choices of L for the three cases become 256, 128, and 64. It is clear that choosing longer correlation length in the case of small frequency offset will benefit the output SNR of the correlator.

Then, it is obvious that reducing Ω_r will bring in two positive effects to improve frequency offset estimation:

1. smaller Ω_r allows to use longer correlation length for CPICH despreading, which can improve the SNR of the observations $\{z[m]\}$;
2. according to Equation 5.11, smaller Ω_r can reduce the interference term in the observation $\{z[m]\}$;

6.5.3 Slot Synchronization with Coarse Frequency Offset Estimation

Because of the large initial frequency uncertainty in initial acquisition stage, the algorithm for acquiring slot boundary should work well also with the existence of large frequency offset. In [Moon and Lee, 2002], a correlator consists of partial correlation with $L = 64$ and the differential coherent combining is introduced to combat the incoherency loss.

Equation 6.10 and 6.11 have shown us that the special structure of the PSC allows constructing the correlator with $L = 256$ by coherently combining the results from partial correlators with $L = 64$. The performance of different combining schemes has been discussed in [Jeong et al., 2000]. For large frequency offset cases, differentially coherent combining scheme in Equation 6.13 achieves the best performance for slot boundary detection

$$p[k] = \sum_{m=1}^3 \left| \left[g_{64}^{(m-1)}[k] \right]^* g_{64}^{(m)}[k] \right| \quad (6.13)$$

and the slot boundary is detected by searching the peak value of $p[k]$ in a time window of one slot

$$\hat{K}_s = \underset{k \text{ in one slot}}{\operatorname{argmax}} p[k] \quad (6.14)$$

Meanwhile, it has been proved in [Cai et al., 2005] that in the case of slow flat fading transmission channel, the partial correlation can be expressed as

$$g_{64}^{(m)}[K_s] = A e^{j2\pi f_o \cdot 64mT_c} + n^{(m)}[K_s] \quad (6.15)$$

where A denotes a complex constant, K_s represents the index of the sample right on the slot boundary and $n^{(m)}[K_s]$ is the corresponding noise sample. Therefore, for each P-SCH we obtain four partial correlation results, which can be seen as received samples of a noise corrupted complex sinusoidal signal.

A number of efficient frequency estimators have appeared in the literature for a complex sinusoidal signal which has been corrupted by noise. Amongst these are the Lank-Reed-Pollon estimator [Lank et al., 1973] in Equation 6.16a, Kay's circular estimator [Kay, 1989] in Equation 6.16b and the *Parabolic Smoothed Central Finite Difference Estimator* (PSCFD) [Lovell et al., 1991] in Equation 6.16c.

$$\hat{\Omega}_{\text{LRP}} = \arg \left\{ \sum_{m=1}^3 g_{64}^{(m)}[K_s] \left(g_{64}^{(m-1)}[K_s] \right)^* \right\} \quad (6.16a)$$

$$\hat{\Omega}_{\text{KC}} = \arg \left\{ \sum_{m=1}^3 w_m g_{64}^{(m)}[K_s] \left(g_{64}^{(m-1)}[K_s] \right)^* \right\} \quad (6.16b)$$

$$\hat{\Omega}_{\text{PSCFD}} = \arg \left\{ \sum_{m=1}^3 \frac{w_m g_{64}^{(m)}[K_s] \left(g_{64}^{(m-1)}[K_s] \right)^*}{\left| g_{64}^{(m)}[K_s] g_{64}^{(m-1)}[K_s] \right|} \right\} \quad (6.16c)$$

where $\arg\{\cdot\}$ denotes the operation taking the argument of a complex value and $(\cdot)^*$ is the conjugate of a complex value. $w_m = \frac{6m(N-m)}{N(N^2-1)}$ are the weights of Kay's window. N is the number of observations and in our case $N = 4$. Although Kay's circular estimator and PSCFD estimator need more computation power, their computation complexities are still in the order of $O(N)$, just as that of the Land-Reed-Pollon estimator. Therefore, they are also computational efficient.

Clarkson has evaluated their performances through numerical simulation [Clarkson, 1992]. Although PSCFD estimator has the best performance in case of large number of observations and high SNR environment, all three estimators have similar performance when $N < 10$ and SNR < 4 dB. Hence, taking into account the computational complexity, the Land-Reed-Pollon estimator is adopted in our system for coarse frequency estimation. Then,

$$\hat{\Omega}_o = 2\pi\hat{f}_o T_c = \frac{1}{64}\hat{\Omega}_{\text{LRP}} = \frac{1}{64} \arg \left\{ \sum_{m=1}^3 g_{64}^{(m)}[K_s] \left(g_{64}^{(m-1)}[K_s] \right)^* \right\}. \quad (6.17)$$

After correcting the phase rotation caused by $\hat{\Omega}_o$ the residual frequency offset Ω_r in $\hat{r}[k]$ will be reduced, and then, the longer correlation length can be adopted for the correlator used for despreading CPICH to fetch the reference signals.

6.5.4 Performance Evaluation

To assess the performance of the abovementioned algorithm, a simulation environment with the parameters listed in Table 6.1 is built up, which are based on [3GPP, 2008a]. For simulating HSPA+ scenario, *Dedicated Physical Channels* (DPCHs) with SF = 16 are adopted instead of DPCHs with SF = 128 to generate the *Orthogonal Channel Noise Simulator* (OCNS). E_c/I_{or} denotes the ratio of the chip power of the dedicated physical channel and the total transmit power of a cell.

Table 6.1: Simulation parameters for HSPA+ system

Parameter	Value
CPICH E_c/I_{or}	-10 dB
CCPCH E_c/I_{or}	-10 dB
SCH E_c/I_{or} (P-SCH/S-SCH)	-13 dB/-13 dB
DPCH E_c/I_{or}	-16 dB (SF = 16)
OCNS	SF = 16, 15 channels
Sample rate	Chip rate (3.84 MHz)
Channel model	Flat Rayleigh fading

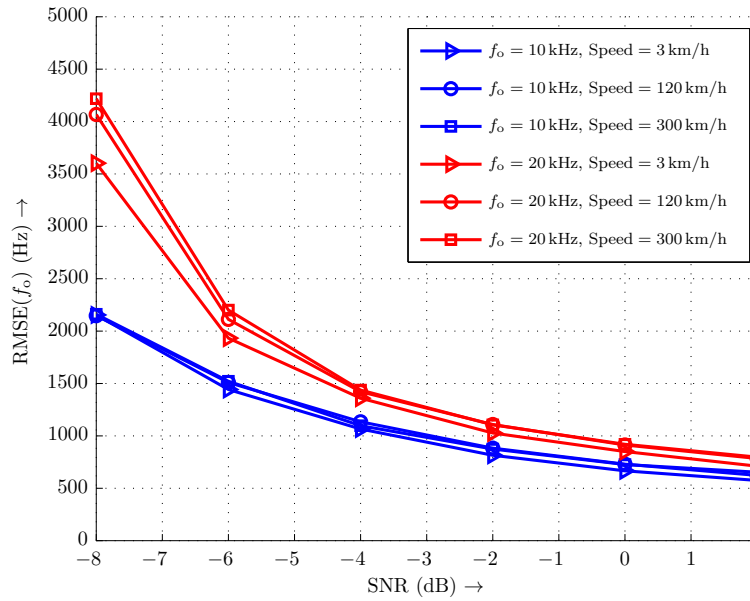


Figure 6.8: Root Mean Square Error of the coarse frequency estimation

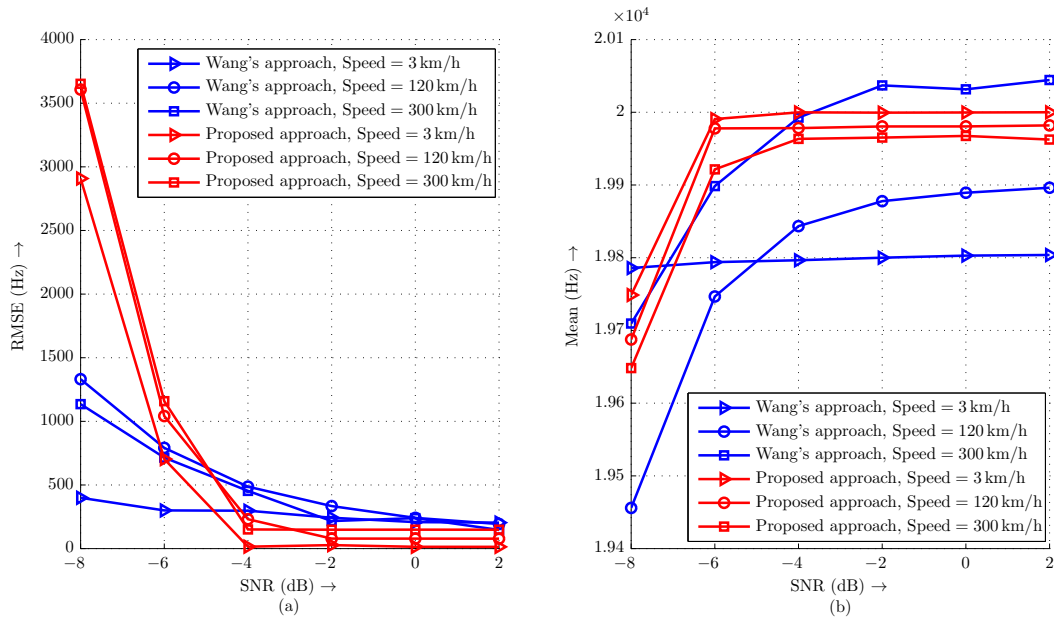


Figure 6.9: RMSEs and Means of the estimates for $f_o = 20$ kHz

Figure 6.8 shows the RMSE of the estimate in Equation 6.17 for different frequency offsets in different Doppler cases. If the frequency offset f_o is chosen as great as 20 kHz, the RMSEs of the estimates are smaller than 5 kHz when the SNR is greater than -8 dB for all Doppler cases. It implies that the correlation length $L = 256$ is optimal for despreading CPICH from $\{\hat{r}[k]\}$.

Taking $L = 256$ for despreading, Figure 6.9 compares the mean value and the RMSE of the proposed estimate to Wang's approach, which had been proved in [Wang and Ottosson, 1999] to be

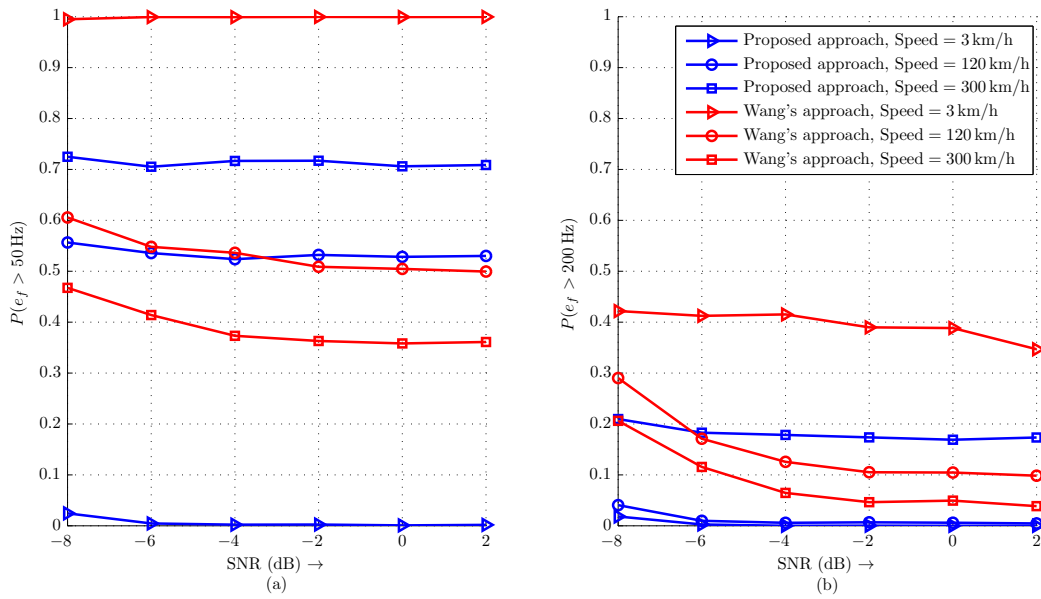


Figure 6.10: Probability of the frequency estimation error when $f_o = 20$ kHz

superior to the differential detection. It is interesting to notice from Figure 6.9(b) that the estimate from Wang's approach is asymptotically biased. In the case of very small Doppler case, i.e. Speed = 3 km/h, the bias of Wang's approach is around 200 Hz when $f_o = 20$ kHz. Furthermore, the bias of Wang's approach is greatly affected by the Doppler effect of the channel. However, the proposed approach shows asymptotically unbiased property and the Doppler effect does only slightly influence the mean value of the estimate. Figure 6.9(a) shows the comparison of the RMSEs of the estimates. The proposed approach provides smaller RMSE when the SNR is greater than -4 dB. But Wang's method is better in lower SNR range when the SNR is smaller than -5 dB. The proposed scheme is worse in low SNR case because its coarse frequency estimation algorithm, i.e. the Land-Reed-Pollon estimator, has poor performance in low SNR case.

The simulation result for the probability of the frequency estimation error $P(e_f)$ when $f_o = 20$ kHz is shown in Figure 6.10, respectively for $e_f > 50$ Hz, and $e_f > 200$ Hz. Figure 6.10(a) reveals that in small Doppler spread case, for instance Speed = 3 km/h, the most estimate errors of the proposed scheme are smaller than 50 Hz. The performance gets worse when the Doppler spread becomes larger, not like Wang's scheme, its performance becomes better when the Doppler spread grows up. However, as shown in Figure 6.10(b), when the Doppler spread is not very serious (even the speed is set as higher as 120 km/h for Carrier frequency = 2 GHz), the proposed scheme provides superior frequency acquisition performance for $P(e_f > 200$ Hz).

6.6 Symbol-Sync-Aided Frequency Acquisition in LTE system

LTE system adopts OFDM-base technique to build up the air interface of the system. Synchronization for general OFDM systems has been intensively studied in the literature. The basic idea in the literature is to split the frequency offset into a *Fractional Frequency Offset (FFO)*, an *Integer Frequency Offset (IFO)*, and a *Residual Frequency Offset (RFO)*, which can be estimated individually [Wang et al., 2010]. Considering the CP structure of the OFDM symbols, van de Beek first proposed the lagged auto-correlation approach in [van de Beek et al., 1997] to utilize the cyclostationary of the received OFDM signal to blindly acquire symbol timing and to estimate FFO. Later, a class of nondata-aided, CP based estimators for FFO estimation of OFDM system are proposed and analyzed in [Lashkarian and Kiaei, 2000]. The Cramer-Rao lower bound of the CP based FFO estimators is given in [Athaudage and Sathananthan, 2005].

In OFDM receivers, the IFO does not cause the inter-carrier interference, however, it will cause cyclic shift of the subcarriers after FFT process. Two of the most popular pilot-aided and blind IFO estimators are proposed in [Schmidl and Cox, 1997] and [Morelli et al., 2000]. Later, an IFO estimator based on the maximum likelihood principle has been derived in [Toumpakaris et al., 2009]. Specially for LTE, the algorithms based on the cross-correlation between the received signals and the synchronization channel signals are described in [Manolakis et al., 2009] and [Wang et al., 2010].

For frequency synchronization in LTE system, the Temporal Sync block in Figure 6.4 refers to the OFDM symbol synchronization process, which employs the CP based lagged auto-correlation to detect *Boundary of Frame (BOF)* and estimate $\hat{\Omega}_0$. Because the reference sequences embedded in the pilot subcarriers are cell dependent in LTE system [3GPP, 2010], the reference collection process should take advantage of the BOS to acquire the BOF and then determine the cell-ID by applying a cross-correlation between the received signal and the reference signal in the synchronization channels. Furthermore, for correct choosing the pilot signals, the reference collection process should perform the cross-correlation procedure for several cyclic shifts in the received OFDM symbols (for instance a shift of -3 to $+3$ subcarriers), in order to detect the IFO. Finally, the collected pilot signals are fed into the proposed periodogram algorithm to estimate the residual frequency offset.

6.6.1 CP based Method for Symbol Timing Synchronization and FFO Estimation

In OFDM based systems, FFO is the major source of ICI destroying the orthogonality between subcarriers. Therefore, it has to be compensated before the demodulation in the OFDM receiver.

For general OFDM systems, a CP based lagged auto-correlation scheme has been proposed in [van de Beek et al., 1997] for OFDM symbol timing synchronization and FFO estimation and it has been proved to be an ML estimator for the OFDM symbol start (ϑ) and the FFO (ε_F) in the case of an AWGN channel.

The log-likelihood function for ϑ and ε_F can be written as

$$\Lambda(\vartheta, \varepsilon_F) = 2 |\eta(\vartheta)| \cos [2\pi\varepsilon_F + \angle\eta(\vartheta)] - \rho\mathcal{E}(\vartheta) \quad (6.18)$$

where \angle denotes the argument of a complex number.

In Equation 6.18,

$$\eta(n) \equiv \sum_{k=n}^{n+N_g-1} r[k]r^*[k+N] \quad (6.19)$$

is the N -lagged auto-correlation term and

$$\mathcal{E}(n) \equiv \sum_{k=n}^{n+N_g-1} |r[k]|^2 + |r[k+N]|^2 \quad (6.20)$$

the energy term, while N_g denotes the CP length, measured in time samples, and N is the number of subcarriers of one OFDM symbol.

The magnitude of the correlation coefficient between $r[k]$ and $r[k+N]$ is given as

$$\rho \equiv \left| \frac{\text{E} \{r[k]r^*[k+N]\}}{\sqrt{\text{E} \{|r[k]|^2\} \text{E} \{|r[k+N]|^2\}}} \right| = \frac{\sigma_s^2}{\sigma_s^2 + \sigma_n^2} \quad (6.21)$$

where σ_s^2 and σ_n^2 represent the signal and noise power, respectively.

The ML estimate of ϑ and ε_F maximizes the function $\Lambda(\vartheta, \varepsilon_F)$, and is given by

$$\hat{\vartheta} = \arg \max_{\vartheta} \{2 |\eta(\vartheta)| - \rho\mathcal{E}(\vartheta)\} \quad (6.22a)$$

$$\hat{\varepsilon}_F = -\frac{1}{2\pi} \arg \{\eta(\hat{\vartheta})\} \quad (6.22b)$$

Averaging $\Lambda(\vartheta, \varepsilon_F)$ over several OFDM symbols can significantly improve the performance of this method [van de Beek et al., 1997]. Therefore, for LTE system, in the context of slow fading, the method has been extended to subframe base in [Wang et al., 2010] and considering $\hat{\Omega}_o = \frac{1}{NT_c} \varepsilon_F$, we can have

$$\hat{\Omega}_o = -\frac{1}{NT_c} \arg \left\{ \sum_{i=0}^{N_s-1} \sum_{n=0}^{N_g-1} r[i(N+N_g) + \hat{\vartheta} + n] r^*[i(N+N_g) + \hat{\vartheta} + N + n] \right\} \quad (6.23)$$

where N_s represents the number of OFDM symbols in one subframe. In an AWGN channel with sufficiently large SNR, the variance of the FFO estimator can be derived as

$$\text{Var}(\hat{\varepsilon}_F) \approx \frac{1}{4\pi^2 N_g N_s \gamma_t} \quad (6.24)$$

where γ_t denotes the average SNR of the signal in time domain.

6.6.2 Reference Signal Collection and IFO Estimation

After FFO compensation the multi-carrier demodulation is conducted by using FFT technique. The reference signal should be picked up from the results of the FFT process for estimating the parameters required for coherent receiving, such as the channel factor, the IFO and the RFO.

According to the analysis in [Toumpakaris *et al.*, 2009], the IFO ε_{IFO} has the following two effects on the received signal after the FFT process:

- A cyclic shift: The signal transmitted on subcarrier k is received on subcarrier $k + \varepsilon_{\text{IFO}}$.
- A phase change proportional to the OFDM symbol number m : The phase of all subcarriers in the m -th OFDM symbol are changed by $2\pi m\alpha\varepsilon_{\text{IFO}}$, where $\alpha = \frac{N_g}{N}$.

Therefore, the IFO should be estimated and compensated in advance in order to pick up the pilot signals from the correct subcarrier indices.

The LTE frame structure in Figure 6.3 shows that the downlink transmission is organized into radio frames with a duration of 10 ms. Each radio frame consists of 10 subframes, each with two consecutive 0.5 ms slots. A dedicated synchronization channel P-SCH is specified to be transmitted within the last OFDM symbols of the first and sixth subframe. The P-SCH signal consists of three length-62 Zadoff-Chu sequences in frequency domain, which are mutually orthogonal and mapped on the subcarriers located symmetrically around the DC-carrier. Each physical cell of the LTE system is comprised of three sectors, which are identified by carrying different P-SCH sequences.

A cross-correlation in frequency domain between the received OFDM symbols and the P-SCH sequences is proposed to simultaneously acquire the *Boundary of Half Frame (BOHF)*, the sector-ID and the IFO. Define the three P-SCH sequences as $\{S_i[k]\}$, where $i \in [0, 1, 2]$, $k \in K_{\text{PSCH}}$. K_{PSCH} denotes the subcarrier indices that contain the P-SCH signal. Note that the P-SCH signals only exist every fifth subframe, the estimation of the IFO can only be conducted in every half frame. BOHF, sector-ID and IFO can be acquired by searching the cross-correlation results within an observation window as follows:

$$\left(\hat{\vartheta}_{\text{HF}}, \hat{I}_s, \hat{\varepsilon}_{\text{IFO}}\right)^T = \arg \max_{\substack{m \in W_s \\ i \in [0, 1, 2] \\ l \in W_l}} \left| \sum_{k \in K_{\text{PSCH}}} S_i^*[k+l] R_m[k] \right| \quad (6.25)$$

where S_i^* denotes the conjugate of P-SCH sequences, $R_m[k]$ is the received OFDM symbol after the FFT process, m is the OFDM symbol index inside the observation window, W_s is the observation window with half frame length, and W_l is the searching window for estimating the IFO.

Taking the frequency uncertainty of the oscillators in LTE receivers in the range of ± 10 ppm, the maximal frequency offset can reach around ± 30 kHz at 3 GHz carrier frequency. Normalized to the 15 kHz LTE subcarrier bandwidth, the IFO should hold $\varepsilon_{\text{IFO}} \in [-2.2]$. Therefore, the searching window W_l needs only cover a small range of the potential subcarrier shifts to save the computing power, for instance, $W_l = [-3.3]$. Once the IFO is estimated, the IFO compensation can be realized by inversely cyclic shifting the subcarrier index of the received OFDM symbol and then multiplying

all the subcarriers of the OFDM symbol m with a phase factor $e^{-j2\pi\alpha m\epsilon_{\text{IFO}}}$. The pilot signals are then collected after the IFO compensation.

6.6.3 RFO Estimation

As described in Chapter 4, the observations for estimating the RFO after FFT process is obtained by multiplying the received pilot signals with the conjugates of the known reference signals. The complex-valued cell-specific reference sequences are mapped on the time-frequency resource grid on every sixth subcarrier with two OFDM symbols in every slot. How to determine the cell-ID and then to select the corresponding reference sequence are not the objective in this dissertation. The interested reader is referred to [Manolakis *et al.*, 2009] and [3GPP, 2010].

As illustrated in Figure 6.3, each radio frame consists of 20 slots. Therefore, 20 observations from one pilot subcarrier index can be collected in one radio frame. Then, the previously proposed periodogram estimator can be employed on the observations to obtain the estimate of the FFO. It is obvious that multiple subcarriers are employed in the OFDM symbol with reference signals for the pilot signal. Therefore, in one radio frame, the proposed periodogram approach can be conducted multiple times on the collections of the observations from different pilot subcarrier indices, and the average of the results will improve the estimation performance. Although better performance can be achieved by averaging more estimates, the number of times that the estimation is conducted in one radio frame is limited by the storage space for the observations and also the computing power of the processor.

6.6.4 Simulation results

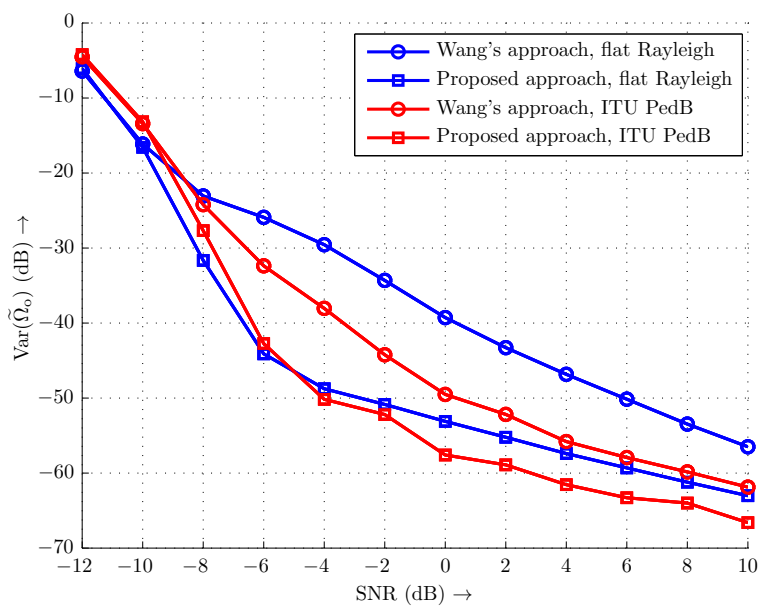
To evaluate the performance of the proposed scheme, Monte Carlo simulations are carried out using a standard compliant LTE FDD physical level simulator. The physical link parameters are listed in Table 6.2. The bandwidth of each subcarrier is 15 kHz. 20 MHz system bandwidth consists of 1320 subcarriers. Except the subcarriers assigned for signaling, 64-QAM is used to modulate all the subcarriers for the payload. Because the synchronization reference signals and the demodulation reference signals are all cell specific, without loss of generality, the cell-ID is set to zero. Two different channel models are adopted in the simulations to compare the performance of the proposed scheme in different environments. In the case of the flat Rayleigh fading channel, the channel factor is assumed to be invariable within a LTE radio frame duration, however, the channel factors for different radio frames are totally independent. For ITU Pedestrian B (PedB) channels [ITU, 1997] with time dispersion, a moving speed of 3 km/h is assumed and the Clark-Jakes model [Jakes, 1994] is used to generate the channel fading factors.

Table 6.2: Simulation parameters for LTE system

Parameter	Value
Carrier frequency	2 GHz
Bandwidth	20 MHz
FFT Size	2048
Sample rate	30.72 MHz
Symbol alphabet	64-QAM
CP length	Normal
cell-ID	0
Channel model	flat Rayleigh fading & ITU PedB
Introduced Frequency Offset	2.424 subcarrier spacings
Number of radio frames	10000

The performance is presented in Figure 6.11 in terms of the estimation variance. For performance comparison, the algorithm in [Wang *et al.*, 2010] is also conducted in the simulations, which adopts the differential phase detector to acquire the RFO.

It is obvious that the proposed scheme outperforms Wang's approach for both channel conditions. In the high SNR case (SNR = 10 dB), the estimation variance of the proposed scheme is smaller than that of Wang's approach 6 dB for both channel cases. The difference will become even greater when the SNR is getting smaller until -6 dB.

**Figure 6.11:** Variance of frequency offset estimation in LTE system:

If we take the results from last chapter as the targets, to achieving $\text{Var}(\Omega) < -58$ dB, the required SNR of the proposed approach is smaller than that of Wang's approach around 6 dB in the case of ITU PedB channel and the gap will be even bigger in flat Rayleigh fading channel case.

6.7 Summary

In this chapter, we focused on the issue of designing the frequency synchronizer for HSPA+ system and LTE system. First, the strategy of frequency synchronization was discussed for general wireless digital communication systems. Later, diverse algorithms were assessed based on the general signal model, which describes the observations in both HSPA+ system and LTE system. The evaluation results suggest us to use the interpolated periodogram algorithm for frequency estimation.

Further, according to the frame structures, a uniform implementation structure was devised for the frequency synchronizer in both HSPA+ system and LTE system. Obviously, the uniform structure can simplify the design of the Dual-Mode receiver by reusing the same function blocks.

The preferred periodogram based algorithm was employed in our design. The performance of the synchronizer is evaluated under different channel cases and the results show its advantage to other synchronizers.

Chapter 7

Conclusion

In the walk of 21st century, diverse Internet-based applications promote the blooming of the demands of wireless Internet access systems with high capability. Several techniques are proposed for the physical layers of the latest evolution of current 3G mobile communication system (HSPA+) and the upcoming 4G mobile communication system (LTE), such as 64-QAM, OFDM, MIMO, etc., in order to boost up the system throughput. These advanced techniques benefit the higher system throughput, however, the system performance becomes more sensitive to the non-idealities inside the real hardware, in which frequency offset is an important member. Therefore, it is important to understand the impairment caused by frequency offset and to evaluate its impact on the system performance in order to establish appropriate requirements for frequency synchronizer design.

In this thesis, a general framework is established to evaluate the impairment of frequency offset on HSPA+ system and LTE system. The uniform implementation structure for frequency synchronizer is also proposed for both systems, which may ease the design for a Dual-Mode receiver.

First, we derive the received signal model of a HSPA+ system with frequency offset, whose air interface takes WCDMA techniques. The impairment of frequency offset on HSPA+ system is shown to be three-fold: 1. attenuating the amplitude of the desired data symbol; 2. rotating the phase of the desired data symbol; 3. resulting inter-channel interference. Note that those effects also act on the pilot symbols which are used for channel estimation. It is well known that the channel estimation performance greatly influences the error rate performance in coherent receivers. Therefore, the error rate performance of HSPA+ receiver is degraded by the deteriorated SINR and channel estimation error both caused by frequency offset.

The influence of the frequency-offset-generated ICI to the SINR of the received signal is detailedly discussed for HSPA+ system in Chapter 3. We also propose an analytical method, which takes into account both the ICI in the received data symbols and the channel estimation error, to reveal the relation between the system error rate and the frequency offset. The simulation results show that the requirement of frequency synchronization for HSPA+ system is much more strict than that of its predecessor – UMTS system.

We further derive the received signal model of the upcoming LTE system with nonignorable frequency offset. By comparing it to the signal model for HSPA+ system, we find out that the received signal models of the these two systems are analogous, although HSPA+ system belongs to single car-

rier system and LTE system is a multi-carrier system. Therefore, a general signal model is proposed to describe the received signals of the both systems and the analytical method for evaluating the error rate of HSPA+ system is consequently generalized so as it can be applicable for both systems.

Concerning the uplink of LTE system, SC-FDMA technique, also known as DFT-spread OFDM, is employed instead of OFDMA for easing the high PAPR problem of OFDM systems. Not like in downlink system, in which there are one transmitter and multiple receivers, the uplink system consists of multiple transmitters and one receiver. Every transmitter in the uplink system corresponds to a UE. For the uplink of LTE system, the interference caused by user specific frequency offset is discussed in the thesis under different resource allocation schemes. The analysis results reveal that the interference caused by user specific frequency offset is distributed to the received data symbols by the DFT process and the interference power is dispensed more uniformly over the received data symbols in the case of LFDMA, compared to IFDMA case.

Frequency estimation plays a key role in frequency synchronization. In estimation theory, much efforts are spent on finding a lower bound for estimation variance as a benchmark for performance evaluation purposes. For estimating a deterministic parameter, if the conditional probability density function of the observations given the parameter obeys the regularity conditions, the CRB establishes a fundamental lower limit to the variance of any unbiased estimator. However, based on the proposed general signal model for HSPA+ system and LTE system, the conditional pdf of the observations given the frequency offset violates the regularity conditions because of the introduction of the interference caused by the frequency offset. As a result, the CRB for frequency offset estimation does not exist. Hence, the Barankin Bound (BB) and its approximation for frequency offset estimation in HSPA+ system and LTE system are derived in chapter 5 based on the proposed general signal model. The BB is chosen to establish the performance benchmark for unbiased estimators and it is conjunctively used with the results from the error rate evaluation process to direct the requirements for frequency synchronizer design.

Finally, the implementation issues on frequency synchronizer are discussed for both HSPA+ system and LTE system. Different frequency estimation algorithms, such as MLE, PE and LSE, are assessed and compared. The consideration of performance and complexity leads to choosing PE algorithm for frequency synchronizer implementation. Because HSPA+ system and LTE system share the same signal model, an uniform implementation structure is proposed for both systems according to their own frame structures. The performance of the proposed frequency synchronizer is evaluated via Monte Carlo simulation under different transmission channel cases. The simulation results reveal the advantage of the proposed algorithm to the other algorithms. Moreover, the uniform structure may simplify the frequency synchronizer design for the upcoming Dual-Mode receiver for HSPA+ system and LTE system, because the fine frequency estimation function is common in the structure for both HSPA+ system and LTE system so as to be reusable for both systems.

Appendices

Appendix A

Derivation of Equation 3.32

According to [Proakis, 2000], the probability of a symbol error for the M -ary QAM in AWGN channels P_M can be expressed in that for the \sqrt{M} -ary PAM $P_{\sqrt{M}}$ as

$$P_M = 1 - (1 - P_{\sqrt{M}})^2 \quad (\text{A.1})$$

Recall Equation 5.2-46 in [Proakis, 2000] for the average probability of a symbol error for M -ary PAM

$$P_M = \frac{2(M-1)}{M} Q \left(\sqrt{\frac{(6 \log_2 M) E_b}{(M^2-1) N_0}} \right), \quad (\text{A.2})$$

where $Q(x)$ the Q -function defined as

$$Q(x) = \frac{1}{\sqrt{2\pi}} \int_x^{\infty} e^{-\frac{t^2}{2}} dt, \quad x \geq 0.$$

Thus, $P_{\sqrt{M}}$ in Equation A.1 is

$$P_{\sqrt{M}} = 2 \left(1 - \frac{1}{\sqrt{M}} \right) Q \left(\sqrt{\frac{(3 \log_2 M) E_b}{(M-1) N_0}} \right) \quad (\text{A.3})$$

Substituting Equation A.3 in Equation A.1, yields

$$\begin{aligned} P_M &= 1 - (1 - P_{\sqrt{M}})^2 \\ &= 2P_{\sqrt{M}} \left(1 - \frac{1}{2} P_{\sqrt{M}} \right) \\ &= 4 \left(1 - \frac{1}{\sqrt{M}} \right) Q \left(\sqrt{\frac{3 \log_2 M E_b}{M-1 N_0}} \right) \times \left[1 - \left(1 - \frac{1}{\sqrt{M}} \right) Q \left(\sqrt{\frac{3 \log_2 M E_b}{M-1 N_0}} \right) \right] \end{aligned} \quad (\text{A.4})$$

Appendix B

Derivation of Equation 3.51

Recall Equation 3.50 as follow

$$\begin{aligned} P_M(E | z_h, \hat{z}_h) &= \frac{1}{M} \sum_{m=2}^{M-1} P(|\hat{d}_P - A_m| > D | z_h, \hat{z}_h) \\ &+ \frac{1}{M} P(\hat{d}_P - A_1 > D | z_h, \hat{z}_h) \\ &+ \frac{1}{M} P(\hat{d}_P - A_M < -D | z_h, \hat{z}_h) \end{aligned} \quad (\text{B.1})$$

Note that the indices i in the equation are dropped for simplicity of notation. Obviously, the RHS of the equation consists of three parts. We will manipulate them respectively. Firstly, according to Equation 3.44, the part in the first summation operation can be expressed as

$$\begin{aligned} P(|\hat{d}_P - A_m| > D | z_h, \hat{z}_h) &= P\left(\left|\left(\frac{z_h}{\hat{z}_h} - 1\right)(2m - 1 - M)D + \frac{\nu}{\hat{z}_h}\right| > D | z_h, \hat{z}_h\right) \\ &= P\left(\left(\frac{z_h}{\hat{z}_h} - 1\right)(2m - 1 - M)D + \frac{\nu}{\hat{z}_h} > D | z_h, \hat{z}_h\right) \\ &+ P\left(\left(\frac{z_h}{\hat{z}_h} - 1\right)(2m - 1 - M)D + \frac{\nu}{\hat{z}_h} < -D | z_h, \hat{z}_h\right) \\ &= P(\nu > (\hat{z}_h - z_h)(2m - 1 - M)D + \hat{z}_h D | z_h, \hat{z}_h) \\ &+ P(\nu < (\hat{z}_h - z_h)(2m - 1 - M)D - \hat{z}_h D | z_h, \hat{z}_h) \end{aligned} \quad (\text{B.2})$$

where ν is the combination of the noise and the ICI caused by the frequency offset. Because the PAM signals are one-dimensional signals, ν are also one-dimensional. Assuming random variable ν has

Gaussian distribution with mean $\mu = 0$ and variance $\sigma_v^2 = \frac{N_1}{2}$, we obtain

$$\begin{aligned}
P(|\hat{d}_P - A_m| > D | z_h, \hat{z}_h) &= \frac{1}{\sqrt{\pi N_1}} \int_{(\hat{z}_h - z_h)(2m-1-M)D + \hat{z}_h D}^{+\infty} \exp\left(-\frac{v^2}{N_1}\right) dv \\
&\quad + \frac{1}{\sqrt{\pi N_1}} \int_{-\infty}^{(\hat{z}_h - z_h)(2m-1-M)D - \hat{z}_h D} \exp\left(-\frac{v^2}{N_1}\right) dv \\
&= Q\left([\!(2m - M)\hat{z}_h - (2m - 1 - M)z_h] \frac{\sqrt{2}D}{N_1}\right) \\
&\quad + Q\left([\!(2m - 1 - M)z_h - (2m - 2 - M)\hat{z}_h] \frac{\sqrt{2}D}{N_1}\right)
\end{aligned} \tag{B.3}$$

Similarly, the rest two parts of the RHS of Equation B.1 can be expressed as

$$P(\hat{d}_P - A_1 > D | z_h, \hat{z}_h) = Q\left([\!(M - 1)z_h - (M - 2)\hat{z}_h] \frac{\sqrt{2}D}{N_1}\right) \tag{B.4a}$$

$$P(\hat{d}_P - A_M < -D | z_h, \hat{z}_h) = Q\left([\!(M - 1)z_h - (M - 2)\hat{z}_h] \frac{\sqrt{2}D}{N_1}\right) \tag{B.4b}$$

Substituting Equation B.3, B.4a and B.4b to Equation B.1, we obtain the SER conditioned on z_h and \hat{z}_h as

$$\begin{aligned}
P_M(E | z_h, \hat{z}_h) &= \frac{1}{M} \sum_{m=2}^{M-1} Q\left([\!(2m - M)\hat{z}_h - (2m - 1 - M)z_h] \frac{\sqrt{2}D}{N_1}\right) \\
&\quad + \frac{1}{M} \sum_{m=2}^{M-1} Q\left([\!(2m - 1 - M)z_h - (2m - 2 - M)\hat{z}_h] \frac{\sqrt{2}D}{N_1}\right) \\
&\quad + \frac{2}{M} Q\left([\!(M - 1)z_h - (M - 2)\hat{z}_h] \frac{\sqrt{2}D}{N_1}\right)
\end{aligned} \tag{B.5}$$

Taking $n = M + 1 - m$, the second term of the RHS in Equation B.5 can be rewritten to

$$\begin{aligned}
\frac{1}{M} \sum_{m=2}^{M-1} Q\left([\!(2m - 1 - M)z_h - (2m - 2 - M)\hat{z}_h] \frac{\sqrt{2}D}{N_1}\right) \\
= \frac{1}{M} \sum_{n=2}^{M-1} Q\left([\!(2n - M)\hat{z}_h - (2n - 1 - M)z_h] \frac{\sqrt{2}D}{N_1}\right)
\end{aligned} \tag{B.6}$$

Thus, Equation B.5 can be further expressed as

$$\begin{aligned}
 P_M(E | z_h, \hat{z}_h) &= \frac{2}{M} \sum_{m=2}^{M-1} Q \left([(2m - M)\hat{z}_h - (2m - 1 - M)z_h] \frac{\sqrt{2D}}{N_1} \right) \\
 &\quad + \frac{2}{M} Q \left([(M - 1)z_h - (M - 2)\hat{z}_h] \frac{\sqrt{2D}}{N_1} \right) \\
 &= \frac{2}{M} \sum_{m=1}^{M-1} Q \left([(2m - M)\hat{z}_h - (2m - 1 - M)z_h] \frac{\sqrt{2D}}{N_1} \right)
 \end{aligned} \tag{B.7}$$

Appendix C

Derivation of ρ and r in Equation 3.55

According to the definitions in Equation 3.45 and Equation 3.55,

$$\rho = \frac{\text{cov}(z_h^2, \hat{z}_h^2)}{\sqrt{\text{var}(z_h^2) \text{var}(\hat{z}_h^2)}} \quad ; \quad r = \frac{\hat{\Omega}}{\Omega} \quad (\text{C.1})$$

where $\Omega = E\{z_h^2\}$, $\hat{\Omega} = E\{\hat{z}_h^2\}$.

Recall Equation 3.43

$$\tilde{h} = h + \frac{\nu}{d_p}$$

where d_p is the pilot symbol and ν denotes the interference and the noise in the pilot channel with $\mu_\nu = 0$ and $\sigma_\nu^2 = N_1$.

Assuming h and ν are two independent random variables, we have

$$\begin{aligned} \text{cov}(z_h^2, \hat{z}_h^2) &= E\{z_h^2 \hat{z}_h^2\} - E\{z_h^2\} E\{\hat{z}_h^2\} = E\{hh^* \tilde{h} \tilde{h}^*\} - \Omega \hat{\Omega} \\ &= E\left\{z_h^2 \left(h + \frac{\nu}{d_p}\right) \left(h^* + \frac{\nu^*}{d_p}\right)\right\} - \Omega \hat{\Omega} \\ &= E\left\{z_h^2 z_h^2 + z_h^2 \frac{|\nu|^2}{|d_p|^2}\right\} - \Omega \hat{\Omega} \\ &= E\{z_h^4\} + \frac{\sigma_\nu^2}{|d_p|^2} \Omega - \Omega \hat{\Omega} \end{aligned} \quad (\text{C.2})$$

and

$$\begin{aligned} \hat{\Omega} &= E\{\hat{z}_h^2\} = E\{\tilde{h} \tilde{h}^*\} \\ &= E\left\{\left(h + \frac{\nu}{d_p}\right) \left(h^* + \frac{\nu^*}{d_p}\right)\right\} \\ &= E\{z_h^2\} + \frac{\sigma_\nu^2}{|d_p|^2} \\ &= \Omega + \frac{\sigma_\nu^2}{|d_p|^2} \end{aligned} \quad (\text{C.3})$$

Substituting Equation C.3 to Equation C.2, we get

$$\text{cov}(z_h^2, \hat{z}_h^2) = E\{z_h^4\} - \Omega^2 \quad (\text{C.4})$$

According to the probability density function of z_h in Equation 3.44, the first term of the RHS of Equation C.4 can be expressed as

$$E\{z_h^4\} = \int_0^{+\infty} z_h^4 \frac{2\Omega}{z_h} \exp\left(-\frac{z_h^2}{\Omega}\right) dz_h \quad (\text{C.5})$$

By using integration by parts it is easy to figure out $E\{z_h^4\} = 2\Omega^2$. Finally we obtain

$$\text{cov}(z_h^2, \hat{z}_h^2) = \Omega^2 \quad (\text{C.6})$$

Now we investigate $\text{var}(z_h^2)$

$$\text{var}(z_h^2) = E\{(z_h^2)^2\} - E\{z_h^2\}^2 = 2\Omega^2 - \Omega^2 = \Omega^2 \quad (\text{C.7})$$

Similarly, we also have $\text{var}(\hat{z}_h^2) = \hat{\Omega}^2$. Taking above into account, we obtain

$$\begin{aligned} \rho &= \frac{\text{cov}(z_h^2, \hat{z}_h^2)}{\sqrt{\text{var}(z_h^2) \text{var}(\hat{z}_h^2)}} = \frac{\Omega^2}{\sqrt{\Omega^2 \hat{\Omega}^2}} \\ &= \frac{\Omega}{\hat{\Omega}} = \frac{1}{r} = \frac{\Omega}{\Omega + \frac{\sigma_v^2}{|d_p|^2}} \\ &= \frac{1}{1 + \frac{\sigma_v^2}{\Omega |d_p|^2}} \end{aligned} \quad (\text{C.8})$$

If the average power of pilot symbols equals to the average power of data symbols, given the variance of the complex random noise $\sigma_v^2 = N_1$, yields

$$\frac{\Omega |d_p|^2}{\sigma_v^2} = \frac{\Omega \mathcal{E}_{av}}{N_1} = \log_2 M \frac{\Omega \mathcal{E}_b}{N_1} = \log_2 M \bar{\lambda}_b \quad (\text{C.9})$$

Thus,

$$\rho = \frac{1}{1 + \frac{1}{\log_2 M \bar{\lambda}_b}} = \frac{\log_2 M \bar{\lambda}_b}{1 + \log_2 M \bar{\lambda}_b} ; \quad r = \frac{1}{\rho} = 1 + \frac{1}{\log_2 M \bar{\lambda}_b} \quad (\text{C.10})$$

where $\bar{\lambda}_b$ denotes the average SINR per bit of the decision symbol.

Appendix D

Derivation of Equation 3.66

Define $\hat{l}_p = \Re\{\hat{d}_p\}$ and recall Equation 3.64 to obtain

$$\hat{l}_p = \frac{z_h}{\hat{z}_h} \cos \psi S_I - \frac{z_h}{\hat{z}_h} \sin \psi S_Q + \frac{\varpi_I}{\hat{z}_h} \quad (\text{D.1})$$

Similar to Equation B.1, we have the conditional SER for M -ary PAM signal as

$$\begin{aligned} P_M(E | z_h, \hat{z}_h, \psi) &= \frac{1}{M} \sum_{m=2}^{M-1} P(|\hat{l}_p - A_m| > D | z_h, \hat{z}_h, \psi) \\ &\quad + \frac{1}{M} P(\hat{l}_p - A_1 > D | z_h, \hat{z}_h, \psi) + \frac{1}{M} P(\hat{l}_p - A_M < -D | z_h, \hat{z}_h, \psi) \\ &= \frac{1}{M} \sum_{m=1}^{M-1} P(\hat{l}_p - A_m > D | z_h, \hat{z}_h, \psi) + \frac{1}{M} \sum_{m=2}^M P(\hat{l}_p - A_m < -D | z_h, \hat{z}_h, \psi) \end{aligned} \quad (\text{D.2})$$

Assuming equally probable signals for the transmitted data symbol and substituting Equation D.1 to the first term of the RHS of Equation D.2, we obtain

$$\begin{aligned} &P(\hat{l}_p - A_m > D | z_h, \hat{z}_h, \psi) \\ &= \frac{1}{M} \sum_{i=1}^M P(\hat{l}_p - A_m > D | z_h, \hat{z}_h, \psi, S_Q = A_i) \\ &= \frac{1}{M} \sum_{i=1}^M P(\varpi_I > (\hat{z}_h - z_h \cos \psi)(2m - 1 - M)D + z_h \sin \psi A_i + \hat{z}_h D | z_h, \hat{z}_h, \psi) \\ &= \frac{1}{M} \sum_{i=1}^M Q \left(\left\{ [(M + 1 - 2m) \cos \psi + (2i - 1 - M) \sin \psi] z_h + (2m - M) \hat{z}_h \right\} \frac{\sqrt{2}D}{N_1} \right) \end{aligned} \quad (\text{D.3})$$

Similarly, the second term of the RHS of Equation D.2 can be expressed as

$$\begin{aligned} &P(\hat{l}_p - A_m < -D | z_h, \hat{z}_h, \psi) \\ &= \frac{1}{M} \sum_{i=1}^M P(\hat{l}_p - A_m < -D | z_h, \hat{z}_h, \psi, S_Q = A_i) \\ &= \frac{1}{M} \sum_{i=1}^M Q \left(\left\{ (M + 2 - 2m) \hat{z}_h + [(2m - 1 - M) \cos \psi - (2i - 1 - M) \sin \psi] z_h \right\} \frac{\sqrt{2}D}{N_1} \right) \end{aligned} \quad (\text{D.4})$$

Taking $m = M + 1 - n$ and $i = M + 1 - j$, yields

$$\begin{aligned} & P(\hat{l}_P - A_m < -D \mid z_h, \hat{z}_h, \psi) \\ &= \frac{1}{M} \sum_{j=1}^M Q \left(\{[(M + 1 - 2n) \cos \psi + (2j - 1 - M) \sin \psi]z_h + (2n - M)\hat{z}_h\} \frac{\sqrt{2}D}{N_1} \right) \end{aligned} \quad (\text{D.5})$$

Comparing Equation D.3 and Equation D.5, we can find out that they have the same form. Thus, after substituting Equation D.3 and D.5 into Equation D.2, we obtain

$$P_M(E \mid z_h, \hat{z}_h, \psi) = \frac{2}{M^2} \sum_{m=1}^{M-1} \sum_{i=1}^M Q \left(\{[(M + 1 - 2m) \cos \psi + (2i - 1 - M) \sin \psi]z_h + (2m - M)\hat{z}_h\} \frac{\sqrt{2}D}{N_1} \right) \quad (\text{D.6})$$

Appendix E

Parity of $P_M(E | z_h, \hat{z}_h, \psi)$ in Equation 3.66

Recall Equation 3.66

$$P_M(E | z_h, \hat{z}_h, \psi) = \frac{2}{M^2} \sum_{m=1}^{M-1} \sum_{i=1}^M Q \left(\{[(M+1-2m) \cos \psi + (2i-1-M) \sin \psi] z_h + (2m-M) \hat{z}_h\} \frac{\sqrt{2D}}{N_1} \right) \quad (\text{E.1})$$

Substituting $-\psi$ and $i = M+1-j$ into Equation E.1, yields

$$\begin{aligned} P_M(E | z_h, \hat{z}_h, -\psi) &= \frac{2}{M^2} \sum_{m=1}^{M-1} \sum_{j=1}^M Q \left(\{[(M+1-2m) \cos(-\psi) - (2j-1-M) \sin(-\psi)] z_h + (2m-M) \hat{z}_h\} \frac{\sqrt{2D}}{N_1} \right) \\ &= \frac{2}{M^2} \sum_{m=1}^{M-1} \sum_{j=1}^M Q \left(\{[(M+1-2m) \cos \psi + (2j-1-M) \sin \psi] z_h + (2m-M) \hat{z}_h\} \frac{\sqrt{2D}}{N_1} \right) \end{aligned} \quad (\text{E.2})$$

Comparing Equation E.1 and Equation E.2, it is obvious that $P_M(E | z_h, \hat{z}_h, \psi) = P_M(E | z_h, \hat{z}_h, -\psi)$, i.e. $P_M(E | z_h, \hat{z}_h, \psi)$ is an even function with respect to ψ .

Appendix F

Derivation of Equation 4.47

Because $\mathbf{W}_{i,k} = \frac{1}{\sqrt{N_d}} e^{-j\frac{2\pi}{N_d}ik}$, $\mathbf{W}_{k,j}^{-1} = \frac{1}{\sqrt{N_d}} e^{j\frac{2\pi}{N_d}kj}$ and $\mathbf{C} = \text{diag}(0, 1, 2, \dots, N_d - 1)$, Equation 4.46 can be rewritten as

$$[\mathbf{B}^{(1,u)}]_{i,j} = j2\pi\Delta F^{(1,u)} \frac{1}{N_d} \sum_{k=0}^{N_d-1} k e^{-j\frac{2\pi}{N_d}k(j-i)} \quad (\text{F.1})$$

In the case $i = j$, we obtain

$$[\mathbf{B}^{(1,u)}]_{i,i} = j2\pi\Delta F^{(1,u)} \frac{1}{N_d} \sum_{k=0}^{N_d-1} k = j2\pi\Delta F^{(1,u)} \frac{N_d - 1}{2} \quad (\text{F.2})$$

If $i \neq j$, defining $l = j - i$ and $x = e^{-j\frac{2\pi}{N_d}l}$, we can rewrite Equation F.1 to

$$[\mathbf{B}^{(1,u)}]_{i,j} = j2\pi\Delta F^{(1,u)} \frac{1}{N_d} \sum_{k=0}^{N_d-1} k x^k \quad (\text{F.3})$$

Upon employing the property of geometric series, we obtain

$$\begin{aligned} \frac{1}{N_d} \sum_{k=0}^{N_d-1} k x^k &= \frac{1}{N_d} \sum_{k=1}^{N_d-1} k x^k = \frac{x}{N_d} \frac{d}{dx} \left(\sum_{k=1}^{N_d-1} x^k \right) \\ &= \frac{x}{N_d} \frac{1 - x^{N_d}}{(1-x)^2} + \frac{x^{N_d}}{x-1} \end{aligned} \quad (\text{F.4})$$

Since $x = e^{-j\frac{2\pi}{N_d}l}$, we have $x^{N_d} = e^{-j2\pi l} = 1$. Therefore,

$$\frac{1}{N_d} \sum_{k=0}^{N_d-1} k x^k = \frac{1}{x-1} = \frac{1}{e^{-j\frac{2\pi}{N_d}l} - 1} \quad (\text{F.5})$$

Combining the results of Equation F.2 – F.3 and Equation F.5, we obtain

$$[\mathbf{B}^{(1,u)}]_{i,j} = j2\pi\Delta F^{(1,u)} \cdot \begin{cases} \frac{N_d - 1}{2}, & m = n \\ \frac{1}{e^{-j\frac{2\pi}{N_d}(j-i)} - 1}, & m \neq n \end{cases} \quad (\text{F.6})$$

Appendix G

Non-linear Approximation of Barankin Bound

Non-linear approximation of Barankin bound for the case of *Complex Circular Gaussian Deterministic Signal Model* is derived in [Chaumette et al., 2009] and [Chaumette et al., 2008]. It is rewritten here for completeness.

Let us consider an $2M$ -dimensional Gaussian real vector \mathbf{x} with mean $\mathbf{m}_x = \mathbf{m}_x(\boldsymbol{\eta})$ and covariance matrix $\mathbf{K}_x = \mathbf{K}_x(\boldsymbol{\eta})$: $\mathbf{x} \sim \mathcal{N}_M(\mathbf{m}_x(\boldsymbol{\eta}), \mathbf{K}_x(\boldsymbol{\eta}))$ and $p(\mathbf{x}; \boldsymbol{\eta}) = p(\mathbf{x}; \mathbf{m}_x(\boldsymbol{\eta}), \mathbf{K}_x(\boldsymbol{\eta}))$. The Gaussian real pdf has the following factorization property [Chaumette et al., 2008]:

$$\begin{aligned} \frac{p(\mathbf{x}; \boldsymbol{\eta}_i)p(\mathbf{x}; \boldsymbol{\eta}_j)}{p(\mathbf{x}; \boldsymbol{\eta})} &= \frac{p(\mathbf{x}; \mathbf{m}_x(\boldsymbol{\eta}_i), \mathbf{K}_x(\boldsymbol{\eta}_i)) p(\mathbf{x}; \mathbf{m}_x(\boldsymbol{\eta}_j), \mathbf{K}_x(\boldsymbol{\eta}_j))}{p(\mathbf{x}; \mathbf{m}_x(\boldsymbol{\eta}), \mathbf{K}_x(\boldsymbol{\eta}))} \\ &= \mathbf{G}_{i,j} p(\mathbf{x}; \mathbf{K}_x^{ij} \mathbf{m}_x^{ij}, \mathbf{K}_x^{ij}) \end{aligned} \quad (\text{G.1})$$

where

$$\mathbf{K}_x^{ij} = \left[\mathbf{K}_x(\boldsymbol{\eta}_i)^{-1} + \mathbf{K}_x(\boldsymbol{\eta}_j)^{-1} - \mathbf{K}_x(\boldsymbol{\eta})^{-1} \right]^{-1} \quad (\text{G.2a})$$

$$\mathbf{m}_x^{ij} = \mathbf{K}_x(\boldsymbol{\eta}_i)^{-1} \mathbf{m}_x(\boldsymbol{\eta}_i) + \mathbf{K}_x(\boldsymbol{\eta}_j)^{-1} \mathbf{m}_x(\boldsymbol{\eta}_j) - \mathbf{K}_x(\boldsymbol{\eta})^{-1} \mathbf{m}_x(\boldsymbol{\eta}) \quad (\text{G.2b})$$

$$\delta^{ij} = \mathbf{m}_x(\boldsymbol{\eta}_i)^T \mathbf{K}_x(\boldsymbol{\eta}_i)^{-1} \mathbf{m}_x(\boldsymbol{\eta}_i) + \mathbf{m}_x(\boldsymbol{\eta}_j)^T \mathbf{K}_x(\boldsymbol{\eta}_j)^{-1} \mathbf{m}_x(\boldsymbol{\eta}_j) - \mathbf{m}_x(\boldsymbol{\eta})^T \mathbf{K}_x(\boldsymbol{\eta})^{-1} \mathbf{m}_x(\boldsymbol{\eta}) \quad (\text{G.2c})$$

$$\mathbf{G}_{i,j} = \sqrt{\frac{|\mathbf{K}_x^{ij}| |\mathbf{K}_x(\boldsymbol{\eta})|}{|\mathbf{K}_x(\boldsymbol{\eta}_i)| |\mathbf{K}_x(\boldsymbol{\eta}_j)|}} \exp \left[\frac{(\mathbf{m}_x^{ij})^T \mathbf{K}_x^{ij} \mathbf{m}_x^{ij} - \delta^{ij}}{2} \right] \quad (\text{G.2d})$$

Therefore, we obtain

$$\begin{aligned} \mathbf{E}_\eta \left[\frac{p(\mathbf{x}; \boldsymbol{\eta}_i)p(\mathbf{x}; \boldsymbol{\eta}_j)}{p(\mathbf{x}; \boldsymbol{\eta})p(\mathbf{x}; \boldsymbol{\eta})} \right] &= \int \frac{p(\mathbf{x}; \boldsymbol{\eta}_i)p(\mathbf{x}; \boldsymbol{\eta}_j)}{p(\mathbf{x}; \boldsymbol{\eta})} d\mathbf{x} \\ &= \mathbf{G}_{i,j} \int p(\mathbf{x}; \mathbf{K}_x^{ij} \mathbf{m}_x^{ij}, \mathbf{K}_x^{ij}) d\mathbf{x} \\ &= \mathbf{G}_{i,j} \end{aligned} \quad (\text{G.3})$$

An M -dimensional Gaussian complex vector \mathbf{z} with mean \mathbf{m}_z and covariance matrix \mathbf{K}_z is actually a $2M$ -dimensional Gaussian real vector $\mathbf{x} \sim \mathcal{N}_{2M}(\mathbf{m}_x, \mathbf{K}_x)$, where $\mathbf{x} = (\Re\{z_1\}, \dots, \Re\{z_M\}, \Im\{z_1\}, \dots, \Im\{z_M\})$.

Therefore, the Gaussian real vector pdf can be rewritten as a Gaussian complex vector pdf by using a few lines of algebra [van den Bos, 1995]. Especially for a complex circular vector $\mathbf{z} \sim \mathcal{CN}_M(\mathbf{m}_z, \mathbf{K}_z)$ verifying $\mathbf{K}_{z,z^*} = 0$, we have

$$\begin{aligned} p(\mathbf{x}; \mathbf{m}_x, \mathbf{K}_x) &= p(\vec{\mathbf{z}}; \mathbf{m}_{\vec{\mathbf{z}}}, \mathbf{K}_{\vec{\mathbf{z}}}) = p(\mathbf{z}; \mathbf{m}_z, \mathbf{K}_z) \\ &= \frac{1}{(\pi)^M |\mathbf{K}_z|} \exp\left[-(\mathbf{z} - \mathbf{m}_z)^H \mathbf{K}_z^{-1} (\mathbf{z} - \mathbf{m}_z)\right] \end{aligned} \quad (\text{G.4})$$

where

$$\vec{\mathbf{z}} = \begin{pmatrix} \mathbf{z} \\ \mathbf{z}^* \end{pmatrix} = \mathbf{T}^{-1} \mathbf{x} \quad (\text{G.5a})$$

$$\mathbf{T} = \frac{1}{2} \begin{bmatrix} \mathbf{I}_M & \mathbf{I}_M \\ -j\mathbf{I}_M & j\mathbf{I}_M \end{bmatrix}, \quad \mathbf{T}^{-1} = 2\mathbf{T}^H \quad (\text{G.5b})$$

From Equation G.5a and G.5b, it is straightforward to get

$$\mathbf{m}_{\vec{\mathbf{z}}}(\boldsymbol{\eta}) = \begin{pmatrix} \mathbf{m}_z(\boldsymbol{\eta}) \\ \mathbf{m}_z^*(\boldsymbol{\eta}) \end{pmatrix}, \quad \mathbf{m}_x(\boldsymbol{\eta}) = \mathbf{T}\mathbf{m}_{\vec{\mathbf{z}}}(\boldsymbol{\eta}) \quad (\text{G.6a})$$

$$\mathbf{K}_{\vec{\mathbf{z}}}(\boldsymbol{\eta}) = \begin{bmatrix} \mathbf{K}_z(\boldsymbol{\eta}) & \mathbf{0} \\ \mathbf{0} & \mathbf{K}_z(\boldsymbol{\eta})^* \end{bmatrix}, \quad \mathbf{K}_x(\boldsymbol{\eta}) = \mathbf{T}\mathbf{K}_{\vec{\mathbf{z}}}(\boldsymbol{\eta})\mathbf{T}^H \quad (\text{G.6b})$$

Subsequently, for a complex circular vector we obtain

$$\begin{aligned} \mathbb{E}_{\boldsymbol{\eta}} \left[\frac{p(\mathbf{z}; \boldsymbol{\eta}_i) p(\mathbf{z}; \boldsymbol{\eta}_j)}{p(\mathbf{z}; \boldsymbol{\eta}) p(\mathbf{z}; \boldsymbol{\eta})} \right] &= \int \frac{p(\mathbf{z}; \boldsymbol{\eta}_i) p(\mathbf{z}; \boldsymbol{\eta}_j)}{p(\mathbf{z}; \boldsymbol{\eta})} d\mathbf{z} = \int \frac{p(\mathbf{x}; \boldsymbol{\eta}_i) p(\mathbf{x}; \boldsymbol{\eta}_j)}{p(\mathbf{x}; \boldsymbol{\eta})} d\mathbf{x} \\ &= \mathbf{G}_{i,j}^{\vec{\mathbf{z}}} \end{aligned} \quad (\text{G.7})$$

where

$$\mathbf{G}_{i,j}^{\vec{\mathbf{z}}} = \sqrt{\frac{|\mathbf{K}_{\vec{\mathbf{z}}}^{ij}| |\mathbf{K}_{\vec{\mathbf{z}}}(\boldsymbol{\eta})|}{|\mathbf{K}_{\vec{\mathbf{z}}}(\boldsymbol{\eta}_i)| |\mathbf{K}_{\vec{\mathbf{z}}}(\boldsymbol{\eta}_j)|}} \exp \left[\frac{(\mathbf{m}_{\vec{\mathbf{z}}}^{ij})^H \mathbf{K}_{\vec{\mathbf{z}}}^{ij} \mathbf{m}_{\vec{\mathbf{z}}}^{ij} - \delta_{\vec{\mathbf{z}}}^{ij}}{2} \right] \quad (\text{G.8a})$$

$$\mathbf{K}_{\vec{\mathbf{z}}}^{ij} = \left[\mathbf{K}_{\vec{\mathbf{z}}}(\boldsymbol{\eta}_i)^{-1} + \mathbf{K}_{\vec{\mathbf{z}}}(\boldsymbol{\eta}_j)^{-1} - \mathbf{K}_{\vec{\mathbf{z}}}(\boldsymbol{\eta})^{-1} \right]^{-1} \quad (\text{G.8b})$$

$$\mathbf{m}_{\vec{\mathbf{z}}}^{ij} = \mathbf{K}_{\vec{\mathbf{z}}}(\boldsymbol{\eta}_i)^{-1} \mathbf{m}_{\vec{\mathbf{z}}}(\boldsymbol{\eta}_i) + \mathbf{K}_{\vec{\mathbf{z}}}(\boldsymbol{\eta}_j)^{-1} \mathbf{m}_{\vec{\mathbf{z}}}(\boldsymbol{\eta}_j) - \mathbf{K}_{\vec{\mathbf{z}}}(\boldsymbol{\eta})^{-1} \mathbf{m}_{\vec{\mathbf{z}}}(\boldsymbol{\eta}) \quad (\text{G.8c})$$

$$\delta_{\vec{\mathbf{z}}}^{ij} = \mathbf{m}_{\vec{\mathbf{z}}}(\boldsymbol{\eta}_i)^H \mathbf{K}_{\vec{\mathbf{z}}}(\boldsymbol{\eta}_i)^{-1} \mathbf{m}_{\vec{\mathbf{z}}}(\boldsymbol{\eta}_i) + \mathbf{m}_{\vec{\mathbf{z}}}(\boldsymbol{\eta}_j)^H \mathbf{K}_{\vec{\mathbf{z}}}(\boldsymbol{\eta}_j)^{-1} \mathbf{m}_{\vec{\mathbf{z}}}(\boldsymbol{\eta}_j) - \mathbf{m}_{\vec{\mathbf{z}}}(\boldsymbol{\eta})^H \mathbf{K}_{\vec{\mathbf{z}}}(\boldsymbol{\eta})^{-1} \mathbf{m}_{\vec{\mathbf{z}}}(\boldsymbol{\eta}) \quad (\text{G.8d})$$

If the non-linear transformation $t_q(y) = y^q$ is conducted on the pdf in Equation G.4, we get

$$\begin{aligned} t_q(p(\mathbf{z}; \boldsymbol{\eta}_i)) &= p(\mathbf{z}; \mathbf{m}_x(\boldsymbol{\eta}_i), \mathbf{K}_x(\boldsymbol{\eta}_i))^q \\ &= k(\boldsymbol{\eta}_i, q) p\left(\mathbf{z}; \mathbf{m}_z(\boldsymbol{\eta}_i), \frac{1}{q} \mathbf{K}_z(\boldsymbol{\eta}_i)\right) \\ &= k(\boldsymbol{\eta}_i, q) p\left(\mathbf{z}; \mathbf{m}_z(\boldsymbol{\eta}_i), \tilde{\mathbf{K}}_z(\boldsymbol{\eta}_i)\right) \end{aligned} \quad (\text{G.9})$$

where $k(\boldsymbol{\eta}_i, q) = \frac{1}{q^M} |\pi \mathbf{K}_z(\boldsymbol{\eta}_i)|^{1-q}$ is a constant w.r.t. \mathbf{x} and $\tilde{\mathbf{K}}_z(\boldsymbol{\eta}_i) = \frac{1}{q} \mathbf{K}_z(\boldsymbol{\eta}_i)$.

Then,

$$\begin{aligned} \mathbb{E}_\eta \left[\frac{t_q(p(\mathbf{z}; \boldsymbol{\eta}_i)) t_q(p(\mathbf{z}; \boldsymbol{\eta}_j))}{p(\mathbf{z}; \boldsymbol{\eta}) p(\mathbf{z}; \boldsymbol{\eta})} \right] &= k(\boldsymbol{\eta}_i, q) k(\boldsymbol{\eta}_j, q) \mathbb{E}_\eta \left[\frac{p(\mathbf{z}; \mathbf{m}_z(\boldsymbol{\eta}_i), \tilde{\mathbf{K}}_z(\boldsymbol{\eta}_i)) p(\mathbf{z}; \mathbf{m}_z(\boldsymbol{\eta}_j), \tilde{\mathbf{K}}_z(\boldsymbol{\eta}_j))}{p(\mathbf{z}; \mathbf{m}_z(\boldsymbol{\eta}), \mathbf{K}_z(\boldsymbol{\eta})) p(\mathbf{z}; \mathbf{m}_z(\boldsymbol{\eta}), \mathbf{K}_z(\boldsymbol{\eta}))} \right] \\ &= k^{ij}(q) \tilde{\mathbf{G}}_{i,j}^z \end{aligned} \quad (\text{G.10})$$

where

$$k^{ij}(q) = \frac{1}{q^{2M}} |\pi^2 \mathbf{K}_z(\boldsymbol{\eta}_i) \mathbf{K}_z(\boldsymbol{\eta}_j)|^{1-q} \quad (\text{G.11a})$$

$$\tilde{\mathbf{G}}_{i,j}^z = \frac{1}{q^M} \sqrt{\frac{|\tilde{\mathbf{K}}_z^{ij}| |\mathbf{K}_z(\boldsymbol{\eta})|}{|\mathbf{K}_z(\boldsymbol{\eta}_i)| |\mathbf{K}_z(\boldsymbol{\eta}_j)|}} \exp \left\{ \frac{q \left[(\tilde{\mathbf{m}}_z^{ij})^H \tilde{\mathbf{K}}_z^{ij} \tilde{\mathbf{m}}_z^{ij} - \tilde{\delta}_z^{ij} \right]}{2} \right\} \quad (\text{G.11b})$$

$$\tilde{\mathbf{K}}_z^{ij} = \left[\mathbf{K}_z(\boldsymbol{\eta}_i)^{-1} + \mathbf{K}_z(\boldsymbol{\eta}_j)^{-1} - \frac{1}{q} \mathbf{K}_z(\boldsymbol{\eta})^{-1} \right]^{-1} \quad (\text{G.11c})$$

$$\tilde{\mathbf{m}}_z^{ij} = \mathbf{K}_z(\boldsymbol{\eta}_i)^{-1} \mathbf{m}_z(\boldsymbol{\eta}_i) + \mathbf{K}_z(\boldsymbol{\eta}_j)^{-1} \mathbf{m}_z(\boldsymbol{\eta}_j) - \frac{1}{q} \mathbf{K}_z(\boldsymbol{\eta})^{-1} \mathbf{m}_z(\boldsymbol{\eta}) \quad (\text{G.11d})$$

$$\tilde{\delta}_z^{ij} = \mathbf{m}_z(\boldsymbol{\eta}_i)^H \mathbf{K}_z(\boldsymbol{\eta}_i)^{-1} \mathbf{m}_z(\boldsymbol{\eta}_i) + \mathbf{m}_z(\boldsymbol{\eta}_j)^H \mathbf{K}_z(\boldsymbol{\eta}_j)^{-1} \mathbf{m}_z(\boldsymbol{\eta}_j) - \frac{1}{q} \mathbf{m}_z(\boldsymbol{\eta})^H \mathbf{K}_z(\boldsymbol{\eta})^{-1} \mathbf{m}_z(\boldsymbol{\eta}) \quad (\text{G.11e})$$

If we have $\mathbf{K}_z(\boldsymbol{\eta}) = \sigma_z^2(\boldsymbol{\eta}) \mathbf{I}_M$, Equation G.10 can be simplified to

$$\mathbb{E}_\eta \left[\frac{t_q(p(\mathbf{z}; \boldsymbol{\eta}_i)) t_q(p(\mathbf{z}; \boldsymbol{\eta}_j))}{p(\mathbf{z}; \boldsymbol{\eta}) p(\mathbf{z}; \boldsymbol{\eta})} \right] = k^{ij}(q) \tilde{\mathbf{G}}_{i,j}^z \quad (\text{G.12})$$

where

$$k^{ij}(q) = \frac{[\pi^2 \sigma_z^2(\boldsymbol{\eta}_i) \sigma_z^2(\boldsymbol{\eta}_j)]^{(1-q)M}}{q^{2M}} \quad (\text{G.13a})$$

$$\tilde{\mathbf{G}}_{i,j}^z = \left[\frac{\sigma_z^2(\boldsymbol{\eta}) c_z^{ij}}{q \sigma_z^2(\boldsymbol{\eta}_i) \sigma_z^2(\boldsymbol{\eta}_j)} \right]^M \exp \left(c_z^{ij} \|\tilde{\mathbf{m}}_z^{ij}\|^2 - \tilde{\delta}_z^{ij} \right) \quad (\text{G.13b})$$

$$c_z^{ij} = \left[\frac{1}{\sigma_z^2(\boldsymbol{\eta}_i)} + \frac{1}{\sigma_z^2(\boldsymbol{\eta}_j)} - \frac{1}{q \sigma_z^2(\boldsymbol{\eta})} \right]^{-1} \quad (\text{G.13c})$$

$$\tilde{\mathbf{m}}_z^{ij} = \frac{\mathbf{m}_z(\boldsymbol{\eta}_i)}{\sigma_z^2(\boldsymbol{\eta}_i)} + \frac{\mathbf{m}_z(\boldsymbol{\eta}_j)}{\sigma_z^2(\boldsymbol{\eta}_j)} - \frac{\mathbf{m}_z(\boldsymbol{\eta})}{q \sigma_z^2(\boldsymbol{\eta})} \quad (\text{G.13d})$$

$$\tilde{\delta}_z^{ij} = \frac{\|\mathbf{m}_z(\boldsymbol{\eta}_i)\|^2}{\sigma_z^2(\boldsymbol{\eta}_i)} + \frac{\|\mathbf{m}_z(\boldsymbol{\eta}_j)\|^2}{\sigma_z^2(\boldsymbol{\eta}_j)} - \frac{\|\mathbf{m}_z(\boldsymbol{\eta})\|^2}{q \sigma_z^2(\boldsymbol{\eta})} \quad (\text{G.13e})$$

Bibliography

- 3GPP (2006), UTRA-UTRAN Long Term Evolution (LTE) and 3GPP System Architecture Evolution (SAE), <http://www.3gpp.org/Highlights/LTE/LTE.htm>.
- 3GPP (2008a), User Equipment (UE) radio transmission and reception (FDD), *TS 25.101*, 3rd Generation Partnership Project (3GPP).
- 3GPP (2008b), Physical channels and mapping of transport channels onto physical channels (FDD), *TS 25.211*, 3rd Generation Partnership Project (3GPP).
- 3GPP (2008c), Spreading and modulation (FDD), *TS 25.213*, 3rd Generation Partnership Project (3GPP).
- 3GPP (2010), Evolved Universal Terrestrial Radio Access (E-UTRA); Physical channels and modulation (FDD), *TS 36.211*, 3rd Generation Partnership Project (3GPP).
- Abel, J. S. (1993), A bound on mean-square-estimate error, *IEEE Transactions on Information Theory*, VOL. 39, pp. 1675–1680.
- Agilent Technologies (2007), Solutions for 3GPP LTE, *Technical overview*.
- Alouini, M.-S., and A. J. Goldsmith (1999), A Unified Approach for Calculating Error Rates of Linearly Modulated Signals over Generalized Fading Channels, *IEEE Transactions on Communications*, 47.
- Athaudage, C., and K. Sathanathan (2005), Cramer-Rao Lower Bound on Frequency Offset Estimation Error in OFDM Systems with Timing Error Feedback Compensation, in *Information, Communications and Signal Processing, 2005 Fifth International Conference on*, pp. pp. 1231 –1235, doi:10.1109/ICICS.2005.1689251.
- Barankin, E. W. (1949), Locally best unbiased estimates, *The Annals of Mathematical Statistics*, VOL. 20(NO. 4), pp. 477–501.
- Barbieri, A., and G. Colavolpe (2007), On the cramer-rao bound for carrier frequency estimation in the presence of phase noise, *IEEE Transactions on Wireless Communications*, NO. 6(NO. 2), pp. 575 –582, doi:10.1109/TWC.2007.05270.

- Besson, O., and P. Stoica (1995), Sinusoidal signals with random amplitude: least-squares estimators and their statistical analysis, *IEEE Transactions on Signal Processing*, VOL. 43(NO. 11), pp. 2733–2744, doi:10.1109/78.482122.
- Besson, O., and P. Stoica (1998), Frequency estimation and detection for sinusoidal signals with arbitrary envelope: a nonlinear least-squares approach, in *Acoustics, Speech and Signal Processing, 1998. Proceedings of the 1998 IEEE International Conference on*, vol. VOL. 4, pp. pp. 2209–2212, doi:10.1109/ICASSP.1998.681586.
- Bhattacharyy, A. (1947), On some analogues of the amount of information and their use in statistical estimation, *Shankya*, VOL. 8(NO. 3), pp. 201–218.
- Blischke, W. R., A. J. Truelove, and P. B. Mundle (1969), On Non-Regular Estimation. I. Variance Bounds for Estimators of Location Parameters, *Journal of the American Statistical Association*, VOL. 64(NO. 327), pp. 1056–1072.
- Brennan, D. (2003), Linear diversity combining techniques, *Proceedings of the IEEE*, VOL. 91(NO. 2), pp. 331–356, doi:10.1109/JPROC.2002.808163.
- Burrus, C. S., M. Frigo, S. G. Johnson, M. Poeschel, and I. Selesnick (2010), Fast Fourier Transforms, in *Fast Fourier Transforms, CONNEXIONS*.
- Cai, Q., A. Wilzcek, and T. Kaiser (2005), A compound method for initial frequency acquisition in WCDMA systems, in *DSPenabledRadio, 2005. The 2nd IEE/EURASIP Conference on (Ref. No. 2005/11086)*, pp. pp. 8–12.
- Candan, C. (2011), A Method For Fine Resolution Frequency Estimation From Three DFT Samples, *IEEE Signal Processing Letters*, VOL. 18(NO. 6), pp. 351–354, doi:10.1109/LSP.2011.2136378.
- Cao, L., and N. C. Beaulieu (2004), Exact Error-Rate Analysis of Diversity 16-QAM With Channel Estimation Error, *IEEE Transactions on Communications*, VOL. 52(NO. 12), pp. 1019–1029.
- Chaumette, E., J. Galy, A. Quinlan, and P. Larzabal (2008), A New Barankin Bound Approximation for the Prediction of the Threshold Region Performance of Maximum-Likelihood Estimators, *IEEE Transactions on Signal Processing*, VOL. 56(NO. 11), pp. 5319–5333, doi: 10.1109/TSP.2003.815391.
- Chaumette, E., A. Renaux, and P. Larzabal (2009), Lower bounds on the mean square error derived from mixture of linear and non-linear transformations of the unbiasedness definition, in *Acoustics, Speech and Signal Processing, 2009. ICASSP 2009. IEEE International Conference on*, pp. 3045–3048, doi:10.1109/ICASSP.2009.4960266.
- Clarkson, V. (1992), Efficient Single Frequency Estimators, in *the International Symposium on Signal Processing and its Applications*.

- Davenport, W., and W. L. Root (1958), *Random Signals and Noise*, 4th ed., McGraw Hill.
- Ekstrom, H., A. Furuskar, J. Karlsson, M. Meyer, S. Parkvall, J. Torsner, and M. Wahlqvist (2006), Technical solutions for the 3G long-term evolution, *IEEE Communications Magazine*, VOL. 44(NO. 3), pp. 38 – 45, doi:10.1109/MCOM.2006.1607864.
- Everitt, B. S., and D. Howell (2005), *Encyclopedia of Statistics in Behavioral Science*, 1st ed., Wiley.
- Feng, L., P. Fan, and X. Tang (2007), A General Construction of OVSA Codes With Zero Correlation Zone, *IEEE SIGNAL PROCESSING LETTERS*, VOL. 14.
- Fraser, D. A. S., and I. Guttman (1952), Bhattacharyya bounds without regularity assumptions, *The Annals of Mathematical Statistics*, VOL. 23(NO. 4), pp. 629–632.
- Gallager, R. G. (2008a), *Principles of Digital Communication*, Cambridge University Press.
- Gallager, R. G. (2008b), Circularly-Symmetric Gaussian random vectors, <http://www.rle.mit.edu/rgallager/documents/CircSymGauss.pdf>.
- Gray, R. M. (2006), Toeplitz and Circulant Matrices: A review, in *Foundations and Trends in Communications and Information Theory*, vol. VOL. 2, pp. pp. 155–239.
- Huang, D., and K. Letaief (2006), Carrier frequency offset estimation for OFDM systems using Null subcarriers, *IEEE Transactions on Communications*, VOL. 54(NO. 5), pp. 813 – 823, doi:10.1109/TCOMM.2006.874001.
- ITU (1997), Guidelines for valuation of radio transmission technologies for IMT-2000, *Recommendation*, International Telecommunication Union.
- Jacobsen, E., and P. Kootsookos (2007), Fast, Accurate Frequency Estimators [DSP Tips Tricks], *IEEE Signal Processing Magazine*, VOL. 24(NO. 3), pp. 123 –125, doi:10.1109/MSP.2007.361611.
- Jakes, W. C. (1994), *Microwave Mobile Communications*, 2nd ed., Wiley-IEEE Press.
- James, B., B. Anderson, and R. Williamson (1995), Characterization of threshold for single tone maximum likelihood frequency estimation, *IEEE Transactions on Signal Processing*, VOL. 43(NO. 4), pp. 817 –821, doi:10.1109/78.376834.
- Jeong, Y. K., K. B. Lee, and O.-S. Shin (2000), Differentially Coherent Combining for Slot Synchronization in Inter-Cell Asynchronous DS/SS Systems, in *Proceedings of The 11th IEEE International Symposium on Personal, Indoor and Mobile Radio Communications, 2000 (PIMRC 2000)*, vol. VOL. 2, pp. pp. 1405 –1409, doi:10.1109/PIMRC.2000.881649.
- Kay, S. (1989), A fast and accurate single frequency estimator, *IEEE Transactions on Acoustics, Speech and Signal Processing*, VOL. 37(NO. 12), pp. 1987 –1990, doi:10.1109/29.45547.

- Kay, S. M. (1993), *Fundamentals of Statistical Signal Processing, Volume I: Estimation Theory*, 1st ed., Prentice Hall.
- Kiefer, J. (1952), On minimum variance estimation, *The Annals of Mathematical Statistics*, VOL. 23(NO. 4), pp. 627–629.
- Kim, C.-J., Y.-S. Kim, G.-Y. Jeong, J.-K. Mun, and H.-J. Lee (1996), SER Analysis of QAM with Space Diversity in Rayleigh Fading Channels, *ETRI Journal*, VOL. 17(NO. 4), pp. 25–35.
- Knockaert, L. (1997), The Barankin bound and threshold behavior in frequency estimation, *IEEE Transactions on Signal Processing*, VOL. 45(NO. 9), pp. 2398–2401, doi:10.1109/78.622965.
- Korde, M., and A. Gandhi (2012), Issues in time and frequency synchronization in wcdma system, in *Advances in Mobile Network, Communication and its Applications (MNCAPPS), 2012 International Conference on*, pp. pp. 11–16, doi:10.1109/MNCApps.2012.8.
- Kutoyants, Y. A. (2008), ON REGULAR AND SINGULAR ESTIMATION FOR ERGODIC DIFFUSION, *JOURNAL OF THE JAPAN STATISTICAL SOCIETY*, VOL. 38(NO. 1), pp. 51 – 63.
- Lank, G., I. Reed, and G. Pollon (1973), A Semicohherent Detection and Doppler Estimation Statistic, *IEEE Transactions on Aerospace and Electronic Systems*, VOL. AES-9(NO. 2), pp. 151–165, doi: 10.1109/TAES.1973.309762.
- Lashkarian, N., and S. Kiaei (2000), Class of cyclic-based estimators for frequency-offset estimation of OFDM systems, *IEEE Transactions on Communications*, VOL. 48(NO. 12), pp. 2139–2149, doi:10.1109/26.891224.
- Li, Y., H. Minn, and J. Zeng (2010), An average Cramer-Rao bound for frequency offset estimation in frequency-selective fading channels, *IEEE Transactions on Wireless Communications*, VOL. 9(NO. 3), pp. 871–875, doi:10.1109/TWC.2010.03.080608.
- Lin, Y.-P., and S.-M. Phoong (2003), BER minimized OFDM systems with channel independent precoders, *IEEE Transactions on Signal Processing*, VOL. 51(NO. 9), pp. 2369–2380, doi:10.1109/TSP.2003.815391.
- Liu, L., Y.-L. Guan, G. Bi, and D. Shao (2011), Effect of Carrier Frequency Offset on Single-Carrier CDMA With Frequency-Domain Equalization, *IEEE Transactions on Vehicular Technology*, VOL. 60(NO. 1), pp. 174–184, doi:10.1109/TVT.2010.2087779.
- Lovell, B., P. Kootsookos, and R. Williamson (1991), The circular nature of discrete-time frequency estimates, in *Acoustics, Speech, and Signal Processing, 1991. ICASSP-91., 1991 International Conference on*, pp. pp. 3369–3372 vol.5, doi:10.1109/ICASSP.1991.150176.

- Luise, M., and R. Reggiannini (1996), Carrier Frequency Acquisition and Tracking for OFDM Systems, *IEEE Transactions on Communications*, VOL. 44(NO. 11), pp. 1590 – 1598, doi:10.1109/26.544476.
- Macleod, M. (1998), Fast nearly ML estimation of the parameters of real or complex single tones or resolved multiple tones, *IEEE Transactions on Signal Processing*, VOL. 46(NO. 1), pp. 141 –148, doi:10.1109/78.651200.
- Manolakis, K., D. Gutierrez Estevez, V. Jungnickel, W. Xu, and C. Drewes (2009), A Closed Concept for Synchronization and Cell Search in 3GPP LTE Systems, in *Wireless Communications and Networking Conference, 2009. WCNC 2009. IEEE*, pp. pp. 1 –6, doi:10.1109/WCNC.2009.4917491.
- McAulay, R., and L. P. Seidman (1969), A useful form of the Barankin lower bound and its application to PPM threshold analysis, *IEEE Transactions on Information Theory*, VOL. IT-15, pp. 273–279.
- Meyr, H., M. Moeneclaey, and S. A. Fechtel (1997), *Digital Communication Receivers: Synchronization, Channel Estimation, and Signal Processing*, vol. 2, Wiley-Interscience.
- Molisch, A. F. (2000), *Wideband Wireless Digital Communications*, 4th ed., Prentice Hall.
- Moon, J., and Y.-H. Lee (2002), Cell search robust to initial frequency offset in WCDMA systems, in *Proceedings of The 13th IEEE International Symposium on Personal, Indoor and Mobile Radio Communications, 2002 (PIMRC 2002)*, vol. VOL. 5, pp. pp. 2039 – 2043, doi:10.1109/PIMRC.2002.1046502.
- Morelli, M., A. D’Andrea, and U. Mengali (2000), Frequency ambiguity resolution in OFDM systems, *IEEE Communications Letters*, VOL. 4(NO. 4), pp. 134 –136, doi:10.1109/4234.841321.
- Myung, H. G., J. Lim, and D. J. Goodman (2006), Single carrier FDMA for uplink wireless transmission, *IEEE Vehicular Technology Magazine*, VOL. 1(NO. 3), pp. 30 –38, doi:10.1109/MVT.2006.307304.
- Nokia Siemens Networks (2010), Long Term HSPA Evolution: Mobile broadband evolution beyond 3GPP Release 10, *White paper*, Nokia Siemens Networks.
- Oppenheim, A. V., R. W. Schaffer, and J. R. Buck (1999), *Discrete-Time Signal Processing*, 2nd ed., Prentice Hall.
- Pollet, T., and M. Moeneclaey (1996), The effect of carrier frequency offset on the performance of band limited single carrier and OFDM signals, in *Global Telecommunications Conference, 1996. GLOBECOM '96. 'Communications: The Key to Global Prosperity*, vol. VOL. 1, pp. pp. 719 –723, doi:10.1109/GLOCOM.1996.594455.

- Pollet, T., M. Van Bladel, and M. Moeneclaey (1995), BER sensitivity of OFDM systems to carrier frequency offset and Wiener phase noise, *IEEE Transactions on Communications*, VOL. 43(NO. 234), pp. 191–193, doi:10.1109/26.380034.
- Proakis, J. G. (2000), *Digital Communications, (4-th edition)*, 4th ed., McGraw Hill.
- Quinn, B. (1994), Estimating frequency by interpolation using Fourier coefficients, *IEEE Transactions on Signal Processing*, VOL. 42(NO. 5), pp. 1264–1268, doi:10.1109/78.295186.
- Rife, D. C., and R. R. Boorstyn (1974), Single-Tone Parameter Estimation from Discrete-Time Observations, *IEEE Transactions on Information Theory*, VOL. 20(NO. 5), pp. 591–598.
- Rupp, M., S. Caban, C. Mehlführer, and M. Wrulich (2011), *Evaluation of HSDPA and LTE: From Testbed Measurements to System Level Performance*, 1st ed., Wiley.
- Schmidl, T., and D. Cox (1997), Robust frequency and timing synchronization for OFDM, *IEEE Transactions on Communications*, VOL. 45(NO. 12), pp. 1613–1621, doi:10.1109/26.650240.
- Schonhoff, T., and A. Giordano (2006), *Detection and Estimation: Theory and Its Applications*, 4th ed., Prentice Hall.
- Siemens, and Texas Instruments (1999), Generalised Hierarchical Golay Sequence for PSC with low complexity correlation using pruned efficient Golay correlators, *TS TSGR1-554/99*, 3rd Generation Partnership Project (3GPP).
- Simon, M. K., and M.-S. Alouini (1998), A Simple Single Integral Representation of the Bivariate Rayleigh Distribution, *IEEE Communications Letters*, VOL. 2(NO. 5), pp. 128–130.
- Sklar, B. (2001), *Digital Communications: Fundamentals and Applications, (2-nd edition)*, 2nd ed., Prentice Hall.
- So, H., Y. Chan, Q. Ma, and P. Ching (1999), Comparison of various periodograms for sinusoid detection and frequency estimation, *IEEE Transactions on Aerospace and Electronic Systems*, VOL. 35(NO. 3), pp. 945–952, doi:10.1109/7.784064.
- Speth, M., S. Fechtel, G. Fock, and H. Meyr (1999), Optimum receiver design for wireless broadband systems using OFDM - Part I, *IEEE Transactions on Communications*, VOL. 47(NO. 11), pp. 1668–1677, doi:10.1109/26.803501.
- Starr, T., M. Sorbara, J. M. Cioffi, and P. J. Silverman (2003), *DSL Advances*, 1st ed., Prentice Hall.
- Tang, X., M.-S. Alouini, and A. J. Goldsmith (1999), Effect of Channel Estimation Error On M-QAM BER Performance in Rayleigh Fading, *IEEE Transactions on Communications*, VOL. 47(NO. 12), pp. 1856–1864.

- Todros, K., and J. Tabrikian (2008), A new lower bound on the mean-square error of unbiased estimators, in *IEEE International Conference on Acoustics, Speech and Signal Processing, 2008. ICASSP 2008.*, pp. pp. 3913 –3916, doi:10.1109/ICASSP.2008.4518509.
- Toumpakaris, D., J. Lee, and H. Lou (2009), Estimation of Integer Carrier Frequency Offset in OFDM Systems Based on the Maximum Likelihood Principle, *IEEE Transactions on Broadcasting, VOL. 55*(NO. 1), pp. 95 –108, doi:10.1109/TBC.2009.2013754.
- Tse, D., and P. Viswanath (2005), *Fundamentals of Wireless Communication*, Cambridge University Press.
- Turin, G. (1980), Introduction to spread-spectrum antimultipath techniques and their application to urban digital radio, *Proceedings of the IEEE, VOL. 68*(NO. 3), pp. 328 – 353, doi:10.1109/PROC.1980.11645.
- van de Beek, J., M. Sandell, and P. Borjesson (1997), ML estimation of time and frequency offset in OFDM systems, *IEEE Transactions on Signal Processing, VOL. 45*(NO. 7), pp. 1800 –1805, doi:10.1109/78.599949.
- van den Bos, A. (1995), The multivariate complex normal distribution-a generalization, *IEEE Transactions on Information Theory, VOL. 41*, pp. 537 –539, doi:10.1109/18.370165.
- Viterbi, A.-J. (1995), *CDMA: Principles of Spread Spectrum Communications*, 1st ed., Addison-Wesley.
- Wang, Q., C. Mehlführer, and M. Rupp (2010), Carrier frequency synchronization in the downlink of 3GPP LTE, in *Personal Indoor and Mobile Radio Communications (PIMRC), 2010 IEEE 21st International Symposium on*, pp. pp. 939 –944, doi:10.1109/PIMRC.2010.5671968.
- Wang, Y.-P., and T. Ottosson (1999), Initial frequency acquisition in W-CDMA, in *Proceedings of Vehicular Technology Conference, 1999. VTC 1999 - Fall. IEEE VTS 50th*, vol. VOL. 2, pp. pp. 1013 –1017, doi:10.1109/VETEFCF.1999.798588.
- Wang, Y.-P., and T. Ottosson (2000), Cell search in W-CDMA, *IEEE Journal on Selected Areas in Communications, VOL.18*(NO. 8), pp. 1470 –1482, doi:10.1109/49.864011.
- Wilzeck, A., Q. Cai, M. Schiewer, and T. Kaiser (2007), Effect of Multiple Carrier Frequency Offsets in MIMO SC-FDMA, in *Proceedings of International ITG/IEEE Workshop on Smart Antennas 2007 (WSA 2007)*.

Lebenslauf

Persönliche Daten

Name: Qipeng Cai
Geburtsdatum: 20.04.1976
Geburtsort: Nantong, China

Ausbildung

1988 – 1991: Shi-Pai-Ling Mittelschule, Wuhan, China
1991 – 1994: Die erste Mittelschule an der CCNU angegliedert, Wuhan, China
1994 – 1998: Studium der Elektrotechnik
an der Huazhong University of Science and Technology
Abschluss: Bachelor
1998 – 2001: Studium der Elektrotechnik
an der Huazhong University of Science and Technology
Abschluss: Master

Berufliche Tätigkeit

2001 – 2003: Hardwareentwickler bei
Shanghai Huawei Technology Limited Company
2004 – 2006: Wissenschaftlicher Mitarbeiter am
Institut für Nachrichtentechnische Systeme
der Universität Duisburg-Essen
2006 – 2009: Wissenschaftlicher Mitarbeiter am
Institut für Kommunikationstechnik
der Leibniz Universität Hannover
seit 2009: Hardwareentwickler bei RFmondial GmbH